Probing Atomic, Electronic, and Optical Structures of Nanoparticle Photocatalysts Using Fast Electrons

by

Qianlang Liu

A Dissertation Presented in Partial Fulfillment
of the Requirements for the Degree
Doctor of Philosophy

Approved November 2017 by the
Graduate Supervisory Committee:

Peter Crozier, Chair
Candace Chan
Daniel Buttry
Jingyue Liu
Robert Nemanich

ARIZONA STATE UNIVERSITY

May 2018

ABSTRACT

Photocatalytic water splitting has been proposed as a promising way of generating carbon-neutral fuels from sunlight and water. In one approach, water decomposition is enabled by the use of functionalized nano-particulate photocatalyst composites. The atomic structures of the photocatalysts dictate their electronic and photonic structures, which are controlled by synthesis methods and may alter under reaction conditions. Characterizing these structures, especially the ones associated with photocatalysts' surfaces, is essential because they determine the efficiencies of various reaction steps involved in photocatalytic water splitting. Due to its superior spatial resolution, (scanning) transmission electron microscopy (STEM/TEM), which includes various imaging and spectroscopic techniques, is a suitable tool for probing materials' local atomic, electronic and optical structures. In this work, techniques specific for the study of photocatalysts are developed using model systems.

Nano-level structure-reactivity relationships as well as deactivation mechanisms of Ni core-NiO shell co-catalysts loaded on Ta_2O_5 particles are studied using an aberration-corrected TEM. It is revealed that nanometer changes in the shell thickness lead to significant changes in the H_2 production. Also, deactivation of this system is found to be related to a photo-driven process resulting in the loss of the Ni core.

In addition, a special form of monochromated electron energy-loss spectroscopy (EELS), the so-called aloof beam EELS, is used to probe surface electronic states as well as light-particle interactions from model oxide nanoparticles. Surface states associated with hydrate species are analyzed using spectral simulations based on a dielectric theory and a density of states model. Geometry-induced optical-frequency resonant modes are excited using fast electrons in catalytically relevant oxides. Combing the spectral features detected in experiments

with classical electrodynamics simulations, the underlying physics involved in this excitation process and the various influencing factors of the modes are investigated.

Finally, an *in situ* light illumination system is developed for an aberration-corrected environmental TEM to enable direct observation of atomic structural transformations of model photocatalysts while they are exposed to near reaction conditions.

To Peter Crozier, without whom this work would not exist.

ACKNOWLEDGMENTS

I must first and most importantly thank Dr. Peter Crozier, who let me join his research group not long after I came to Arizona State University (ASU) as an exchange student and later offered me the opportunity of pursuing my PhD degree under his guidance. I am very grateful for the instruction and support he has provided as my research advisor, my mentor and my friend.

I want to acknowledge the members of my committee, for their encouragement and for the interesting discussions we had which has provided me with other viewpoints of my projects. I am also grateful for the numerous support and help from the members of my research group. In particular, Dr. Liuxian Zhang and Dr. Benjamin Miller have shared their experience and tricks with me on conducting *in situ* experiments. I also had the chance of mentoring an undergraduate student, Adam Pocock, who has contributed to the construction of the photo-reactor system and the testing of various photocatalysts.

Throughout this research I have worked with many scientists and technicians. I acknowledge the training and help on operating the aberration-corrected microscopes provided by Dr. Toshihiro Aoki, Dr. Katia March, and Dr. Shery Chang. Karl Weiss and Fred Pena have always encouraged me and helped with some of the practical work involved in my projects. David Wright and Timothy Karcher have helped me on materials synthesis and surface characterization.

In addition, valuable discussions with Prof. Archie Howie (Department of Physics, Cambridge University) have helped on EELS interpretation using dielectric response theory. Steven Quillin and David Masiello from University of Washington are my collaborators who

have performed the DDA simulations and contributed tremendously to the understanding of cavity modes. Dr. Joerg Jinschek from FEI has helped with the design of the fiber holder, and Richard Flubacher from the mechanical instrument shop at ASU has worked with me on manufacturing the device needed for the *in situ* light illumination system.

I would also like to thank my parents and my friends, for their continuous support and encouragement.

Finally, I gratefully acknowledge the funding support from US Department of Energy (DE-SC0004954) and the use of the microscopes at John M. Cowley Center for High Resolution Microscopy at ASU.

TABLE OF CONTENTS

Page

LIST OF TABLES

Table Page

LIST OF FIGURES

Figure Page

Figure Page

1 Introduction

1.1 Background and Motivation

Access to modern energy services and increased energy consumption are found to be closely correlated to improved human quality of life (Gaye and others 2007). Since the Industrial Revolution, fossil fuels (petroleum, coal, and natural gas) have become the primary form of energy produced and consumed, and will continue to be the case for the next few decades ("EIA - Annual Energy Outlook 2017" 2017). These fuels show relatively high energy density (20-60 MJ/kg) and ease of transportation, but are not sustainable in the long-term and upon usage, emits significant carbon dioxide and other greenhouse gases, as well as undesirable contaminants such as nitrogen oxides, sulphur oxides and ash (Crabtree, Dresselhaus, and Buchanan 2004; Dresselhaus and Thomas 2001).

There is an overwhelming consensus (~97%) among climate scientists that emission of greenhouse gases and other human activities have caused anthropogenic global warming (AGW) (Houghton and Intergovernmental Panel on Climate Change 2001; Cook et al. 2013; Oreskes 2004; R. K. Pachauri, Mayer, and Intergovernmental Panel on Climate Change 2015). In fact, the atmospheric concentrations of CO_2, CH_4, and N_2O have all increased to levels unprecedented in at least the last 800,000 years, with CO_2 concentration increase being the fasted (~40% compared to the pre-industrial era), primarily due to combustion of fossil fuels (Stocker et al. 2013). The greenhouse gases alter the energy balance of the climate system through absorbing and emitting radiation within the thermal infrared range, resulting in Earth's surface temperature rise and related harmful impacts on our ecosystems (Rajendra K. Pachauri and IPCC 2008). Therefore, replacing these carbon-intensive fuels with alternative energy sources that do not emit extra but rather recycle the existing CO_2 is highly demanded by the current society.

Among the different carbon-neutral energy sources (nuclear, biomass, hydropower, wind, geothermal etc.), solar energy shows enormous potential as it is the most abundant renewable energy source but has not been well exploited at present. The energy of sunlight striking the earth in an hour is 4.3×10^{20} J, larger than all energy consumed on the planet in one year (4.1×10^{20} J) (Lewis and Crabtree 2005). However, solar energy accounts only for 0.5% of total U.S. energy production in 2014 (Beiter 2015). The current existing solar facilities include photovoltaic (PV) cells and concentrating solar thermal power (CSP) plant, both of which generate electricity from sunlight (Kannan and Vakeesan 2016). Such solar power generation is not consistent all the time due to the intermittent nature of sunshine, requiring integration of other energy sources into the grid. Another approach that's under development is the so-called "solar to fuel" or "artificial photosynthesis", which converts and stores the solar energy into the chemical energy of fuel molecules. In this way, a clean solar fuel which is easy to store and transport with much higher energy density than capacitors or batteries can be used when sunlight is not available.

Artificial photosynthesis is quite a broad category, including solar splitting of water to hydrogen and oxygen, as well as photosynthesis of biofuels which often involves carbon fixation. The former process is attractive as hydrogen is viewed as a promising future energy carrier, which can be used directly in a fuel cell to generate electricity or as a reducing agent to make carbonaceous fuels from other sources such as recycled CO_2 (Turner 1999). Various methods/systems have been investigated to produce H_2 through solar water splitting (Bard and Fox 1995). Typical examples are: (i) semiconductor solid state PV cell coupled with water electrolyzer; (ii) semiconductor electrode (liquid junction) systems or photoelectrochemical (PEC) devices; and (iii) semiconductor powder systems or functionalized particulate photocatalyst composites. The annual averaged power conversion efficiency of system (i) (PV-driven electrolysis) could reach ~11% with present Si PV modules and modern commercial electrolyzers, with likely higher efficiencies in the future, but significant costs are usually associated with such an installation (Blankenship et al. 2011; Graetzel 1981; Osterloh 2014a). System (ii) and (iii) are closely related, in which the photopotential to drive the water-splitting reaction is generated directly at the semiconductor/liquid interface. In fact, system (iii) can be viewed as a more compact version of PEC devices, with the anode and cathode directly coupled through interfaces without an electric circuit, as illustrated in **Figure 1.1**. Both methods are very often referred to as photocatalytic water splitting. It should be noted that although in a more rigorous definition they are referred to as heterogeneous photosynthesis as the water splitting reaction is thermodynamically unfavored (Bard 1979; Ohtani 2008), the phrase photocatalysis will be used in this thesis because from the kinetic viewpoint, acceleration of a chemical reaction is achieved.

System (iii) results in simultaneous production of H_2 and O_2, generating a combustive gas mixture, as H_2 flammability limit is 4 - 75% in air and goes up to 4 - 95% in oxygen (by volume) (Kanury 1975). This is an important design concern but is not an insurmountable problem especially if continuous sweeping is taking place. Despite that, considerable simplification of the apparatus is associated with this system, leading to reduced cost for industrialization, which is why system (iii) is of particular interest. Technoeconomic evaluations have been reported to compare the levelized costs of conceptual reactors associated with different systems. For the powder system, a single bed particle suspension reactor is potentially viable. With the assumptions of photoactive particles being conductive spherical cores coated with photoanodic and photocathodic materials as islands, particles, or thin film shells, and solar-to-hydrogen (STH) efficiency being 10%, this system shows an attractively low cost (~$1.6 per Kg of H_2), cheaper than any other systems and cost-competitive with fossil fuels (James et al. 2009; A. Pinaud et al. 2013).

However, demonstrated bench-scale STH efficiencies of various powder systems are about 3 orders of magnitude too low for practical application (Osterloh 2014a). Significant efforts have been made on trying to synthesize the ideal photocatalyst that will show high efficiency for an extended period of time. Certain thermodynamic and kinetic concerns need to be taken into account when developing and searching for such catalyst, which are discussed in detail in the following sections. In order to better design the catalyst structure, deeper understanding on factors that govern the efficiencies or the reactivities of the catalysts is desired. One important step in the pursuit of this goal is to perform detailed and comprehensive characterization on selected model photocatalyst systems. Therefore, this work focuses on characterizing several model systems using transmission electron microscopy (TEM) and related techniques, as well as developing specific TEM based characterization methods on photocatalysts, which are the topics of Chapter 3 - 6. The justification and advantages of using and developing TEM based techniques on photocatalysis are given in Chapter 2.

1.2 Photocatalytic Water Splitting

1.2.1 Thermodynamic Concerns

Water decomposition (Eq. 1.1) is an uphill reaction that requires a large positive change in the standard Gibbs free energy ($\Delta G^o = 237\ kJ/mol$ of H_2O). In other words, the smallest electrochemical potential (or voltage) required for this reaction to proceed is 1.23 V (Bard and Fox 1995; Maeda 2011). The overall reaction can be written as:

$$2H_2O \rightarrow 2H_2 + O_2 \qquad 1.1$$

Since water itself does not absorb much radiation within the solar spectrum, light-harvesting species (usually semiconductors) need to be used to transduce the photon energy to the reducing and oxidizing chemical potentials through generation of electron/hole (e/h) pairs. A semiconductor's energetic properties is characterized by its bandgap, which is an energy interval with very few electronic states between the valence band (VB) and the conduction band (CB) which each has a high density of states. Upon absorption of a photon with above-bandgap energy, an electron and a hole can be created in the initially empty CB and initially filled VB, respectively. The presence of a bandgap, compared to the continuously distributed electronic states near the Fermi level in a metal, ensures a much longer lifetime of the photo-excited electrons and holes (Gerischer 1990). Meanwhile, the bandgap width needs to be suitable for utilization of the solar spectrum. These are the reasons why a semiconductor is preferred over a metal or an insulator as the light absorber.

Theoretically, the minimum bandgap width required for a single semiconductor device to drive water splitting is 1.23 eV. However, in practice, certain energy losses are unavoidable, including the thermodynamic loss associated with converting the photon energy to free energy, as well as the kinetic overpotentials or the activation barriers involved in charge migration/transfer process in bulk and over the interfaces (Weber and Dignam 1984; Walter et al. 2010; Archer and Bolton 1990; Osterloh 2014b). Bolton et al. claimed that ~0.8 eV energy losses would be a reasonable estimation for an operating system, leading to a semiconductor with a bandgap of >2eV (Bolton, Strickler, and Connolly 1985). Considering the maximum photovoltage generated from a good photovoltaic device plus the additional voltages needed for electrochemical oxidation/reduction of water, Osterloh and Parkinson comes to the same conclusion that if a single semiconductor absorber is used for water splitting to achieve good catalysis, the minimum bandgap needed is greater than 2 eV (Osterloh and Parkinson 2011). In addition, the band edge positions of the light absorber need to be carefully designed so that the bottom of the CB must be sufficiently more negative than the reduction potential of H^+ to H_2 ($E^o(H^+/H_2)$), while the top of the VB sufficiently more positive than the oxidation potential of H_2O to O_2 ($E^o(O_2/H_2O)$) (**Figure 1.1**). It should be noted that the chemical potentials of the electrons and holes excited by photons may be different than the CB and VB energy levels in the ground state when in dark. For example, a 0.6 eV upper shift in potentials was observed for platinized TiO_2 powders upon exposure to light (Sakata, Kawai, and Hashimoto 1982). The electrochemical potential of a carrier under illuminated conditions is referred as the quasi-Fermi level, and as reported by Weber et al., the quasi-Fermi level of holes need to lie $\gtrsim$ 0.4 eV below the O_2/OH^- level, while the electron quasi-Fermi level need to be $\gtrsim$ 0.05 eV more negative than the H^+/H_2 level, to account for the overpotentials needed for overcoming kinetic limitations (Weber and Dignam 1984).

It should be noted that the fundamental thermodynamic principles for a tandem cell or Z-scheme design is slightly different in which the necessary oxidizing and reducing potentials are produced by a combination of two or more semiconductors, as illustrated in **Figure 1.2**. In most cases, additional redox-active molecules/ions or electrically conductive materials are used for electron transfer and stabilizing the excited semiconductors. The advantages of this type of design are that smaller bandgap semiconductors with either a large reduction or oxidation overpotential can be employed so that a wider range of visible light is absorbed leading to higher STH efficiency. In fact, a bandgap width of ~1.2 eV has been proposed for efficient utilization of solar energy (Bard 1979). From a reactor design point of view, the z-scheme system may also allow separated generation of H_2 and O_2 (M. Fabian et al. 2015; Maeda and Domen 2010).

Other than oxidizing water, the photo-generated holes may also oxidize the semiconductor itself, if the standard potential for anodic decomposition (or the thermodynamic oxidation potential of the semiconductor) is higher in energy than its VB edge. In this case, photocorrosion or photochemical reactions may proceed instead of photocatalysis. Whether a semiconductor will undergo oxidation in water is determined by the relative positions of the semiconductor oxidation potential and the water oxidation potential. Same rule applies for the photo-generated electrons. Most metal oxides are resistant to the hole oxidation and stable in water, except for those with cations at a not-highest valence states. Most sulfides and other nonoxide semiconductors are thermodynamically unstable in aqueous solution, although kinetic barriers may prevent them from undergoing photocorrosion (Y. Xu and Schoonen 2000; S. Chen and Wang 2012). Therefore, when choosing the candidate light harvesting semiconductor for water splitting, optimal bandgap and band edge alignment, as well as its stability in aqueous environment both in dark and under illumination are the first screening criteria to consider.

1.2.2 Kinetic Concerns

Once the photo-excited electrons and holes are generated in the light harvesting semiconductors, they must migrate to some active sites at the water-catalyst interface to participate in rapid redox chemistry, i.e., reducing and oxidizing water (**Figure 1.1**). The overall water decomposition reaction can then be described as two half reactions (Maeda 2011; X. Li et al. 2015):

$$2H_2O + 4h^+ \rightarrow O_2 + 4H^+ \qquad 1.2$$

$$2H^+ + 2e^- \rightarrow H_2 \qquad 1.3$$

To achieve better performance, the system demands efficient charge generation, long carrier lifetime, fast charge transport, high electrochemical conversion and fast mass transport. Moreover, a few competing processes need to be considered, since they diminish the number of electrons and holes that can be used to generate the desired products. Typical competing processes include recombination of the excited charge carriers in the bulk and at the surface of the light harvesting semiconductor, as well as the unwanted back reactions such as oxygen reduction reaction (ORR) and the reverse reaction of forming water from H_2 and O_2. These issues will be discussed in detail below.

Electron/hole generation, recombination and trapping

The number of photo-generated carriers is affected by the number, rather than the energies, of the incident photons. This is because photons with excessive energies generate carriers with large kinetic energies, which then quickly undergo the thermalization processes in ~fs regime until reaching the respective band edges (Nelson 2003). The macroscopic absorption coefficient and the thickness of a bulk material may be used to estimate how much light may be absorbed. However, apart from photogeneration, incident photons can also be scattered, particularly by surfaces/interfaces or inhomogeneities in the materials, which makes it difficult to estimate the photoabsorption efficiency in a suspension of photocatalytic nanoparticles (Ohtani 2008; Hagfeldt and Graetzel 1995). Careful experimental measurements on the initial number of electron/hole pairs generated in particles of a few nanometers can be performed using picosecond transient absorption and emission spectroscopies (Serpone et al. 1995). Also, one possible way to bypass this problem is to use a sufficiently large amount of photocatalyst powders so that full absorption of incident light can be assumed, i.e. a further increase in the catalyst amount does not increase fuel productivity (Osterloh 2015).

After the photogeneration event occurs in fs, the mobile carriers may recombine, get trapped, or undergo interfacial transfer to reductant and oxidant (Hoffmann et al. 1995). The competition between charge carrier recombination (ns to μs) and trapping (fs to ns) followed by the competition between trapped carrier recombination and interfacial charge transfer (μs to ms) are critical to the overall quantum efficiency of the catalyst. An increase in the recombination lifetime and the interfacial electron transfer rate are desired, since they result in higher photocatalytic reactivity.

Recombination can occur in the forms of photon generation (radiative recombination), phonon emission (non-radiative recombination) or as kinetic energy to another free carrier (Auger recombination). It has been shown that radiative recombination is less likely to take place in indirect-gap semiconductors than direct-gap semiconductors, since a slowly rising absorption edge results in longer radiative lifetime (Archer and Bolton 1990; Tong et al. 2012). Recombination and trapping are strongly affected by crystal defect structures, surface morphologies, adsorbed species and light intensity (Thompson and Yates 2006). For instance, trapping of photogenerated electrons at Ti cation sites, as well as trapping of holes at near-surface lattice O anions and the surface-bound radicals have been confirmed experimentally (Howe and Gratzel 1987; Hoffmann et al. 1995; Fox and Dulay 1993; Linsebigler, Lu, and Yates 1995; Kudo and Miseki 2009; Meekins and Kamat 2011). The detailed recombination kinetics are greatly influenced by the number of photogenerated charge carriers and surface adsorbates but generally speaking, when excessive electrons and holes are generated in TiO_2 nanoparticles, a fast decay event exists meaning a large percent (60 - 90%) of the charge carriers recombine within a nanosecond timescale. This fast decay component is due to recombination of delocalized or shallow-trapped charge carriers and it significantly limits the quantum yield. A slow decay of the remaining charge carriers suggests that they are deep-trapped carriers with longer lifetimes therefore they dictate the kinetics of the photocatalyzed redox chemistries (Serpone et al. 1995; Leytner and Hupp 2000; Bahnemann, Hilgendorff, and Memming 1997; Tang, Durrant, and Klug 2008).

Electron/hole transport and separation

In order to suppress recombination, it is preferred that electrons and holes can be driven to different surface sites and be spatially separated. It is well known that when a bulk semiconductor is in contact with another phase, band bending usually emerges forming a space charge layer within the semiconductor near its surface. When TiO_2 is in contact with pH 7 aqueous solution, the width of the space charge layer is in the range of 22 – 70 nm, assuming a carrier density of 10^{18}-10^{19} cm^{-3} (Sakata, Kawai, and Hashimoto 1982). It is very often argued that band bending can serve as an internal bias to help with e/h separation thus improving photoactivity. However, as the size of the semiconductor decreases, the amount of band bending will also decrease. When the particle radius equals the Debye length (which is ~3.8 –

12 nm for TiO_2), the voltage difference from the center to the surface resulted from band bending is only ~4 mV (Z. Zhang and Yates 2012), whereas at least 50 mV voltage difference is needed for charge migration (Hagfeldt and Graetzel 1995). Therefore, the particle size of the specific light absorber, along with its conductivity and dielectric constant, determine whether charge separation due to effective band bending is present. For small particles where this internal bias is absent, the charge carriers move by diffusion and in this case, a shorter carrier collection pathway is desired. Ideal carrier collection may be achieved when the particle size is smaller than the mean free diffusion lengths of electrons and holes (but it is also necessary to consider the decreased number of absorbed photons per particle and possibly faster recombination in a small particle (Serpone et al. 1995)), thus boosting the photoactivity of the catalyst system (E. Osterloh 2013). In particular, Sabio et al. have shown that a nanoscale niobate based photocatalyst leads to a 16-fold increase in H_2 evolution and an 8-fold increase in O_2 evolution over its bulk phase, due to over 200 times faster charge transport rate to the water-catalyst interface (Sabio et al. 2012). Hence, although a space charge region is less important in a nanosized system, the advantage of a shorter carrier transport pathway in such a system may enable a higher number of photo-generated carriers to reach the water-catalyst interface.

Moreover, co-catalysts are usually used in conjunction with light absorbers and their desired functionalities are (1) improving the separation of photogenerated electrons and holes by acting as either electron or hole acceptors, (2) improving charge transport across the water-catalyst interface, and reducing the overpotentials involved in the hydrogen evolution reaction (HER) and the oxygen evolution reaction (OER) (Harris and Kamat 2010; M. Fabian et al. 2015; E. Osterloh 2013; McCrory et al. 2015). Injection of photogenerated electrons from irradiated CdSe or TiO_2 to metal nanoparticles such as Pt, Cu, Au and Ag, as well as hole transfer from TiO_2 to IrO_2 have been observed and measured (Harris and Kamat 2010; Katoh et al. 2010; Subramanian, Wolf, and Kamat 2004; Takai and Kamat 2011; Meekins and Kamat 2011). The charge transfer or charge equilibration between the light harvesting semiconductor and the co-catalyst results in significantly suppressed recombination and shift of the Fermi level of the composite system. In addition, water reduction overpotential was found to be decreased by 0.2-0.26 V upon loading Pt nanoparticles as the HER co-catalyst onto a niobate based photocatalyst system, while water oxidation overpotential was decreased by 0.6 V upon loading IrO_2 as the OER co-catalyst (Compton et al. 2008). Such decrease in the redox overpotentials lead to significant increase in product yields and quantum efficiency. A brief discussion on the development of co-catalyst materials and structures is in session 1.2.3.

Reaction steps and intermediates

Various steps are involved in photocatalytic water splitting such as photoabsorption, charge recombination, charge transport to the catalyst surface, water electrolysis, mass transport in the solution phase etc. It is important to understand, kinematically, what the main limiting step is under given reaction conditions. In fact, the slow kinetics of water electrolysis has been found to be the limiting factor for the catalytic activities when niobate based photocatalyst powders are studied (Sabio et al. 2012). Furthermore, O_2 production, which requires four-hole chemistry thus is more difficult than H_2 production, is found to be the reason that limits the overall rate of water splitting on TiO_2 based systems. In particular, the OER is controlled by the interfacial reaction between holes and water, rather than transport of holes to the surface, and a long hole lifetime is strongly desired to achieve high reactivity of TiO_2 (Tang, Durrant, and Klug 2008).

The detailed mechanisms for photooxidation of water on metal oxide surfaces have been of interests to many researchers, in order to develop more efficient photocatalysts. TiO_2 has been one of the most employed model materials for studying OER, yet the suggested reaction mechanisms and the intermediates associated with the TiO_2-water system have been controversial (Linsebigler, Lu, and Yates 1995; Nakamura et al. 2005; Salvador 2011; Y.-F. Li and Selloni 2016). For example, opposing to the long-assumed electron-transfer-type OER mechanism where photogeneration of surface $OH^{\bullet}$ radicals is the initial step, a (Lewis) acid-base type mechanism has been proposed by Nakato and co-workers where OER starts from the nucleophilic attack of water to the surface-trapped hole accompanied by bond breaking, with TiOOTi and TiOOH surface peroxo species identified as the intermediates (Kisumi et al. 2003; Nakamura and Nakato 2004; Nakamura et al. 2005). Later, Salvador proposed instead a more comprehensive redox photooxidation mechanism, which is based on a few sequential steps: photoinduction of bridging oxygen vacancies, dissociative adsorption of water molecules at these vacancies generating bridging hydroxyl ions, which are then oxidized to bridging hydroxyl radicals via VB free holes, followed by generation and further photooxidation of surface-bound hydrogen peroxide species ($\mathrm{Ti-HO-OH-Ti}$) leading to oxygen evolution (Salvador 2011). Despite the difference in detailed reaction steps, overall the OER can be viewed as initiating from the formation of surface-trapped holes, which may oxidize water to oxygen via four proton-electron transfer steps, with radicals and surface-bound peroxo species being the relevant intermediates (Y.-F. Li and Selloni 2016; Duonghong and Grätzel 1984; Valdés et al. 2012; Y.-F. Li et al. 2010).

1.2.3 Development of Photocatalyst Systems

Scope

A large variety of studies have been carried out with the purpose of developing suspended particulate photocatalysts in the nano- or micro-scale. Within these studies, the photocatalysts may be grouped into two categories: (1) catalysts that can perform overall water splitting, i.e., produce both hydrogen and oxygen in (near) stoichiometric amounts; (2) catalysts that can either produce H_2 or O_2 with the aid of a sacrificial scavenger (e.g. methanol as a hole scavenger and $AgNO_3$ as an electron scavenger). Great effort has been put into studying the latter catalysts, which can be very informative on elucidating reaction mechanisms (Sabio et al. 2012). However, certain drawbacks associated with catalysts that only conduct half reaction should be noted. Kudo et al. reported that the optimum structure of a photocatalyst, $SrTiO_3$ in their case, is not the same when overall water splitting, H_2 half reaction or O_2 half reaction is considered. This result implies that the half reaction environment does not necessarily provide accurate knowledge on the optimum catalyst structure for overall water splitting (Kudo, Tanaka, Domen, and Onishi 1988). It should also be noted that one photocatalyst that's able to both reduce and oxidize water separately does not guarantee its ability to achieve overall water splitting without any sacrificial reagents (Maeda 2011). Therefore, in the general development review below, stronger focus will be put on the suspended photocatalysts developed over the years which can perform overall water splitting.

In addition, titanium and tantalum based photocatalyst systems, as well as Ni-NiO co-catalysts are among the most widely studied systems that have shown interesting water splitting performances, and they are the model photocatalysts employed in the work that will be covered in the following chapters. In this section, knowledge gained from studying these systems will be emphasized.

General development review

i. Early work

After the discovery of water photoelectrolysis at illuminated TiO_2 electrodes in 1971 by Fujishima and Honda (Fujishima and Honda 1971, 1972), the concept of 'photochemical diodes' was first formulated by Nozik in 1977 (Nozik 1977), where small sandwich-like semiconductor devices immersed in an appropriate electrolyte and exposed to light can cause redox reactions to occur including decomposition of water. Many attempts have then been made to manufacture and test potential particulate photocatalysts, with some of the first demonstrations of overall water (vapor) splitting being systems using Pt/TiO_2 and $NiO_x/SrTiO_3$ (S. Sato and White 1980; Domen et al. 1980).

ii. Elemental compositions of photocatalysts

From the elemental composition viewpoint, the main active photocatalysts reported so far are semiconductors with d^0 (empty d orbitals) and d^{10} (filled d orbitals) electronic configurations. Typical d^0 cations include Ti^{4+}, Zr^{4+}, Nb^{5+}, Ta^{5+}, W^{6+}, Ce^{4+} and usually their d orbitals construct the CBs, while typical d^{10} cations are Ga^{3+}, Ge^{4+}, In^{3+}, Sn^{4+}, Sb^{5+} and usually their hybrid sp orbitals construct the CBs. Meanwhile the VBs are typically constructed from orbitals of non-metal anions such as O 2p, S 3p and N 2p orbitals. Many sophisticated and highly active photocatalysts also contain alkali, alkaline earth and some lanthanide ions, which do not contribute to the electronic structure but help construct highly active crystal structures (Maeda 2011; X. Li et al. 2015; Kudo and Miseki 2009). In fact, some of the most active photocatalysts that have been reported so far are $NaTaO_3$:La loaded with NiO co-catalyst (Kato, Asakura, and Kudo 2003), (Na, K)TaO_3:Hf and (Na, K)TaO_3:Zr (J. Sun et al. 2011), all being Ta-based photocatalysts and show stoichiometric H_2 and O_2 production in pure water under ultraviolet (UV) light irradiation. Moreover, to better utilize the solar spectrum, active visible light photocatalysts have also been developed, with $(Ga_{1-x}Zn_x)(N_{1-x}O_x)$ based systems being one of the most famous and widely studied material systems (Maeda et al. 2005; Maeda, Teramura, Lu, Takata, et al. 2006). It should also be noted that other than these metal-based semiconductors, non-metallic systems such as nitrogen doped graphene oxide quantum dots (Yeh et al. 2014), carbon nitride-carbon nanodots composites (J. Liu et al. 2015) and other graphitic carbon nitride based photocatalysts (X. Wang et al. 2009; Maeda et al. 2009) have shown interesting photocatalytic behaviors including overall water splitting under visible light irradiation.

Most of these semiconductors are functionalized with co-catalysts to boost the efficiency of photocatalytic water splitting. These co-catalysts are usually metals or metal oxides consisting of first-row transition elements or platinum-group elements (X. Li et al. 2015). A few nonmetal-oxide co-catalysts have also been employed as co-catalysts, including tungsten carbide, MoS_2 and other transition metal sulfides (X. Chen et al. 2010; Ran et al. 2014) but these materials will not be discussed in detail here. As mentioned in 1.2.2, an important functionality of co-catalysts is to enhance water reduction or oxidation reactions, thus the extensive knowledge gained from studying electrocatalysts for HER and OER can be applied on searching highly active co-catalysts. 'Volcano' patterns are observed when investigating various pure metals as HER catalyst, and the peak HER activity is associated with an intermediate metal-hydrogen bond strength and negligible hydrogen adsorption free energy.

Noble metal Pt and Pd demonstrate exceptionally high HER activity, with Ni being the most active non-precious metal (Trasatti 1972; Parsons 1958; Walter et al. 2010). In contrast, OER catalysts are usually metal oxides, and OER are more difficult to rationalize, possibly due to the more complex intermediate structures and kinetics of an oxide phase (Walter et al. 2010). Trasatti suggested that non-stoichiometry of the metal oxide is the main factor governing the catalyst activity, and by plotting the overpotentials as a function of the enthalpy of the next lower to the nominal oxide transition, an asymmetric volcano pattern is obtained with RuO_2 and IrO_2 at the apex and NiO_x close to the apex (Trasatti 1980). Later, Valdés and co-workers constructed a different volcano plot by considering the free energy change of one of the intermediate steps along the OER process, and RuO_2, IrO_2, MnO_2, PtO_2 and RhO_2 are all close to the apex (Valdés et al. 2012). In addition to these oxides, cobalt based OER catalyst systems have been synthesized relatively recently, which exhibited water oxidation reactivity with low overpotential (Kanan and Nocera 2008; Surendranath, Dincǎ, and Nocera 2009). These findings based on the study of HER and OER electocatalysts are further confirmed by experimental evidences in the field of photocatalytic water splitting, where loading of Pt, NiO_x, RuO_2 and other co-catalysts are proved to effectively improve the H_2 and O_2 production (Maeda 2011; Ogura et al. 1997; Ran et al. 2014). As an earth-abundant co-catalyst, NiO_x has drawn great attention and shown interesting properties, but its reaction and deactivation mechanisms have not yet been elucidated. Thus, this particular co-catalyst has been chosen to be the model system to characterize in the work described in Chapter 3.

iii. Photocatalysts' structures

Different photocatalysts show drastically different crystal structures. The detailed effects of photocatalysts' microscopic structures on their reactivities have been discussed in a few articles (Maeda 2011; Inoue 2009; Kudo and Miseki 2009; P. Zhang, Zhang, and Gong 2014). Some of the important findings from studying various titanate, tantalate, niobate and indate based photocatalysts containing alkaline (earth) cations are summarized as follows: (1) a layered perovskite structure has been found to result in high activity (Takata et al. 1997; Kudo, Tanaka, Domen, Maruya, et al. 1988; Maeda 2011), and the proposed mechanism is that the HER and OER sites are located at different interlayers thus the back reaction of H_2 and O_2 forming water is prevented leading to high reactivity; (2) a tunnel structure composed of distorted metal-oxygen octahedra/tetrahedra has been found to generate dipole moments, which are positively correlated with photocatalytic activity. It is believed that local polarization fields induced by the dipole moments can promote charge separation in the very initial process of photoexcitation (Ogura et al. 1997; J. Sato, Kobayashi, and Inoue 2003; Inoue 2009); (3) for alkali tantalates and niobates, a distorted bond angle (e.g. Ta-O-Ta bond angle) has been found to negatively impact charge migration, whereas a near-180° bond angle is argued to help with carrier migration thus improving activity (Wiegel et al. 1994; J. Sun et al. 2011; Kudo and Miseki 2009).

Co-catalysts are usually in the form of small nanoparticles and can be loaded onto the light absorbing semiconductors using photodeposition or impregnation followed by some activation treatments. One general problem associated with many HER metal co-catalysts such as Pt and Rh is that they can also catalyze the back reaction, forming water from H_2 and O_2 (Maeda 2011). Engineering the co-catalysts into core-shell structures have been found as a very effective strategy to address this issue, and two examples are given below:

(1) Ni-NiO core-shell (NiO_x)

NiO_x was first used as a co-catalyst on $SrTiO_3$ for overall water vapor splitting (Domen et al. 1980), and has been widely applied on various other photocatalyst systems (Ran et al. 2014; Kudo and Miseki 2009). A pretreatment of the catalyst is necessary for it to be active, in which a reduction of the catalyst in hydrogen followed by a relatively moderate reoxidation in oxygen is involved. This treatment basically produces a Ni metal core-NiO shell co-catalyst structure, while the surface of NiO partly transforms to $Ni(OH)_2$ during the water splitting reaction (Domen et al. 1986). Domen and co-workers argued that the Ni metal assists electron transfer from $SrTiO_3$ to NiO, while the NiO shell prevents the back reaction on Ni as well as the oxidation of Ni by water (Domen et al. 1982; Domen, Kudo, and Onishi 1986). However, the discussion of the detailed reaction mechanism has been controversial and will be covered in Chapter 3 (K. Townsend, D. Browning, and E. Osterloh 2012).

(2) Noble metal-Cr_2O_3 core-shell

Maeda et al. first demonstrated on $(Ga_{1-x}Zn_x)(N_{1-x}O_x)$ based photocatalysts that the use of a Rh core-Cr_2O_3 shell co-catalyst leads to overall water splitting, whereas the use of only one phase of the core-shell (either Rh or Cr_2O_3) lead to little or no photocatalytic activity in pure water. Applying this Cr_2O_3 coating onto other noble metals such as Ir and Pt also generated similar activity improvement (Maeda, Teramura, Lu, Saito, et al. 2006). The Cr_2O_3 coating is believed to suppress the back reaction, and the proposed mechanism is that, in aqueous solution, the Cr_2O_3 shell develops a passivated layer (Cr-based composites) which may contain micropores and is permeable to protons and H_2 molecules generated at the metal-shell interface, but not to oxygen. Therefore, oxygen reduction to water, which preferentially occur at the metal surface, is prevented. It should be noted that the selective permeability of the shell for the two gas molecules remains unclear, as the van der Waals radii for H_2 and O_2 molecules are 1.20 and 1.52 Å respectively and no reliable method to probe such small micropores is identified yet (M. Yoshida et al. 2009).

1.3 TiO_2 Anatase Surfaces

The surface of a photocatalyst has a prominent role, since adsorption of the reactants, transfer of photogenerated charges from the photocatalyst to the adsorbed reactants, as well as desorption of the products all occur on the surface. Detailed characterization of the atomic and electronic structures of the photocatalyst surfaces is extremely beneficial for understanding the reaction and deactivation mechanisms. This is because, surface atomic and electronic structures of a photocatalyst dictates charge transfer events in the catalytic reactions thus affecting its reactivity. In fact, this is the motivation in this work for developing monochromated electron energy-loss spectroscopy (EELS) to study surface electronic structures (Chapter 4 and 5) and *in situ* TEM to follow catalyst structural transformations under near-reaction conditions (Chapter 6). In this section, TiO_2 anatase is used as the example material to elucidate the surface atomic structural changes when exposed to conditions related to photocatalysis. Characterization of TiO_2 surface electronic structures associated with different facets and surface defects are summarized.

1.3.1 Atomic Structures

Anatase and rutile are two main polymorphs of TiO_2, in which anatase is the more stable phase for nanoparticles below 11 nm and shows better photocatalytic activity in general, although it’s a metastable phase and can transform to rutile at elevated temperatures (Fujishima, Zhang, and Tryk 2008; Hanaor and Sorrell 2011). Since anatase is employed as a model material in the work described in the following chapters, here studies on anatase surfaces will be discussed in detail.

Anatase has a tetragonal Bravais lattice with I41/amd (141) space group symmetry. Its unit cell model is illustrated in **Figure 1.3a**. In bulk, each Ti cation is bonded to six oxygen anions (6-fold coordinated Ti or Ti-6c) forming a distorted octahedron, while each oxygen is bonded to three Ti cations (O-3c). The calculated equilibrium shape of an anatase crystal according to the Wulff construction shows a truncated bipyramid exposing two low index surfaces, (101) and (001) (**Figure 1.3b**), which are also commonly observed in the synthesized anatase nanocrystals. The calculated surface formation energies of these two surfaces along with other low index surfaces are listed in **Table 1.1**. It can be seen that, thermodynamically, (101) surface has a much lower surface energy thus it is more stable than (001). The atomic models of the two surfaces are shown in **Figure 1.3b**. (101) surface shows a wave-like or saw tooth-like morphology, with exposed Ti-5c, Ti-6c, O-2c and O-3c atoms, while (001) surface Ti-5c, O-2c and O-3c. These undercoordinated Ti and O atoms play an important role in determining the chemical activities and electronic properties of the surfaces (Diebold 2003; Andrea Vittadini, Casarin, and Selloni 2007; Bourikas, Kordulis, and Lycourghiotis 2014).

1.3.2 Water Adsorption

The majority of the investigations on how anatase surfaces interact with water molecules are theoretical, with very few experimental investigations using methods including temperature-programmed desorption (TPD), X-ray/ultraviolet photoemission spectroscopy (XPS/UPS) and scanning tunneling microscopy (STM) (Herman et al. 2003; Egashira et al. 1978; He et al. 2009). In general, it is agreed that water tends to adsorb on the perfect (101) surface in a non-dissociative way at low to monolayer coverage, which means the oxygen from the water molecule adsorb on a Ti-5c site forming two hydrogen bonds with two neighboring O-2c (A. Vittadini et al. 1998; Herman et al. 2003; Arrouvel et al. 2004; C. Sun et al. 2010). However, in the presence of surface oxygen vacancies, dissociation of water at the Ti-4c sites near the vacancies is energetically favored, forming bridging hydroxyls (Tilocca and Selloni 2004, 2003; C. Sun et al. 2010; Sumita, Hu, and Tateyama 2010). Similar behavior is also found on some of the surface step edges (Gong et al. 2006).

By contrast, dissociative adsorption of water on perfect (001) surface at low coverages is favored, which leads to cleavage of Ti-O bonds with the formation of Ti-OH bonds or terminal hydroxyls. It has been argued that hydration is an efficient way to stabilize this (001) surface, as it shows a higher degree of undercoordination and is under tensile stress. With increasing water coverages, once all surface Ti atoms carry terminal hydroxyls, a second layer can form with non-dissociated water molecules through hydrogen bonds (Gong and Selloni 2005; A. Vittadini et al. 1998; Andrea Vittadini, Casarin, and Selloni 2007; Sumita, Hu, and Tateyama 2010).

1.3.3 Surface Electronic Structures

Experimentally, selective flow of photogenerated electrons to the (101) surface over the (001) surface is observed (Ohno, Sarukawa, and Matsumura 2002; Tachikawa, Yamashita, and Majima 2011), suggesting different electronic structures are associated with these two surfaces with different atomic configurations. This is supported by theoretical calculations of density of states of anatase surfaces when they are in aqueous surroundings. The lowest unoccupied states or the bottom of the CB of (101) show a larger population and a more significant distribution on the surface layer, thus facilitating accumulation of photoelectrons on this particular surface. Meanwhile holes tend to move to the (001) surface due to its slightly higher VB compared to the bulk (Y.-F. Li et al. 2010; Selcuk and Selloni 2016).

Another important feature of surface electronic structures is the presence of surface states. The existence of specific electron states associated with crystal surfaces was first illustrated by Tamm (Tamm 1932). By one definition, a surface state is an electronic state in which the probability amplitude of an electron decreases exponentially with increasing distance from the surface (outside or inside) (Henzler 1971). The origin of surface states can be categorized into two types: intrinsic, meaning states of a free surface without any foreign atom, and extrinsic, including the ones associated with absorbed atoms and/or surface defects (Davison and Levine 1970; Mönch 2013). In the case of anatase, a defect-free (101) surface shows no bandgap states, however, deep bandgap states approximately 1 eV below the CB edge can be introduced by hydroxyls, oxygen vacancies and step edges on this surface. This is consistent with the observations from doped or reduced rutile, where bandgap states lie ~0.8 - 1 eV below the CB edge are commonly detected (Setvin et al. 2014; Selcuk and Selloni 2016; Thomas et al. 2007; Finazzi et al. 2008). In addition, as for reduced anatase (001) surface, shallow dispersive donor levels or deep defect state with 0.8 eV binding energy have been observed in separate studies (Moser et al. 2013; Y. Wang et al. 2013).

1.4 Objectives and Outline

As illustrated in the previous sections, photocatalytic water splitting is a very complicated process involving multiple steps. Developing an ideal photocatalyst that can be efficient and stable is quite a challenging task, which requires fundamental understandings on the reaction and deactivation mechanisms. This usually involves detailed characterization of the atomic, electronic and photonic structures of carefully selected model materials. Also, since the structures of photocatalysts during reactions may not necessarily be the same as their original structures, *in situ* observations of these materials under conditions related to photocatalysis is essential for gaining accurate information and elucidating the true mechanisms.

In this study, particulate photocatalyst systems (Ni-NiO/Ta_2O_5, TiO_2) as well as oxide nanocubes (MgO, CeO_2) are employed as the model systems under investigation. TEM, EELS and other related techniques are the characterization methods used and developed. These fast electron (or high voltage electron) based characterization techniques show superior spatial resolution thus local information from nano-sized particles can be extracted. The scientific questions that are attempted to address are:

1) What is the reaction mechanism associated with a Ni-NiO core-shell co-catalyst? What is the most active co-catalyst structure? Do they deactivate over time and what is the deactivation mechanism?
2) Do surface states form when an oxide is exposed to water and can one detect the surface states at the nanometer level using EELS? How to interpret the signals?
3) At the atomic level, what structural transformations occur on the surfaces of a model photocatalyst when it's exposed to near-reaction conditions?

In order to answer the first question, high resolution TEM images have been obtained from initial and used co-catalysts. By correlating the atomic structures with H_2 productions, structure-reactivity relationships of the co-catalysts, as well as the deactivation processes, have been investigated. The proposed reaction and deactivation mechanisms associated with this particular system are discussed in Chapter 3.

MgO nanocubes are used as the model material to develop the EELS based technique of characterizing and interpreting surface states, which is discussed in detail in Chapter 4. However, when this technique is applied on TiO_2 and Ta_2O_5 photocatalysts, excitation of cavity modes is observed. Understanding the cavity modes behaviors is desired as it is related to the photonic structure of the oxides. Efforts have been made to characterize the cavity modes on TiO_2 nanoparticles and CeO_2 nanocubes with results showing in Chapter 5.

In situ TEM techniques related to photocatalysis need to be developed in order to answer the third question, which requires building an *in situ* light illumination system onto an aberration-corrected environmental TEM. Chapter 6 will present the details of this illumination system and preliminary results obtained using TiO_2 anatase nanoparticle as the model material.

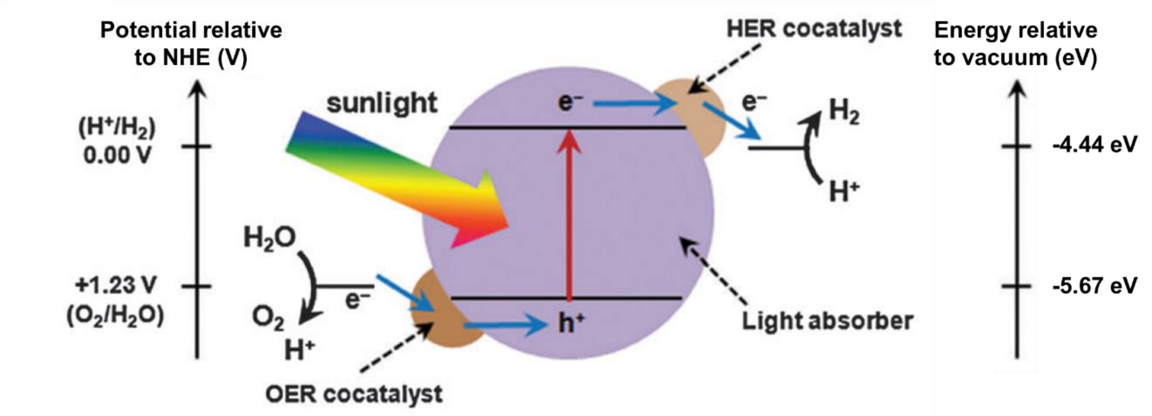

Figure 1.1: A schematic showing the principles of photocatalytic water splitting, with a single light harvesting semiconductor. Adapted from Fabian et al. 2015.

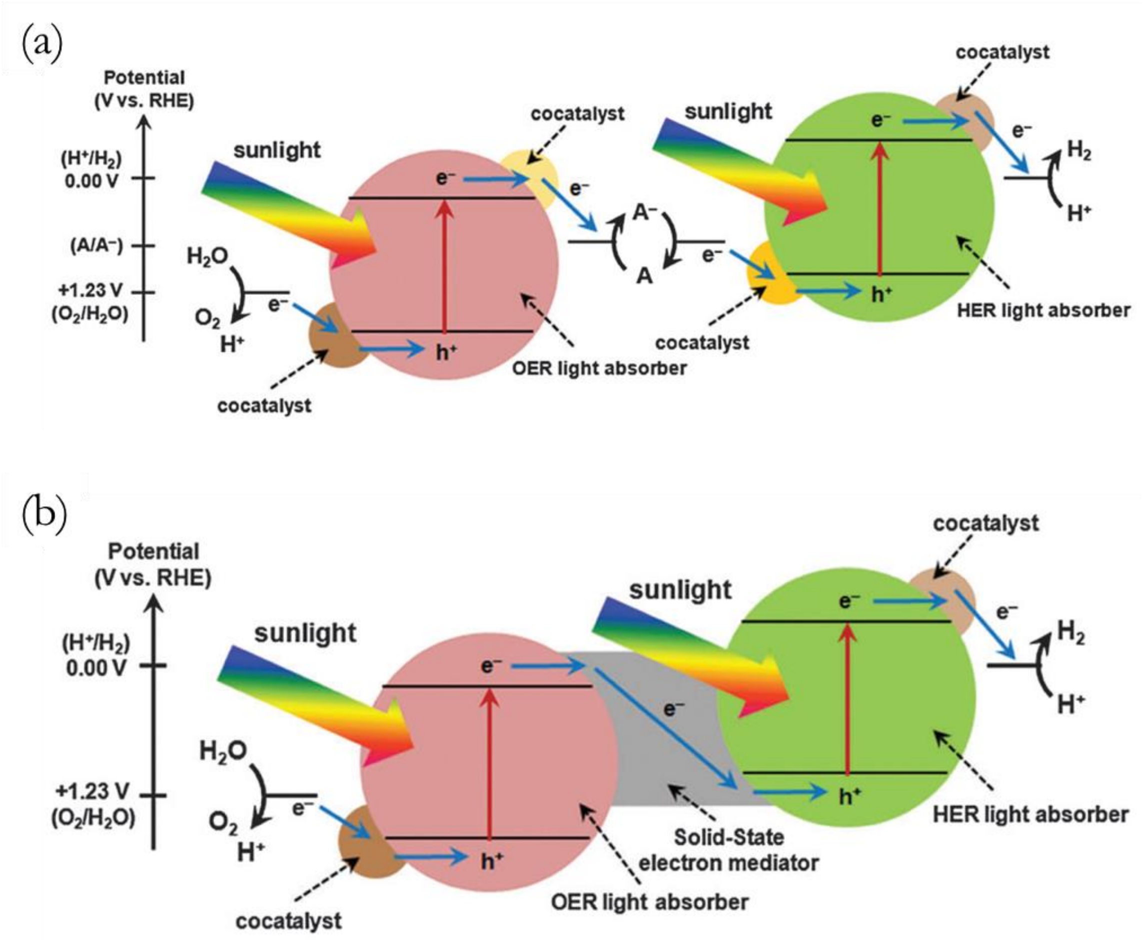

Figure 1.2: Schematic of two types of tandem cell designs, with (a) redox-active molecules/ions, or (b) electrically conductive materials respectively (Fabian et al. 2015).

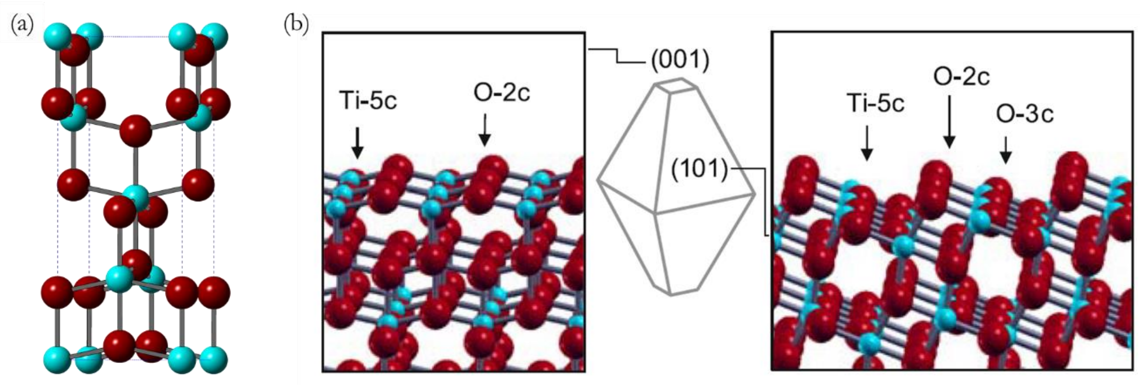

Figure 1.3: (a) A unit cell model of anatase. Red - O atoms; Blue - Ti atoms. (b) Center graph shows the equilibrium shape of a TiO_2 anatase crystal. Left is the model structure of the (001) surface, and right is the model structure of a (101) surface. Figure adapted from Vittadini et al. 2007.

Table 1.1: Calculated surface formation energies of four low index surfaces for anatase TiO_2 (Gong et al. 2006).

Surface	(101)	(001)	(103)	(100)
Calculated surface energies ($\times 10^{-2}\ eV/\text{Å}^2$)	2.75 – 3.5	5.63 – 6.44	5.19 – 6.94	3.31-4.63

2 Methods

As illustrated in the previous chapter, the photocatalytic behaviors of a material are essentially determined by its atomic, electronic and optical structures. Characterizing these structures and correlating them with the photocatalytic reactivities is thus necessary to gain fundamental understandings of the reaction and deactivation mechanisms. In this work, a photo-reactor system is built to perform photocatalytic water splitting reactions to measure the gas productions thus quantitatively determining the reactivities of different photocatalysts. Several structural characterization methods have been applied and developed. High resolution imaging of photocatalyst nanoparticles has been performed by employing aberration-corrected (scanning) transmission electron microscopes. Therefore, basic principles of TEM/STEM imaging and advantages of aberration correction are explained in detail in section 2.2 and 2.3. A special form of monochromated EELS is developed as a high spatial resolution technique for probing surface electronic states, as well as light-particle interactions. Monochromation, EELS acquisition and interpretation are discussed in section 2.4. In addition, an *in situ* characterization approach is developed in this work, specific for the study of photocatalysts, where an environmental TEM is employed. Thus, a general introduction to *in situ* TEM as well as environmental cells is given in section 2.5.

2.1 Photo-reactor System

To test the water splitting activities of the photocatalysts, a continuous flow photo-reactor system was designed and built. A picture of the liquid phase reactor and a schematic showing the major components of this system is in **Figure 2.1**. The liquid phase reactor is a beaker-shape glass container (outer diameter at the bottom: 2.2"; height: 2.6") with two connecting tubes (outer diameter: ¼") as the gas inlet and outlet. On the top of the container, a quartz window (diameter: 3") with an O-ring is clamped to the container to form a seal. The quartz window is used for transmitting the incident light since high transmittance for both UV and visible light is desired.

The light source employed here is a 450 W xenon lamp house (Newport, Inc.) with a mirror selectively reflecting a certain wavelength range (to match the bandgap of the photocatalyst). For example, a mirror selecting 260 nm to 320 nm wavelengths is used for Ta_2O_5 based photocatalysts, and a mirror selecting 350 nm to 450 nm wavelengths is used for TiO_2 based photocatalysts. The incoming photon flux for the liquid phase reactor can be calculated based on the irradiance spectrum of the light source and the reflectivity spectrum of the mirror.

The gas inlet and outlet on the reactor are connected to a mass flow controller (MFC) and a gas chromatography (GC) respectively. The MFC (Alicat Scientific, Inc.) is used to control the flow rate of a carrier gas (usually Ar or He) for the photo-reactor system. Before starting a catalytic reaction by switching on the incident light, the carrier gas is flowed to purge the system to remove the residual air, usually with a high flow rate such as 30 cc/min. During the catalytic reaction, the carrier gas mixes with the evolved H_2 and/or O_2 in the reactor and then flows into the GC, usually at a slow flow rate such as 3 or 5 cc/min. The H_2 and/or O_2 production rates from the catalysts can then be detected and quantified using the GC.

Detailed operating principles of a GC can be found in these references (Grob and Barry 2004; Poole 2012). For this work, a Varian 450 GC equipped with a porous-layer open tubular (PLOT) column and a thermal conductivity detector (TCD) is employed. Fine layers of adsorbent are deposited on the inside wall of the column, and different gas species will experience different adsorptive forces when interacting with the adsorbent. Thus, the time it takes for each gas species to flow through the column is different and characteristic, resulting in separation or eluting of various gas species from a gas mixture. The gases exiting the column then passes through the TCD which is a non-destructive detector that incorporates a Wheatstone bridge circuit consisting of a reference side and an analytical side. Pure carrier gas passes over the reference side, while carrier/sample gases flows over the analytical side. On each side, there is a heated wire filament with a temperature-dependent resistance. The difference in thermal conductivity of a sample gas compared to the carrier gas causes a resistance change of the filament which is measured and outputs as voltage signals. These signals are then plotted over time to generate a chromatograph or a spectrum, which should show a flat baseline punctuated with peaks corresponding to each sample gas (see section 8.1). The signal strength depends on the concentration of the sample gas as well as the difference in thermal conductivity between the sample and the carrier gas, therefore a large difference is preferred to improve the sensitivity. A list of thermal conductivities of 30 common gases can be found in (Poole 2012). As for detecting the products of water splitting reaction, Ar carrier gas is a good option for detecting H_2 while He carrier is usually used for detecting O_2.

Correction factors are required to obtain the H_2 and O_2 production rates (in μmol/h/g) from the signal intensities in the chromatographs. One way to gain the correction factors is to conduct calibration runs of electrolysis of water, under the same GC operating conditions as for photocatalytic water splitting runs. The advantage of this calibration method is that the H_2 and O_2 gases are produced at a 2:1 ratio and their quantities can be comparable with those using the photocatalysts involved in this work (shown in section 8.1). In a typical set-up, a Gamry Reference 3000 potentiostat is employed to provide small amount of voltages (e.g. 3 to 4 volts) to a low concentration alkaline water electrolyte (NaOH) through two Pt wires as the electrodes. The H_2 and O_2 generated are mixed with the selected carrier gas and flow into the GC to be detected. The gas production rates in the calibration runs can be calculated since the current and the duration time are monitored by the potentiostat. The correction factors are thus obtained by correlating the known gas production rates with the signal intensities in the chromatographs.

It should be noted that water vapor is generally harmful to the GC therefore a condenser has been added to the system after the reactor and before the GC inlet. In addition, efforts have been made to upgrade this continuous flow design by incorporating a gas recirculation option. A recirculation system is particularly useful when the yield of the catalytic reaction is low or simultaneous detection of both H_2 and O_2 is desired, as the evolved gases are circulated and accumulated in a gas-closed system. This is achieved by coupling a diaphragm gas recirculation pump (Gardner Denver Thomas) into the system and modifying the gas lines to allow the selection of a circulation loop. Over time the product concentrations build up exceeding the detection limits. Employing He as the carrier gas, simultaneous detection of O_2 and H_2 generated using a Ta_2O_5 based photocatalyst is achieved in the recirculation system, even though the sensitivity of detecting H_2 in He is low (discussed in section 8.1).

2.2 Transmission Electron Microscopy (TEM)

TEM and its related techniques are the primary characterization techniques used in this work due to the following reasons:

(1) The materials under investigation are particles with sizes ranging from a few nanometers to hundreds of nanometers. Detailed atomic structures, especially on the surfaces, of these particles need to be characterized as fundamental understandings are

pursued. Also, heterogeneity often occurs in the powder system so techniques that give averaged bulk information do not have the capability to probe it. Instead, TEM shows superior spatial resolution which allows characterizing complicated structures at the nano- and atomic-level.

(2) TEM is also a very versatile technique, as various imaging and spectroscopy signals can be coupled and different operation modes can be achieved for different applications. Therefore, a material's chemical information and electronic structure can be correlated with its atomic structure. In fact, developing novel TEM based characterization approaches/methods to study photocatalysts is an important goal of this work.

Details of the instrumentation and physical principles of TEM and related techniques is readily available (Williams and Carter 2008; Reimer 2013; Erni 2015; Pennycook and Nellist 2011; R.F. Egerton 2011). In this section, the spatial resolution and imaging fundamentals of TEM are briefly explained, while in the following sections other operation modes and related techniques used in this work are discussed.

Historically the motivation for developing TEM is to surpass the imaging resolution limit of visible-light microscopes. Based on the Rayleigh criterion, the smallest distance that can be resolved using visible-light microscopes is approximately equal to half of the photon wavelength, which is in the range of hundreds of nanometers. As for TEMs, the theoretical resolution can be approximated as $\sim 1.22\lambda/\beta$, where λ is the wavelength of the incident electron and β is collection semi-angle of the magnifying lens. Ignoring relativistic effects, the electron wavelengths (in nm) can be approximated from their energy E (in eV):

$$\lambda \approx \frac{1.22}{\sqrt{E}} \qquad 2.1$$

For a 100 keV electron source, $\lambda{\sim}4\ \mathrm{pm}$, thus the theoretical minimum resolvable distance is much smaller than that using visible-light radiation. In practice, realization of this wavelength-limited resolution limit is not yet achieved in a TEM since many factors degrade its performance, such as imperfections in the electron lens systems (discussed later) and external interferences (electromagnetic fields, mechanical instabilities, etc.).

A schematic of an ideal electron scattering experiment is shown in **Figure 2.2**, which is the basis of electron imaging in a TEM (Van Dyck and de Jong 1992). Each of the three primary components shown in this schematic (illumination, scattering and detection) has its distinct functionality. The illumination system consisting of an electron source and condenser lenses is used to determine the state of the electron immediately before interacting with the object/specimen (plane A), which is parallel or broad illumination for TEM (**Figure 2.3a**). Then the incident electron, or the fast electron, undergoes scattering events when passing through the specimen, resulting in trajectory and energy changes. At last, the state of the electron after interacting with the specimen (plane B) is selectively detected to form a magnified image that carries information of the specimen. It should be noticed that, for conventional or uncorrected TEM, the property of the objective lens post-field (relative to the sample) is vital to the microscope performance.

To interpret the specimen information from a TEM image, one needs to understand the various factors contributing to the image contrast (Williams and Carter 2008). As the electron wave traverses the specimen, both its amplitude and phase can change, giving rise to image contrast. Although in many cases, both amplitude contrast and phase contrast are present in an image, it is preferred to make one of them predominant by selecting certain imaging condition. Within the category of amplitude contrast, there are two principle types, i.e., mass-thickness contrast and diffraction contrast. Mass-thickness contrast results from incoherent elastic scattering, or Rutherford scattering, in which the fast electron is deflected by the intense local electric field of the nuclei in the specimen. As a result, the cross section for Rutherford scattering strongly depends on the atomic number Z (or sample density) and the sample thickness. On the contrary, diffraction contrast arises from coherent elastic scattering, or Bragg scattering, of the fast electron by a crystalline sample. Strong diffraction contrast can be achieved by tilting the specimen to a two-beam condition, where only one diffracted beam is strongly excited along with the transmitted beam. Using either one of the two beams, images can be formed with diffraction contrast. This is particularly useful when studying defects in crystals.

On the other hand, when two or more beams (transmitted or Bragg scattered) are used to form an image, phase contrast arises from the interferences of the electron waves with different phase delays, generating lattice fringes in the image. Phase contrast is very sensitive to instrument and specimen parameters including objective lens defocus and astigmatism, as well as sample thickness and orientation. In many cases (especially for uncorrected TEMs), as the lattice fringes or the spots in the image bears no direct relationship to the positions of atomic planes or atom columns in the crystal, image simulations are required if one needs to interpret the detailed atomic structure of the sample. However, the lattice fringes give information on the lattice spacing and orientation of the specimen. As will be shown in Chapter 3, lattice fringes are used to verify the appearance of Ni and NiO phases in the photocatalysts.

Aberration Correction

Apart from the specimen, the presence of aberrations of electron lenses can also induce phase changes which are significant for image interpretation. These aberrations can be grouped into two types: (i) geometrical aberrations such as spherical aberration (C_s). In this and the next section, effects of the spherical aberration and benefits of C_s correctors are discussed. (ii) chromatic aberrations (C_c), which are due to the electron-energy dependent refraction strengths of the magnetic fields induced by the lenses. A field emission gun (FEG), a C_c corrector, and/or a monochromator can be used to help reducing the effects of chromatic aberrations (Urban 2008; Spiecker et al. 2010; Hosokawa et al. 2013). A recently developed monochromator will be briefly introduced in section 2.4.

In conventional TEMs, the spherical aberration of the objective lens makes the lens field behaves differently for off-axis rays, thus a point object is imaged to a disk. Clearly, this degrades the detail that can be resolved in a TEM image. The point resolution of a conventional TEM (which represents the smallest detail that can be directly interpreted) has been derived to be $\sim 0.66 \times {C_s}^{1/4} \lambda^{3/4}$, and it can be achieved when a special negative defocus (Scherzer focus) is employed to partly balance the effect of the spherical aberration (Scherzer 1949). In other words, at a fixed electron wavelength, the spherical aberration coefficient C_s limits the point resolution of a conventional TEM. Image details smaller than this point resolution (or at higher spatial frequencies) suffer from complicated contrast oscillations and thus are not directly interpretable. As shown in **Figure 2.4**, developing higher energy electron beams (i.e., reducing the electron wavelength) and better polepieces with reduced C_s has led to a steady improvement of the microscope point resolution until about 1 Å resolution is achieved (O'Keefe 2008).

This situation changed when software and hardware aberration correction methods were invented, leading to substantial improvement in resolution for medium-voltage microscopes (**Figure 2.4**). After a hexapole C_S corrector system was first installed onto a TEM by Haider and coworkers (M. Haider, Braunshausen, and Schwan 1995; Max Haider et al. 1998), many other hardware C_S correctors have been manufactured, which are basically sets of carefully designed multipole lenses, for both TEM and STEM. With the aid of the correctors, C_S can not only be compensated, but also has become an experimental variable. In fact, it has been shown that, for thin samples, tuning C_S to a small negative value and balancing its effect with an optimum positive defocus makes it possible to resolve light elements in the direct neighborhood of columns of heavy elements (Jia, Lentzen, and Urban 2004). Under this so-called negative C_S imaging condition (NCSI), the complicated contrast oscillations at high spatial frequencies present in uncorrected TEM is now absent, therefore interpretable contrast can be retained at a much better resolution. Furthermore, image delocalization is also greatly suppressed under this condition, which is caused by phase dispersion at different spatial frequencies. Simulations of a single unit cell of $(PbS)_{1.14}NbS_2$ embedded in vacuum are conducted by Spiecker et al. as an example to illustrate the suppression of image delocalization at a NCSI condition. **Figure 2.5a** shows a simulated conventional TEM image at Scherzer defocus, revealing extended delocalization of contrast into the vacuum region, as well as complex image pattern difficult to interpret. On the contrary, **Figure 2.5b** shows a simulated aberration-corrected image where hardly any delocalization effects are seen at the interfaces of the unit cell and the vacuum. Moreover, the image pattern can be directly compared to the projected crystal structure (inset), meaning the bright dots in the image correspond to atomic columns in the crystal structure (Spiecker et al. 2010). These advantages of aberration correction are very important for imaging photocatalyst nanoparticles, especially their surfaces, if atomic-level structural information is desired. The suppression of delocalization allows easier interpretation of images of the nanocrystals' surfaces. The NCSI technique allows both cation columns and oxygen columns to be observed and located in the oxide photocatalysts, under optimum conditions.

2.3 Scanning Transmission Electron Microscopy (STEM)

Different than TEM, the main components in a STEM illumination system include condenser lenses, scanning coils and objective lens pre-field (**Figure 2.3b**). A convergent electron beam, namely a probe, is formed onto the specimen plane by the illumination system, which also scans laterally across the region of interest, without tilting the probe relative to the optic axis. The aberrations in the probe-forming system in a STEM are critical to its image quality, as they determine the size and shape of the probe, as well as how much beam current can be put into the small probe. By coupling C_S correctors to STEM systems, a sub-Ångström probe with much higher current can be achieved nowadays, leading to greatly improved spatial resolution and image contrast (O. L. Krivanek, Dellby, and Lupini 1999; Batson, Dellby, and Krivanek 2002; Nellist et al. 2004; Smith 2008).

As the probe scans across the sample, a stationary convergent-beam diffraction pattern forms with varying intensity distributions. Similar to what happens in TEM mode, coherent and incoherent elastic scatterings of the fast electron occur when it interacts with the specimen, which give rise to different types of STEM image contrast. Instead of using objective apertures to enhance certain types of image contrast in TEM, various detectors have been designed to form STEM images featuring different contrast by intercepting different parts of the diffraction pattern. As shown in **Figure 2.6**, STEM bright field (BF) images can be formed using a BF detector, which intercepts the forward-scattered electrons on axis, i.e., the direct beam. **Figure 2.7a** shows an example of a STEM BF image of a Ni core-NiO shell loaded on a Ta_2O_5 particle, which is an active photocatalyst. Similar to a high resolution TEM image, lattice fringes are observed here, resulting from the overlapping and interference of the direct beam and the diffracted beams. It should be mentioned that, relatively recently, annular bright field (ABF) detector has drawn increasing attention, which has an annular shape and is located within the direct beam region, as it enables direct imaging of light elements such as oxygen, along with heavy elements (Okunishi et al. 2009; Findlay et al. 2009). STEM dark field images can be formed using an annular dark field (ADF) detector with an inner radius of maybe a few tens of mrad up to perhaps 100 mrad, and an outer radius of several hundred mrads. A special ADF detector which only picks up high angle ($\gtrsim$ 100 mrads) scattered electrons is referred to as a high-angle annular dark field (HAADF) detector. At high scattering angles, Rutherford scattering which is Z-dependent, becomes the dominant mechanism for image contrast. Therefore, HAADF images are also very often called Z-contrast images, allowing relatively intuitive image interpretation in favorable cases, especially when high Z elements are dispersed on low Z supports. An ADF image of a used Ni-NiO/Ta_2O_5 photocatalyst is shown as an example in **Figure 2.7b**. Interestingly, this image reveals that the Ni-NiO core-shell particle is decorated with lots of dots with high brightness, indicating that the heavier atoms, Ta atoms, has migrated from the oxide support onto the Ni-NiO.

2.4 Electron Energy-loss Spectroscopy (EELS)

The structural information obtained using various imaging techniques discussed above can be supplemented by chemical information from the same area with nano- or atomic-level resolution, using different spectroscopy techniques. Majority of these techniques deal with the secondary de-excitation processes such as energy dispersive X-ray spectroscopy (EDX) and cathodoluminescence spectroscopy (CL), while EELS focuses on the primary electron excitation processes, offering a wealth of information such as bonding or oxidation state of the ions in the specimen. Recent development of a novel form of monochromator has enabled unprecedented energy resolution to be achieved in a STEM EELS (Ondrej L. Krivanek et al. 2009, 2013). This novel form of monochromatic EELS is heavily employed to detect surface states (Chapter 4) as well as cavity modes (Chapter 5) from oxide nanoparticles. Therefore, general concepts of EELS and this particular monochromator are introduced in this section.

By measuring the distribution of energy losses of the incident electrons after they interact with the specimen, EELS provides a way of probing materials' chemical, electronic and optical properties in the electron microscope. The main energy-loss mechanism lies in the inelastic scattering of the incident electron by the atomic electrons in the specimen due to Coulomb interaction. Such inelastic scattering events lead to quite small changes in the direction of the fast electron momentum, thus the entrance aperture of an EELS spectrometer can be placed at the optic axis of the microscope, collecting the forward scattered electrons with angles up to tens of mrad. As illustrated in **Figure 2.8** (Crozier and Miller 2016), these electrons then go through a magnetic prism spectrometer, being dispersed according to their energies. More specifically, a magnetic field is produced by the electromagnet in the spectrometer, forcing an electron to travel along an arc orbit, with a radius proportional to its velocity. Therefore, an electron that has suffered more energy loss will have lower velocity, and thus is bent more in the magnetic prism and vice versa, leading to the dispersion of the electrons. If a focusing and magnifying system as well as a charge-coupled device (CCD) are used to detect the exiting electrons from the spectrometer, an EEL spectrum can be generated.

Figure 2.8 also illustrates a typical EEL spectrum consisting of three parts: a zero-loss peak (ZLP), a low-loss region and a core-loss region. The ZLP results from electrons that have transmitted through the specimen without experiencing noticeable energy losses. Its intensity is often used to determine sample thickness. Generally speaking, a reasonably high ZLP is preferred as it indicates sufficiently thin specimen, in which case plural scattering can be suppressed, leading to more interpretable EELS signals. The full width at half maximum (FWHM) is another important parameter of the ZLP, as it represents the energy resolution of EELS. Without a monochromator, EELS energy resolution is limited by the energy spread of the electron source to about 0.25 eV for a cold FEG, and about 0.5 eV for a Schottky FEG. The recently developed alpha-type monochromator by Krivanek and coworkers has improved the energy resolution by an order of magnitude (Ondrej L. Krivanek et al. 2009, 2013). As shown in **Figure 2.9**, this monochromator is placed after the gun and the accelerator, but before the condenser and the objective lenses in an aberration-corrected STEM. The three magnetic prisms along with the multipole optics in the monochromator bend the electrons by 360°. At the same time, the electrons exiting the accelerator are first dispersed and projected onto a slit, where a narrow energy passband is selected, then the dispersion is canceled, resulting in significant improvement of the energy width of the incident electrons. **Figure 2.10a** compares the FWHM of the ZLP obtained when the slit is retracted (unmonochromated) and inserted to a nearly closed position (monochromated), revealing that a much narrower

ZLP with greatly suppressed tail intensities can be attained using the monochromator. This means subtle spectral features close to the ZLP can now be detected instead of obscured, enabling local studying of vibrational signals as their energies are in the range of 50 to 500 meV (Ondrej L. Krivanek et al. 2014).

Spectrum region roughly within 50 eV is referred to as the low-loss region, where intensities mainly arise from exciting a single outer shell electron to a higher electronic state, or excitation of collective modes that involve many valence electrons, i.e., plasmon oscillations. The suppression of the ZLP tail by the monochromator also benefits the detection of spectral details in this low-loss range, generating information on, for example, materials' band structures. **Figure 2.10b** shows a typical monochromated spectrum from anatase nanoparticles, where a nearly flat, featureless spectrum region is observed in between the ZLP and the intensity onset at ~3.4 eV (bandgap onset). This is because, for a defect-free semiconductor, the smallest energy that can be transferred from the fast electron to the sample in an electronic excitation event is its bandgap energy, as an electron at the top of the VB is excited into the bottom of the CB. Above the bandgap onset, the intensity variations are related to the density of states in the VB and the CB of the semiconductor. In addition, if electronic states are present within the bandgap, energy losses smaller than the bandgap energy may occur resulting in spectral features before the onset. These topics will be discussed in detail in Chapter 4. Moreover, spectral intensity changes in this bandgap region may also result from other physical phenomena than electronic excitations, including Cherenkov radiation and guided light modes, which is the focus of Chapter 5.

The spectrum region above ~50 eV is referred to as the core-loss region, where ionization edges representing inner-shell excitations are found superimposed on a continuously decreasing background, as shown in **Figure 2.11**. The edge onset energy corresponds to the characteristic ionization threshold thus giving elemental identification. The spectral features within the first several tens of eVs after an edge onset is often referred to as the energy-loss near-edge structure (ELNES), which represents approximately the local density of unoccupied electronic states above the Fermi level. The ELNES is thus quite useful for revealing local bonding and near-neighbor coordination configurations. Intensity oscillations about 50 eV beyond an ionization edge onset are often referred to as the extended energy-loss fine structure (EXELFS), containing information on interatomic distances and degree of atomic disorder. It should be mentioned that in the core-loss region, the improved energy resolution by a monochromator could be beneficial for resolving more details in the fine structures of an ionization edge.

EELS interpretation using simulations

The energy-loss signals usually contain a wealth of information and detailed interpretation of the signals generally requires simulation, especially for the low-loss region. In this work, three different approaches have been used to interpret the low-loss EELS signals generated from oxide nanoparticles, through spectral simulations within the frameworks of dielectric response theory, density of states (DOS), and discrete dipole approximation (DDA). These approaches are briefly introduced and compared below, as more detailed discussions are covered in Chapter 4 and 5.

A material's response to external electromagnetic fields can be described using the bulk dielectric function, which is a frequency- and wave vector-dependent complex function that can be calculated from first principles in favorable cases as it is intimately related to band structures (Landmann, Rauls, and Schmidt 2012), or be experimentally obtained using optical techniques such as spectroscopic ellipsometry (Jellison et al. 2003). Once the bulk dielectric function is known for a given material, it is then possible to calculate the electron energy-loss probability, or the theoretical EEL spectra, via formulas derived based on the dielectric response theory. This theory treats the target material as a continuum medium characterized by its bulk dielectric function, and are usually applied to relatively simple sample geometries. The sample geometry used in this work to simulate an MgO nanocube with a surface layer is an infinite slab model where the MgO medium extends to infinity and the surface layer only covers one side of the MgO (Howie and Milne 1985). Obviously, this is not an accurate description of the nanocube geometry but is often a reasonable approximation. In addition, the distance between the electron trajectory and the surface of MgO is fixed when the fast electron is passing by the material in this model, which is not the case in reality since electrons are likely to be deflected by the target material. Despite the simplifications and approximations, the dielectric theory based spectral simulations which are easy to perform (especially in the non-relativistic scenario) still generate good matches with experimental spectra, yielding an estimate thickness of the surface layer.

DDA (Draine and Flatau 1994), also referred to as the coupled-dipole approximation (Purcell and Pennypacker 1973), has been routinely used to model the response of nanoparticles exposed to electromagnetic radiation, especially for studying plasmonic excitations (Bigelow et al. 2012). In this approach, the continuum target material is approximated and described as a finite number of small polarizable volume elements or point dipoles, allowing the Maxwell's equations to be numerically solved. Under an external electric field, the dipole moment formed at a specific point is affected by the applied field as well as interactions with all other point dipoles, which can be calculated using the bulk dielectric function (Geuquet and Henrard 2010). This numerical method can in principle deal with arbitrarily shaped particles and electron beam positions (Zubko et al. 2010), which is an advantage over the method based on dielectric theory, although it requires sufficient computer power.

Different than the above two approaches, no consideration of sample geometry is needed for DOS modeling. Here the experimental EELS spectrum is approximated as a single scattering distribution, which is calculated based on the distribution of the filled and empty electronic states (i.e., DOS) of the target material in the ground state. This means only the energy-loss signals resulting from electronic excitations can be simulated using the DOS approach, whereas the DDA approach can also simulate energy-loss signals resulting from scattering events. The advantage of the DOS approach, as will be shown in Chapter 4, is that information on the bandgap states associated with the nanocube surface can be obtained.

2.5 *In Situ* (S)TEM

In situ characterization in a TEM allows direct observation of nanomaterials' dynamic responses to selected and controlled stimulus/stimuli, by modifying the standard operation condition in a TEM. Early *in situ* approaches include the use of a hot stage to study crystallization, the incorporation of an ultra-high vacuum environment to perform surface science studies, as well as the construction of a water saturated environment to prevent sample from degradation (Butler and Hale 1981). The development of *in situ* techniques since then has enabled exposure of TEM specimens to gas, liquid, thermal, biasing and mechanical stimuli, with the aim of learning various materials' properties (Taheri et al. 2016). In the field of catalysis, some of the main motivations/benefits for conducting *in situ* (S)TEM experiments are: (i) the *in situ* capability provides access to conduct pretreatment of the catalysts in the microscope to form well-defined initial model structures, or to elucidate synthesis routes. (ii) the active catalyst structure may not necessarily be the same as the initial catalyst structure. In other words, it is quite possible that when a catalyst is exposed to reaction conditions, structural transformation occurs. Thus, *in situ* experiments are essential for probing the true active structure and building the fundamental structure-reactivity relationships. (iii) Although a catalyst should not be consumed during a chemical reaction, its local structure may alter during the reaction, usually leading to reactivity degradation. *In situ* experiments allow this degradation process to be monitored, providing insights on the catalyst deactivation mechanisms. As fundamental understanding of the reaction and deactivation mechanisms of model photocatalysts is pursued, developing specific *in situ* (S)TEM techniques for the study of photocatalyst nanoparticles is a necessary step.

To perform *in situ* experiments on photocatalysts, exposure of the specimen to light and water (vapor or liquid) is required. At times, exposure to other gases such as O_2 and H_2, as well as elevated or decreased temperatures is also desired, for the purpose of synthesizing model initial structure or suppressing contamination. In this work, an *in situ* light illumination system for an aberration-corrected environmental transmission electron microscope (ETEM) has been designed, built, and tested, which will be discussed in detail in Chapter 6. Control of the sample temperatures can be achieved by employing heating or cooling stages. The system used in this work to introduce a controlled gaseous environment around the sample is introduced below.

Standard operation of a TEM requires a high vacuum environment, typically at 10^{-7}-10^{-10} Torr, to prevent electron scattering by gas molecules and deposition of contaminating species onto the electron gun. Thus, reactive gases or liquids must be confined to the sample region of the microscope during *in situ* exposure. Methods applied to realize this scenario can be grouped into two categories, a windowed cell method, as well as a differential pumping method which is used in this work, depending on the confinement mechanism. For the windowed cell system, the standard specimen holder is modified so that the sample and the reactive gases or liquids are enclosed in between two non-porous, amorphous electron transparent windows such as carbon or SiN membranes. The advantages of this design include compatibility across different microscopes, capability of achieving ambient or higher pressures, and capability of introducing liquids around the sample to perform wet chemistry studies. Recent development of microelectromechanical system (MEMS) based windowed cell holders has enabled miniaturization of the gas volume and the integration of a heater, allowing atomic resolution to be achieved at ambient pressures and elevated temperatures (Creemer et al. 2008). The main limitations of this design, however, are that the sample geometry is constrained, images are affected by the interactions between the electrons with the two membranes, and the use of EDX is hindered because X-rays can be absorbed by the membranes.

On the other hand, the differential pumping design requires modification of the microscope column, in order to construct an environmental cell or a microreactor between the objective lens polepieces. The modified microscope is thus referred to as an ETEM. The first successful construction of an ETEM with atomic resolution is demonstrated by Doole et al. (Doole, Parkinson, and Stead 1991). Later, commercial ETEMs have been built based on the same concept. **Figure 2.12** shows a schematic of a differentially pumped column, where pressure limiting aperture sets are inserted in the bores of the polepieces, and a gas inlet and additional pumping systems with turbo molecular (TMP) or ion getter pumps (IGP) are added to the column. With this design, a relatively high gas pressure (usually less than 20 Torr) can be maintained in the sample region while the rest of the column stays under high vacuum. Gas conductance through the pressure limiting apertures depends on the aperture diameter and the gas mean-free path. In general, for a fixed pumping speed, the cell pressure increases with smaller aperture size and larger gas molecular weight (Wagner et al. 2012; Robertson and Teter 1998).

This design does not pose limitations on the specimen holder that can be used, allowing a variety of samples to be investigated. Also, it is potentially more favored to study detailed surface atomic structures of nanoparticles in an ETEM, compared to using a windowed-cell holder, as image contrast from the amorphous membranes is excluded. Spectroscopy data can also be acquired without the contribution from the membranes, especially EELS, which has been shown to be an excellent tool for quantifying the gas composition near the sample (Crozier and Chenna 2011). In addition, a residual gas analyzer can be used to qualitatively monitor the gas pressure and composition changes in the cell.

The capability of observing materials under near-reaction conditions in an ETEM is obtained at the expense of increased experimental complexity, as many factors need to be considered including electron scattering by the gas molecules and ionization of the gas species by the electron beam. In an ETEM, the gas(es) introduced into the environmental cell will fill the entire sample stage region therefore the electron-gas interactions are not spatially localized. In fact, for an FEI Titan 80-300 aberration-corrected ETEM, the distance between the first pair of pressure limiting apertures, which is also the electron path length through the high pressure region, is on the order of 7 mm (T. W. Hansen, Wagner, and Dunin-Borkowski 2010). Elastic and inelastic scatterings of the fast electron by the gas molecules in this region results in beam intensity loss and dampening of the contrast transfer, to some extent. In addition, with a relatively high electron current density, unwanted sample structural transformations may occur due to ionization of the gas molecules. In other words, the reactivity of the gas species is significantly increased by ionization, which may lead to etching or increased mobility of the atoms in the specimen. Generally speaking, lighter gas molecules, lower cell pressure and reduced beam current are desired to suppress the complex effects of the electron-gas interactions when studying specimen dynamics in the presence of reactive gas(es) (Thomas W. Hansen and Wagner 2012; Wagner et al. 2012).

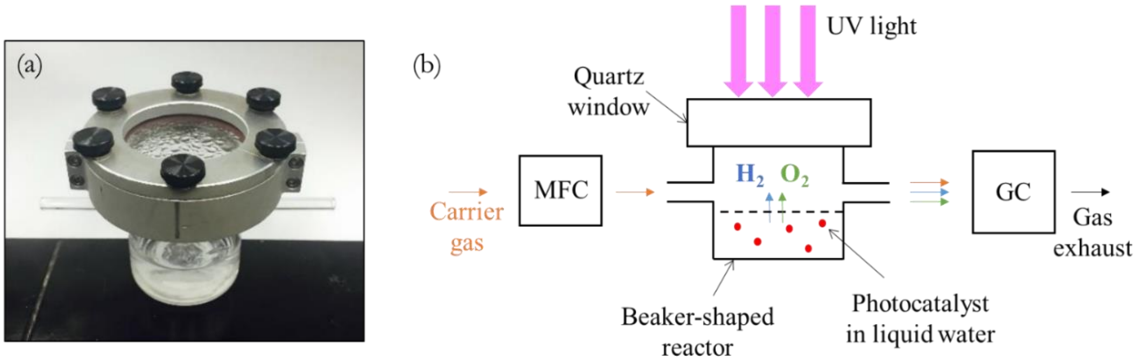

Figure 2.1: (a) A picture of the liquid phase photo-reactor. (b) Schematic of the photo-reactor system showing major components.

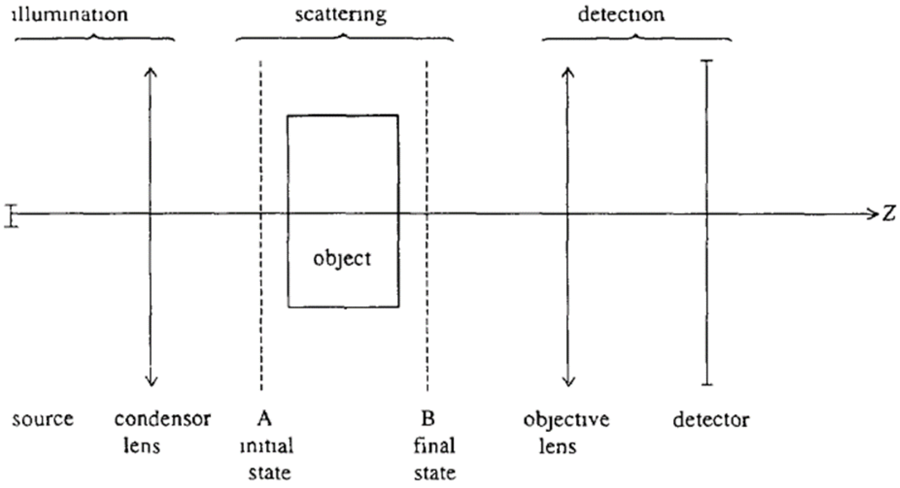

Figure 2.2: Schematic of an ideal scattering experiment (Van Dyck and de Jong 1992).

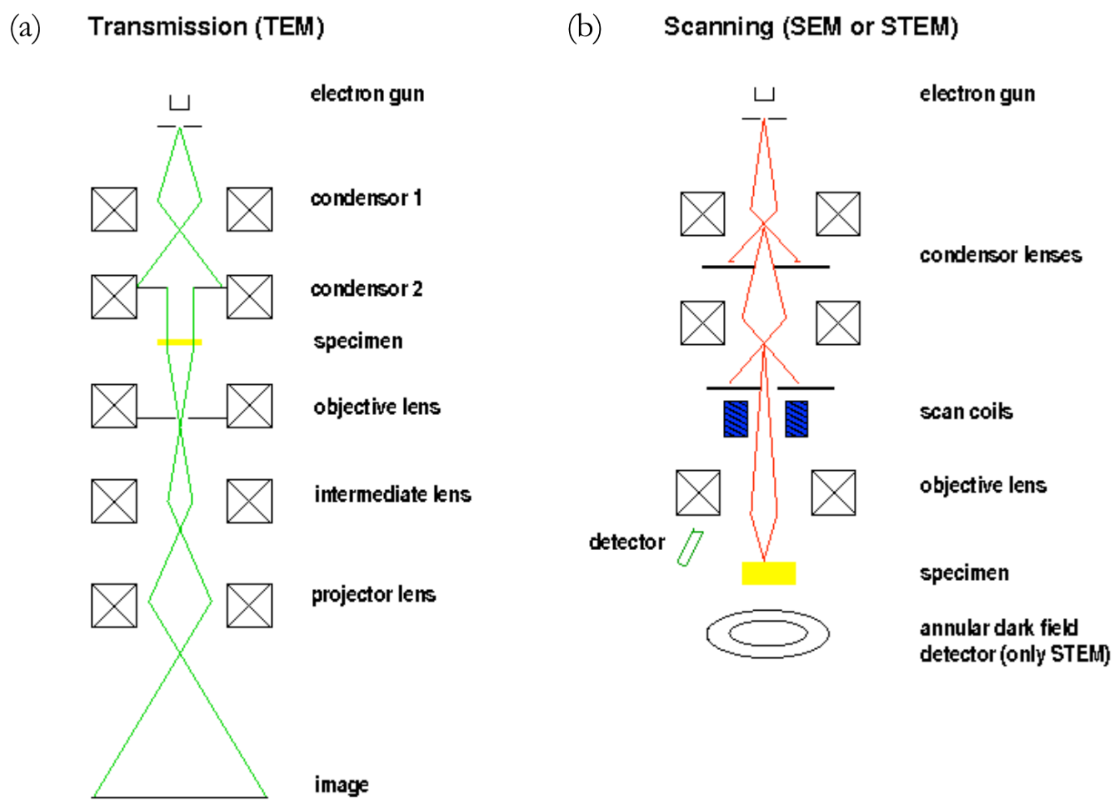

Figure 2.3: Operating principle of (a) a TEM showing broad illumination, and (b) a STEM showing focused illumination (Courtesy of Dr. Duncan Alexander).

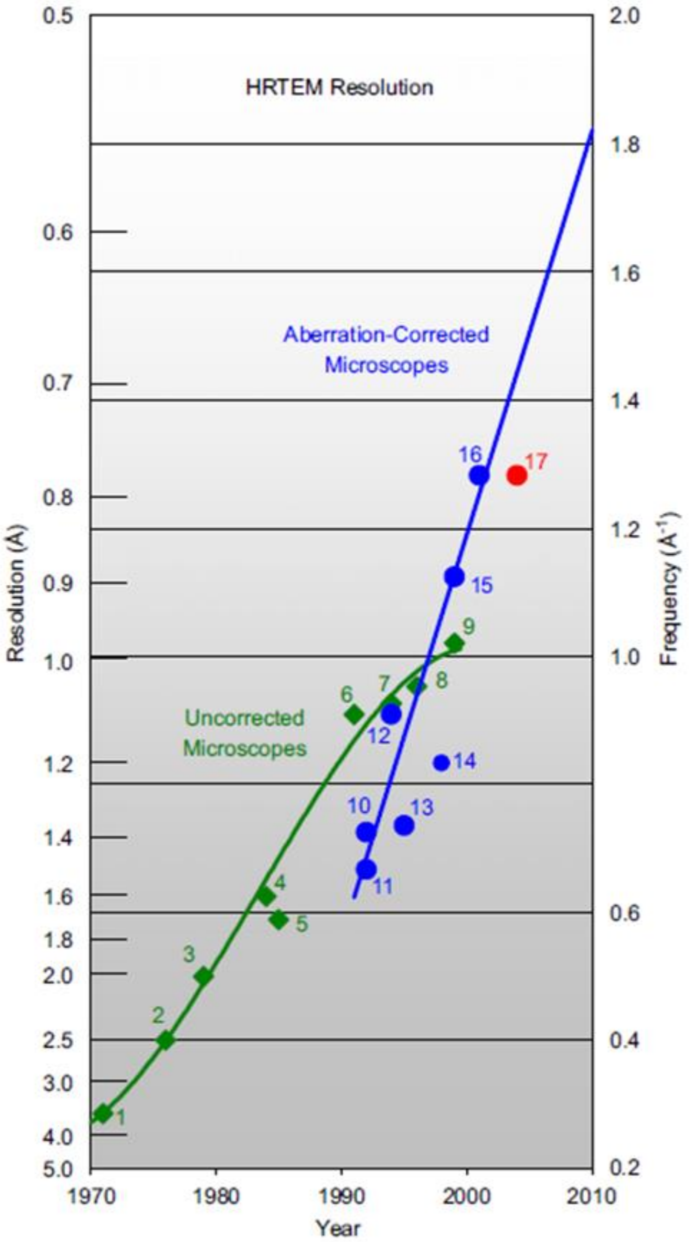

Figure 2.4: Progress in resolution improvement for high-resolution electron microscopy from 1970 to 2008. The resolution scale extends from 5 to 0.5 Å (left) and is linear in spatial frequency from 0.2 to 2 Å^{-1} (O'Keefe 2008).

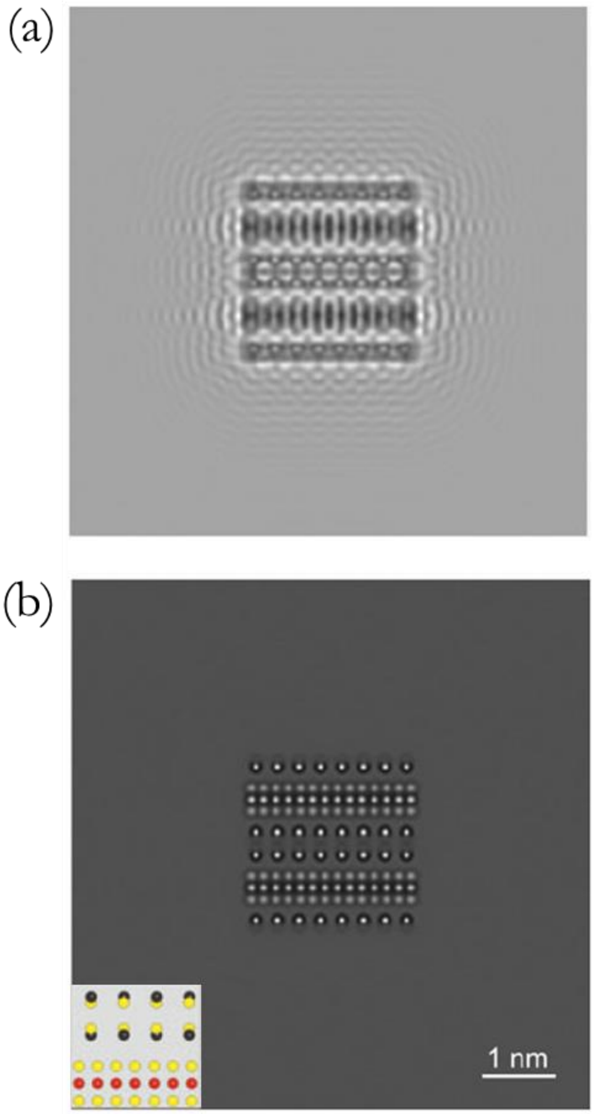

Figure 2.5: Illustration of the effect of image delocalization for a single unit cell (thickness: 3.2 nm) of $(PbS)_{1.14}NbS_2$ embedded in vacuum. (a) Simulation of a conventional TEM image at Scherzer defocus. (b) Corresponding simulation of an aberration-corrected TEM image at a NCSI condition, with the inset showing the projected crystal structure. More simulation details can be found in Spiecker et al. 2010.

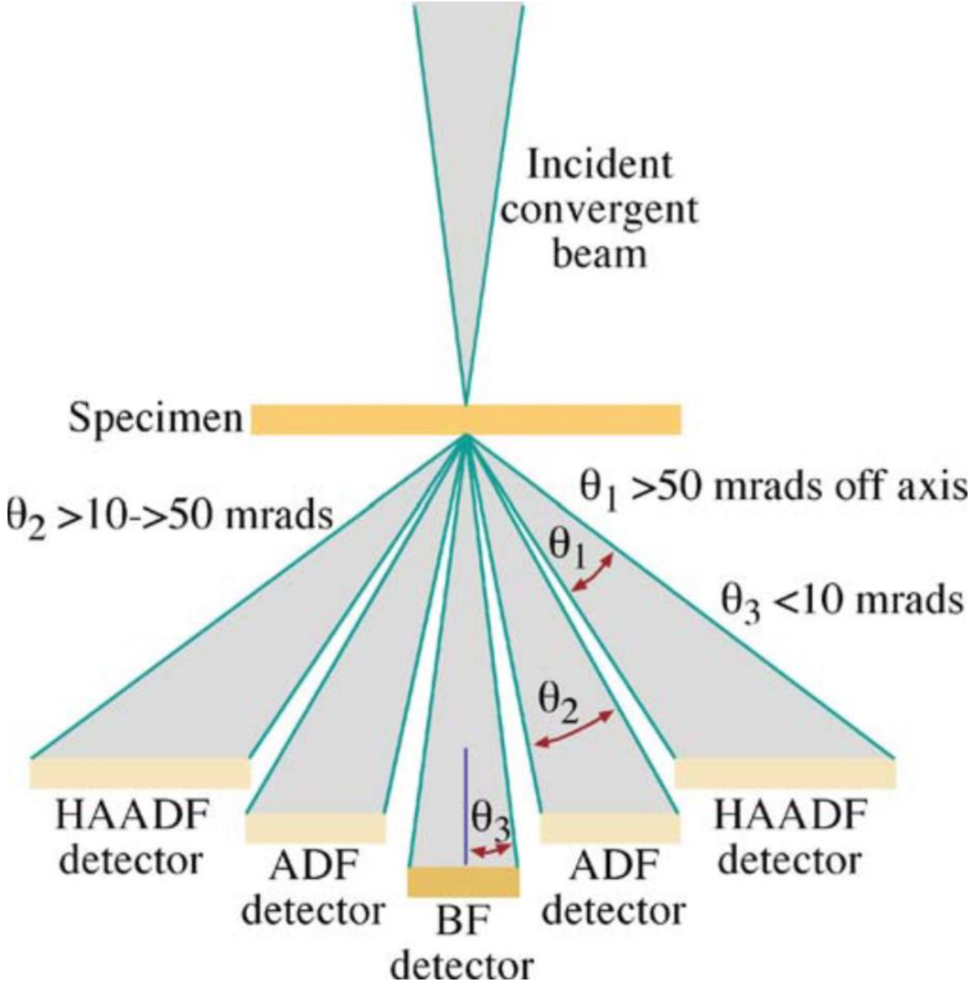

Figure 2.6: Schematic of the BF, ADF and HAADF detector set up in a STEM (Williams and Carter 2008).

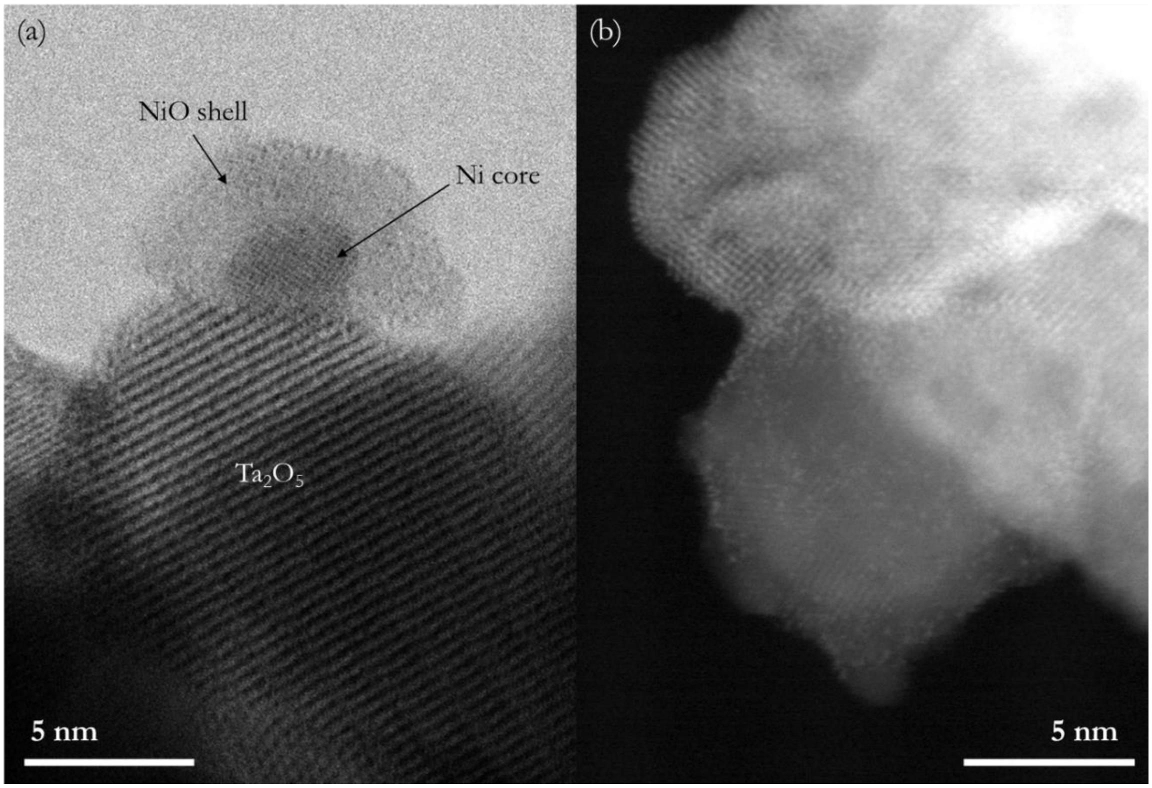

Figure 2.7: (a) BF and (b) ADF images of particles from initial and used Ni-NiO/Ta_2O_5 photocatalysts respectively, acquired using an aberration-corrected STEM (JEOL ARM200F).

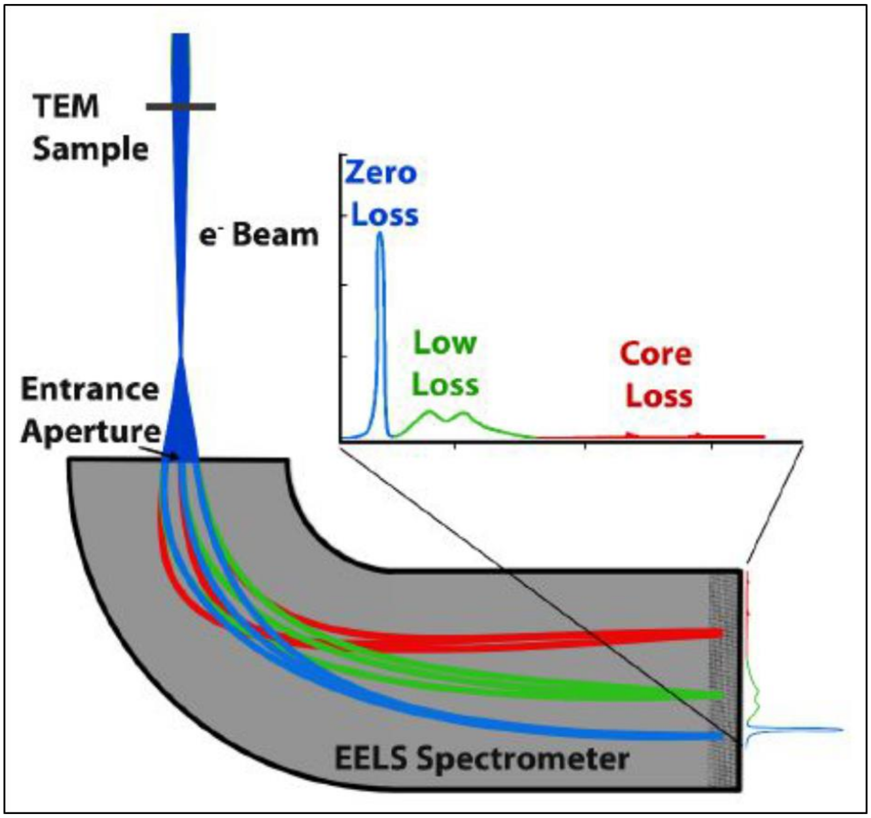

Figure 2.8: Schematic of the working principles of EELS with a magnetic prism spectrometer. Colors represent the relative energies of electrons after they interact with the sample. Image from (Crozier and Miller 2016).

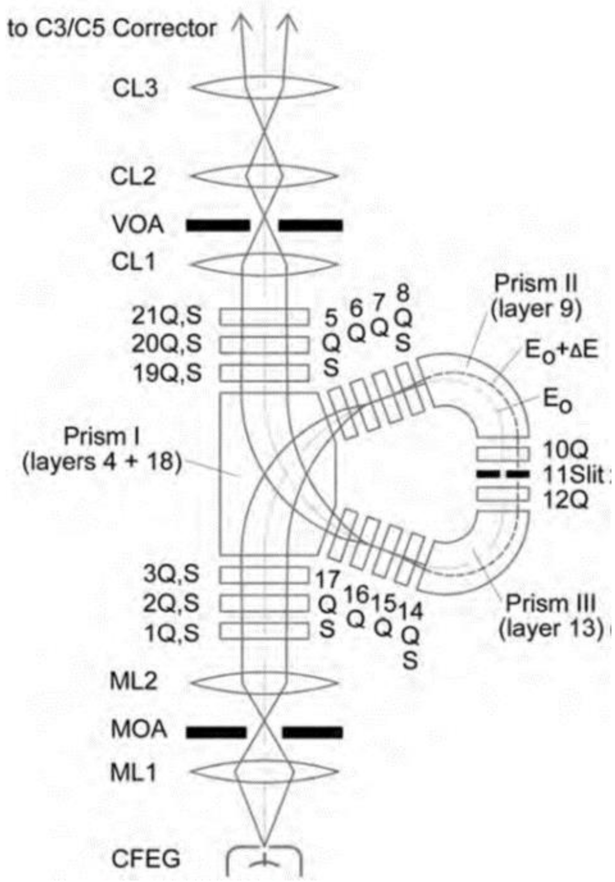

Figure 2.9: Schematic cross-section of the monochromator part of the STEM column (Krivanek et al. 2013).

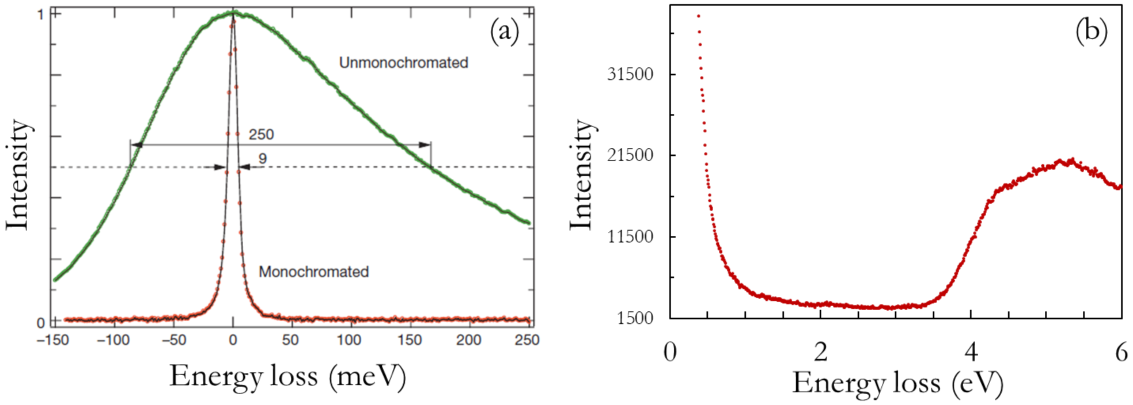

Figure 2.10: (a) A 9 meV wide (FWHM) monochromated ZLP compared to the energy distribution of an unmonochromated beam produced by the microscope's cold FEG (Krivanek et al. 2014). (b) A typical monochromated EEL spectrum from anatase nanoparticles showing the bandgap region, acquired using an aberration-corrected NION UltraSTEM 100.

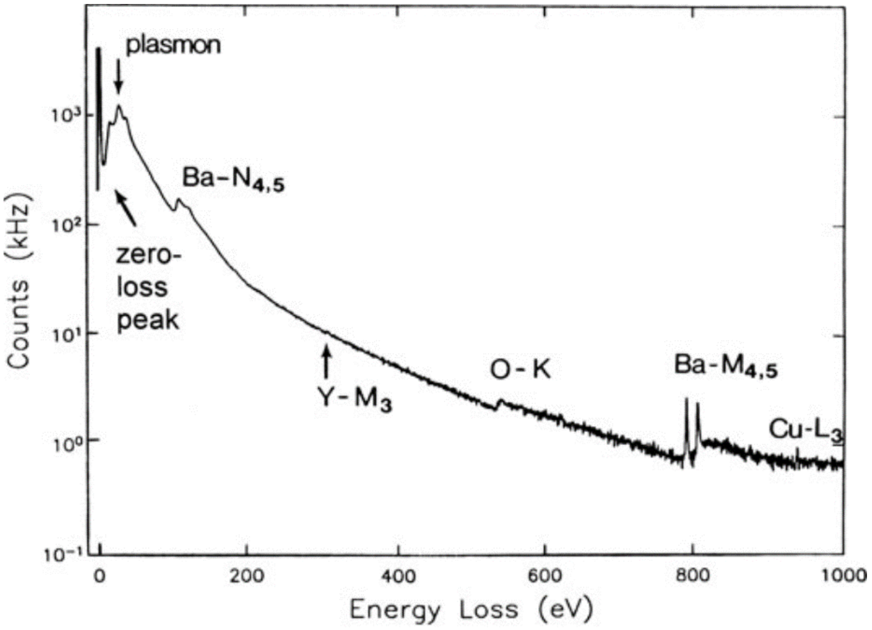

Figure 2.11: EEL spectrum of a high-temperature superconductor ($YBa_2Cu_3O_7$) with the electron intensity on a logarithmic scale, showing zero-loss and plasmon peaks and ionization edges arising from each element. Image from (Egerton 2011). Courtesy of D.H. Shin, Cornell University.

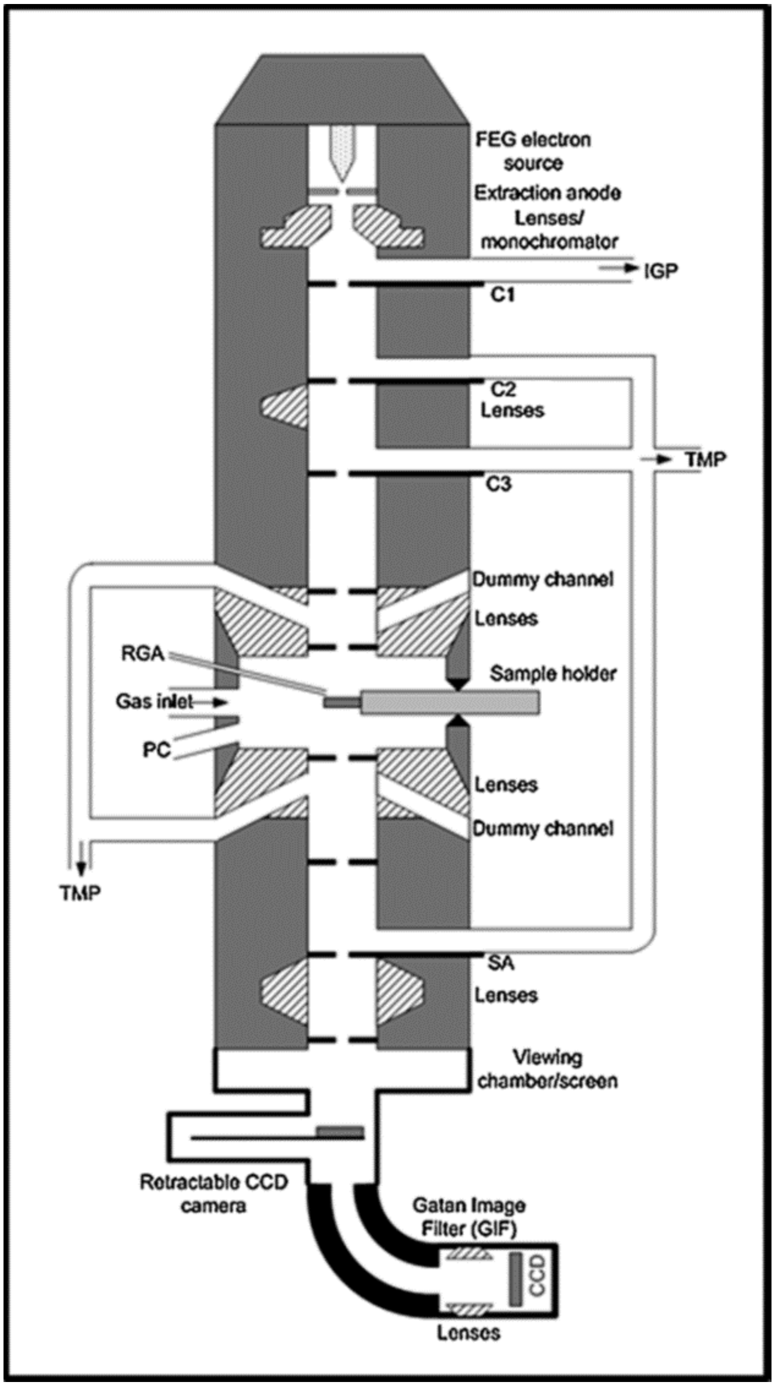

Figure 2.12: Schematic of a differentially pumped TEM column (Wagner et al. 2012).

3 Structure-reactivity Relationships of Ni-NiO Core-shell Co-catalysts on Ta_2O_5

3.1 Motivation

As discussed in section 1.1, it is potentially attractive to utilize sunlight and water, which are ultimately clean and abundant, to produce energy without contributing to greenhouse gas emission, through photocatalytic water splitting. In one approach, a light harvesting inorganic semiconductor with valence and conduction band edges that straddles the electrochemical potentials for water reduction and oxidation is employed (S. Chen and Wang 2012). This semiconductor must be stable under reaction conditions and not undergo photocorrosion. Furthermore, suitable co-catalysts are added to the surface of the semiconductor which provide reaction sites and decrease the water reduction/oxidation activation energies resulting in significant improvement of the photocatalytic activity (Maeda and Domen 2010).

Tantalum oxide and many tantalite-based systems, which have a band gap of about 4 eV, have been reported to show extraordinarily high activities and quantum yields when decomposing water under ultraviolet (UV) illumination (Kato, Asakura, and Kudo 2003; Kudo and Miseki 2009; P. Zhang, Zhang, and Gong 2014). Although pure tantalum oxide shows some photocatalytic activity, loading with a nickel-based co-catalyst improves the initial H_2 production rate by 3 orders of magnitude and results in stoichiometric decomposition of pure water into H_2 and O_2 (Kato and Kudo 1998). Interestingly, in order to have high activity, this co-catalyst has to undergo a pre-treatment consisting of a full thermal reduction in hydrogen followed by partially re-oxidation creating a Ni core-NiO shell morphology. Moreover, noble metal covered with a Cr_2O_3 layer, which has a similar metal core-oxide shell structure, is also a very efficient co-catalyst for overall water splitting. It is argued that this co-catalyst structure will not only catalyze the forward reaction but also suppress the backward reaction in which water is formed by combing H_2 and O_2 (Maeda and Domen 2010; M. Yoshida et al. 2009).

A detailed atomic-level understanding of the relationship between the catalyst microstructure and the photocatalytic reactivities has not yet been fully explored. Transmission electron microscopy (TEM) is a powerful approach to elucidate atomic level structure and composition providing a nano-level view of the evolution of the catalysts. Correlating the microstructures of the semiconductor, co-catalyst and their interfaces with reactivities should give insights on both reaction and deactivation mechanisms.

In this work, a series of different Ni core-NiO shell co-catalysts were prepared on Ta_2O_5 substrate particles. The catalytic behavior of the material may be greatly influenced by changes in the co-catalysts microstructure. One way to modify and tune the co-catalysts structure is by changing the heat treatment conditions during the preparation of the material. This provides an opportunity to correlate changes in activity with relatively well-defined changes in structure allowing fundamental information on structure-reactivity relations to be determined. The photocatalytic activities of all the co-catalysts were measured and compared. TEM was employed to directly observe the changes of the microstructure of the material. By varying the co-catalyst structure in a controlled way and correlating the photocatalytic activity with the structure of both fresh and de-activated photocatalysts, we can obtain a deeper insight on structure-reactivity relationships. The fundamental information derived from these experiments can provide guidance to future improvements in the design of the co-catalyst structure and composition.

3.2 Experimental

3.2.1 Materials Preparation

NiO (1 wt %) was loaded on Ta_2O_5 photocatalyst powders (Aldrich; 99.99%) using an impregnation method from an aqueous solution of $Ni(NO_3)_2 \bullet 6H_2O$ (Aldrich; 99.999%). Different subsequent heat treatments were conducted to vary the co-catalyst structures: Sample (i) was reduced at 500 °C with flowing 5% H_2/Ar for 2 h; Sample (ii), (iii) and (iv) were first reduced under the same condition as sample (i) and then partially oxidized in 200 Torr of O_2 for 1 h at 100, 150 and 200 °C respectively; Sample (v) was oxidized at 500 °C with flowing O_2 for 2 h. The reduction and oxidation steps for the heat treatments are summarized in **Table 3.1**.

3.2.2 Photocatalytic Test

The photo-reactor system described in section 2.1 was used primarily in the continuous flow set up to perform the reactivity measurements. A GC Varian 450 (PLOT column, TCD, Ar carrier) is employed to detect the H_2 gas production rates. In a typical test, about 0.08 g of catalyst was suspended constantly in 40 mL of pH 7 DI water using a magnetic stirrer at room temperature. The sealed system was first purged with Ar gas for 20 - 40 min until no residual air was left in the system as demonstrated by the absence of air peaks in the GC spectrum. The suspension was then irradiated from the top by a xenon lamp (Newport) with a mirror selecting the wavelengths from 260 nm to 320 nm. The incoming photon flux was 21.5 mW/cm^2. The photo-reactor system was set up to be in the form of continuous flow, the H_2 and O_2 gases released from water were constantly carried away by flowing Ar gas and every 10 min the gas mixture was sampled in GC. An H_2 calibration was obtained by measuring peak intensities from H_2/Ar mixtures of well-defined compositions and flow rates. Therefore, H_2 production rate at each time point can be calculated and plotted. This particular system had very poor sensitivity to O_2 gas because of both the design of our flow reactor and because Ar was used as the carrier gas, thus most of the results shown here only focus on H_2 evolution.

Theoretically the O_2 production should be half of the H_2 production during water splitting. To test that hypothesis, the photo-reactor system was employed in the recirculation set up measuring both H_2 and O_2 productions from sample (iv). In this test, 0.41 g catalyst was suspended in pH 7 DI water and a GC Varian 3900 (PLOT, TCD, He carrier) was used to measure the accumulated gases every 3 min. Typical gas chromatograms can be found in section 8.1.

3.2.3 TEM Characterization

An aberration corrected FEI Titan (300 KV) was used to examine the atomic structure of the co-catalyst on Ta_2O_5. The fresh powder catalysts were first imaged before any catalytic tests were conducted. After exposure to water and UV light, the same materials were again imaged to determine the structural evolution that took place under photoreaction conditions.

3.3 Results

3.3.1 Photocatalytic Activity

Figure 3.1a shows the H_2 production rates of the catalysts as a function of time after starting the UV illumination. After the UV light was turned on, significant H_2 was detected within 10 min and it usually took 20-30 min for the H_2 production rate to reach its maximum. This incubation behavior was believed to be partly associated with the time needed for the evolved H_2 to be mixed with the flowing Ar in the head space above the water and carried to the GC. Sample (v), which was oxidized to NiO at 500 ºC, showed no activity. Sample (i) to (iv), produced H_2 at different rates but showed similar variations in activity with time. Sample (i) has the lowest H_2 production rate (64 mol/h/g), while sample (iv) had the highest by a factor of 3 (189 mol/h/g). Sample (i) - (iii) de-activate in the same way with their activities dropping by 50% in 140 min. Interestingly, in addition to having the highest activity, sample (iv) showed a much longer deactivation time and took 360 min to drop to 50% of the maximum activity (**Table 3.2**). There was about 3.8 μmol (0.2 mg) Ni loaded on sample (iv) initially and 389.6 μmol H_2 was produced till the catalyst deactivated to 20% of its maximum activity. Thus, an estimation can be made that 1 mg initial Ni co-catalyst should at least generate 1950 μmol H_2 before the activity drops to zero. Furthermore, pH values of a suspension of sample (iv) in water before and after exposure to UV light for 5h were measured and they were both in the range of 7 - 7.5.

3.3.2 Initial Catalyst Structures

Figure 3.2 shows the variation in the structures of the initial co-catalysts for the 5 materials. Although sample (i) was not oxidized at elevated temperature in the furnace, it was exposed to air and small nickel oxide domains were formed on parts of Ni metal surfaces confirmed by fast Fourier transform (FFT) (**Figure 3.2a**). The catalytically activity arises because of the existence of both metallic and oxide phases via the mechanism discussed in section 3.4.1. As the oxidation temperature goes up, sample (ii) and (iii) show typical core-shell structures where the oxide shell covers the entire Ni metal core in most of the particles. Twin boundaries can often be observed in the metal phase. Sample (iv) shows the most complicated structure where the metal core and the oxide shell are difficult to differentiate presumably because of the low contrast difference between the smaller metallic Ni phase against the larger NiO phase.

However, FFT analysis of the high resolution transmission electron microscopy (HRTEM) images reveals that both metal and oxide phases are present. Since sample (v) was oxidized at high temperature with no reduction step, NiO particles arise on the surface of Ta_2O_5 with NiO (200) planes present as the surface termination facets.

The particle sizes and the oxide shell thicknesses were measured from the HRTEM images for each catalyst, with average values and errors listed in **Table 3.2**. The errors come from the heterogeneity of the co-catalyst morphology. Generally speaking, the average particle size as well as the oxide shell thickness increased with increasing oxidation temperature. More specifically, comparing sample (i), (ii) and (iii), a rise in oxidation temperature results in a small change in particle size and oxide shell thickness. Interestingly, this was accompanied by an almost three times increase in the maximum H_2 production. For sample (iv), a further increase in oxidation temperature results in significant particle growth and a thicker oxide shell but little increase in the maximum H_2 production rate. However, this sample showed improved long-term stability with a significant increase in the time for the activity to drop by 50%.

As the oxidation time associated with catalyst preparation increases, the interfaces between Ta_2O_5 (which has an orthorhombic structure) and the Ni-NiO (which have cubic structures) core-shell becomes more complex and difficult to clearly observe. Thus, careful interface analysis was conducted on sample (i) where the interfaces between Ta_2O_5 and Ni metal could be viewed in projection without NiO overlayers. The Ni metal/Ta_2O_5 orientational relationship and interface structure determined from this sample should be similar to those in the gently oxidized samples assuming the buried Ni metal/Ta_2O_5 interface does not significantly change. The average contact angle of between the Ni and Ta_2O_5 (as demonstrated in **Figure 3.3a**) is $87 \pm 9^{\circ}$ for this sample. A typical interface structure is shown in **Figure 3.3b** where the relative angles between Ni and Ta_2O_5 lattice fringes are commonly observed. The two flat interfaces are parallel to two sets of Ta_2O_5 lattice fringes with d-spacings of 2.42 Å and 1.67 Å respectively. The longer interface is almost parallel both to the Ni (111) plane in the metal particle and Ta_2O_5 (201) plane in the substrate, and it is extended over a distance of 10.6 nm suggesting that it is an energetically favorable configuration. The low interfacial energy together with the fact that samples (i)-(iv) have high activities, suggests that this coherent interface structure helps with the electron transfer from Ta_2O_5 substrate to Ni metal co-catalyst.

3.3.3 Used Catalyst Structures

The deactivation mechanism was investigated by comparing the initial and used catalyst structures of samples (i) and (iv). **Figure 3.4** shows the morphology and phase changes of sample (i) after exposure to UV light and water for 140 min during which the catalytic activity dropped to about 35% of its maximum value. Faceted surface nanodomains (**Figure 3.4a**) and a cluster of multiple blocky nanodomains (**Figure 3.4b**) are observed in the co-catalysts. The changes appear to be correlated with the drop in activity. The morphological similarity suggests that **Figure 3.4a and Figure 3.4b** are respectively snapshots of the earlier and later stages of structural evolution associated with deactivation. FFT analysis of both structures showed that the faceted surface domains and the cluster are NiO with (200) surface termination planes. In addition to forming a cluster, NiO nanodomains were also found finely dispersed on the surface of the Ta_2O_5 (shown in section 8.2). It should be noted that during catalyst preparation, formation of NiO phase as shells covering the Ni metal particles results in reactivity improvement, whereas the formation of NiO nanoblocks when catalysts are immersed in water and exposed to light leads to deactivation. Also, although the surface termination of NiO nanoblocks formed during deactivation is the same as that of NiO particles formed during thermal treatment in sample (v), they have very different morphologies and particle sizes. It is speculated that during deactivation, surface sites on Ni metal are highly heterogeneous for NiO nucleation and growth. Each active nucleation site will form a NiO nanodomain and at ambient temperature, these NiO nanodomains do not sinter or grow into large particles.

After sample (iv) has been exposed to water and UV light for 16 h, the catalytic activity dropped to 20% of the maximum value. Various changes were observed (see section 8.2) but the two most dramatic structural changes were: (1) Formation of NiO nanodomain cluster (**Figure 3.5a**) as observed in sample (i); (2) evolution of void-shell structures in which the Ni metal core disappeared leaving a hole in the center of the NiO shell (**Figure 3.5b**). Some Ni metal was still present in some areas of the used co-catalyst particles and was presumably the reason for continued H_2 production albeit at a lower level.

Similar structures and morphologies were observed to be associated with the deactivation in all of the catalysts. As illustrated by sample (i), Ni metal particle is first oxidized to NiO nanodomain on the surface. Then the entire particle changes to multiple NiO nanoblocks. Even with the protection of NiO shell in sample (ii) to (iv), this type of transformation still occurred during deactivation. The void-shell structure was less frequently observed here than nanoblocks but it was still a significant morphology associated with deactivation observed on a Ni-NiO/TiO_2 system (L. Zhang et al. 2015).

Interestingly, some used co-catalyst particles did not show obvious structural changes, which may imply that there was no significant charge transfer from the Ta_2O_5 to the Ni-NiO at these sites preventing the Ni metal core to be oxidized. This could be due to a less efficient interface structure for charge transfer, or that the local Ta_2O_5 structure does not support long electron-hole recombination lifetime. As discussed in section 1.2.2, charge transfer and recombination are greatly affected by the interfacial and substrate crystal structures, which show high degree of heterogeneity in the nanopower system. Such variations in the used co-catalyst structures as well as the local crystal structures can only be probed using high spatial resolution techniques such as TEM imaging, which provides a possible route for connecting the fundamental structural characters with undesired carrier kinetics.

3.4 Discussion

3.4.1 Core-shell Water Splitting Mechanism

The Ni-NiO core-shell structure is believed to help with charge separation and catalyzes the forward water splitting reaction while kinetically limiting the reverse reaction. The process is initiated when the incoming photon (with energy greater than the bandgap of 4.2 eV) is absorbed by the Ta_2O_5 light harvesting material and electrons are excited into the conduction band generating electron-hole pairs. The electrons and holes either recombine or go to different surface reaction sites and may contribute to H_2 and O_2 evolution on the catalyst surface (S. Chen and Wang 2012; Walter et al. 2010). As shown in **Figure 3.6a**, the band alignment of the Ta_2O_5, NiO and Ni provides a thermodynamic driving force for the photo-generated electrons to go to the Ni metal, whereas the holes are driven to the valence band of NiO (Chun et al. 2003; Caspary Toroker et al. 2011). This is supported by the work of Townsend et al. who showed that Ni serves as an electron trap (water reduction site) and NiO serves as a hole trap (water oxidation site) by photovoltage and other experimental measurements (K. Townsend, D. Browning, and E. Osterloh 2012; Kato, Asakura, and Kudo 2003).

In addition, Townsend et al. also showed that by forming a core-shell structure rather than having spatially isolated Ni and NiO particles on the surfaces of the light harvesting semiconductor, the photocatalytic reactivity increases by an order of magnitude (K. Townsend, D. Browning, and E. Osterloh 2012). Similar core-shell structure is present in the noble metal-Cr_2O_3 co-catalyst system (as previously mentioned in section 1.2.3) (Maeda and Domen 2010; M. Yoshida et al. 2009) and the Cr_2O_3 shell is proposed to function as a protective layer to prevent the backward reaction between H_2 and O_2. The NiO shell may also work as a protective layer, leading to the higher reactivity of the core-shell structure. In fact, Ni metal can catalyze both the water reduction reaction and the water formation reaction (when it is in contact with both H_2 and O_2) while NiO has been reported to show inhibition behavior for water formation reaction (Matsumoto et al. 2004; K. K. Hansen 2008). The protective mechanism of the core-shell structure is illustrated schematically in **Figure 3.6b**. In this system, only the NiO surface is exposed and in contact with water whereas the Ni metal surface is buried below the oxide shell. Protons diffuse through the NiO shell and reach the buried Ni-NiO interface, get reduced to H_2 by the photo-generated electrons accumulated in Ni metal. The evolved H_2 molecules then diffuses out through the NiO shell. Meanwhile, O_2 is generated on the surface of NiO by oxidizing H_2O/OH^- using the photo-generated holes. It is easy for oxygen to leave the NiO surface and go into solution. Moreover, oxygen cannot diffuse rapidly through NiO and as a result, O_2 is inhibited from reacting catalytically with H_2 on the Ni metal surface to reform water. Thus, the reverse reaction is suppressed.

This mechanism suggests an interpretation for why the photocatalytic activities change significantly with varying the extent of oxidation during the catalyst preparation, as illustrated in **Figure 3.1b**. The increase in the photocatalytic activities from sample (i) to (iv) results from the increase in the NiO shell thickness which appears to be associated with greater suppression of the reverse reaction. An optimization of the co-catalyst particle size as well as the oxide shell thickness is desired to give the best activity. From this work, the optimum appears to be a particle size of ~20 nm or larger with an oxide shell thickness percentage of 30-40%.

Comparison with Ni-NiO/TiO₂

Ni-NiO core-shell co-catalyst has also been loaded onto anatase particles and the detailed work is described in this reference (L. Zhang et al. 2015). Although H_2 production was detected from the Ni-NiO/TiO_2 system, it was produced via a photochemical rather than a photocatalytic reaction, involving dissolution of Ni. Specifically, Ni may donate electrons to protons and produces hydrogen, i.e.

$$\mathbf{Ni\ (metal)} - 2e^- = Ni^{2+} \quad or \quad Ni(metal) + 2h^+ = Ni^{2+} \qquad 3.1$$

$$2H^+ + 2e^- = H_2 \qquad 3.2$$

Using inductively-coupled plasma mass spectroscopy (ICP-MS), it was found that the amount of Ni released into solution matched the amount of H_2 production. Therefore, when this Ni-NiO/TiO_2 system is dispersed in pure water and exposed to UV light, photocorrosion of Ni metal phase takes place generating H_2 from water.

On the contrary, for Ni-NiO/Ta_2O_5 system, this photochemical mechanism can be mostly discounted by comparing the number of metallic Ni atoms with the number of molecules of H_2 produced. If we assume that this photochemical reaction is responsible for all the H_2 produced, the total moles of produced H_2 can be estimated based on the amount of initially loaded Ni metal on each sample as shown in **Table 3.3**. As the oxidation temperature increases, more Ni is oxidized to NiO so the initial Ni metal decreases from sample (i) to (iv) leading to a drop of estimated H_2 production. In contrast to this prediction, the H_2 produced increases dramatically in the experiments as the Ni metal content decreases. In the case of sample (iv), the amount of H_2 detected is 2 orders of magnitude higher than the predicted amount of H_2 from the photochemical reaction. Therefore, at least for this sample, the photochemical contribution to H_2 production from the mechanism outlined above is negligible.

To further investigate the reaction mechanism of sample (iv), a recirculation set up of the photo-reactor system was used to detect both H_2 and O_2 productions. As shown in **Figure 3.7a**, gas production continuously increased for over 230 min after the light was turned on (H_2 measurements are very noisy because of the low H_2 sensitivity in this set up). At the initial stage of the reaction, the H_2 to O_2 ratio is >3, which then drops to about 2.56 after ~90 min reaction time (**Figure 3.7b**). This deviation from the stoichiometric ratio suggests that other types of photochemical reactions are present as side or sacrificial reactions apart from the photocatalytic water decomposition reaction, generating excessive H_2 or consuming the photogenerated holes leading to suppressed O_2 production. Excessive H_2 may be generated through possible reactions associated with catalyst deactivation (Eq. 3.1-3.3), which are discussed later. On the other hand, consumption of holes have been argued to be the reason for similar behavior observed in a Ni-NiO/$SrTiO_3$ system, where NiO is argued to transform to $Ni(OH)_2$ when exposed to water, which is then oxidized to NiOOH by the holes (Han et al. 2017). The specific sacrificial reaction occurred in Ni-NiO/Ta_2O_5 system is beyond the scope of this study, but the large production of H_2 and O_2 strongly suggests that this system can actually catalyze water splitting.

Comparing these two systems reveals that loading the same type of co-catalysts onto two different substrates can lead to dramatically different reaction mechanisms. Two possible reasons are proposed below for the photocatalytic behavior of Ni-NiO/Ta_2O_5 instead of the photochemical behavior of Ni-NiO/TiO_2.

(1) The difference may come from the different electronic structures of Ta_2O_5 and TiO_2. The CB/VB edge of Ta_2O_5 is more negative/positive than those of TiO_2, thus the electrons and holes generated in Ta_2O_5 possess higher electrochemical potentials. Based on the Marcus-Gerischer theory, it is expected that an increase in the potentials, which means higher thermodynamic driving force, usually leads to faster rate for interfacial charge transfer and water electrolysis (Marcus 1964; Gerischer 1990).

(2) The co-catalyst morphologies and interface structures may also be responsible for the different reaction mechanisms. Although the impregnation and heat treatment methods involved in synthesizing the two systems are very similar, many factors may still alter the resulting catalyst structures, including the dispersion of the $Ni(NO_3)_2 \bullet 6H_2O$ precursor on the substrate surfaces, and the interaction between the substrate material with Ni-NiO during the heat treatments. Differences in particle size, core-shell morphology and interface structures in the two systems need to be analyzed to draw a conclusion.

3.4.2 Deactivation

A common factor in both the blocky and void-shell structure transformations is the loss of the Ni metal phase. As a result, the electrical contact between the metal and semiconductor is lost and thus the number of surface reduction sites decreases leading to the drop in H_2 production rate over time. On the contrary, there was no obvious corrosion of the NiO shell, which may suggest that the Ni loss is independent of pH along with the fact that the pH of the suspension stayed in the range of 7 - 7.5 during the reaction. Interestingly, **Figure 3.1b** shows the reaction time for 50% max reactivity depends almost linearly on the oxide shell thickness based on the analysis of sample (ii) to (iv). It was also observed that exposure of the catalyst to just water in the absence of UV illumination resulted in no significant change in the structure and activity even after several hours, suggesting the deactivation is associated with a light driven diffusion controlled process.

The loss of Ni metal can be explained by two likely mechanisms:

(A) Photocorrosion of Ni metal in which Ni ions dissolve into the surrounding water (Eq. 3.1). This can be associated with the void-shell formation if the NiO shell is preserved, or the NiO nanoblocks formation if the NiO shell breaks down and changes its morphology. The amount of NiO should not change before and after deactivation for this mechanism.

(B) Oxidation of Ni metal core to NiO phase. A volume expansion will be associated with this transformation, which could result in local stresses and form NiO nanodomains. In this case, the amount of NiO on the used catalysts would increase.

The initial native NiO shell in sample (i) was very thin but still lots of NiO nanoblocks were found on the used catalyst suggesting that mechanism (B) actually dominates for this sample. This is in part consistent with the observations made from the Ni-NiO/$SrTiO_3$ system, where Ni metal core appears smaller and NiO shell appears thicker after illumination (Han et al. 2017). Whether mechanism (A) or (B) dominates for sample (ii) to (iv) remains unclear.

As discussed previously, complicated competitive redox reactions may occur in the presence of light and water leading to a rise in the Ni oxidation state. Apart from the photochemical reaction listed in Eq. 3.1, the holes accumulated in the NiO phase may also result in oxidation of Ni metal. One possible reaction is listed below:

$$\mathbf{2Ni} + \boldsymbol{2h^{+}} + \boldsymbol{2OH^{-}} = \boldsymbol{2NiO} + \boldsymbol{H_2} \text{ (Mechanism (B))} \qquad 3.3$$

For these competitive reactions to occur, certain Ni diffusion must occur to bring Ni into contact with the oxidizing agent and other reactants. Three possibilities are discussed here for facilitating the diffusion processes. The first mechanism is that the H_2 formed at the interface between Ni and NiO may accumulate leading to stress build up resulting in cracks formation and growth in the NiO shell. Ni may then be oxidized via contact with water or the produced O_2 molecules. However, this is less likely to occur based of the data obtained from sample (ii) and (iii). The H_2 production of (iii) is nearly twice as much as that of (ii) which would lead to faster crack formation and growth in NiO. Also, the average oxide shell thickness/particle size percentages of these two samples are similar thus the deactivation time for sample (iii) should be faster. This hypothesis is contradicted by the observation that the reaction time for 50% max reactivity of sample (iii) is 20 min longer.

The second possibility considers a Kirkendall type diffusion. The transformation of initial Ni-NiO to a void-shell structure has been previously observed by Chenna et al. in an *in situ* TEM work where Ni metal nanoparticles were oxidized in a well-controlled environment at elevated temperature. The resulting NiO shell structure was explained via a Kirkendall mechanism since the diffusion coefficient of Ni cations along the NiO grain boundaries is 8 orders of magnitude higher than that of O anions at 400°C (Chenna and Crozier 2012; Atkinson and Taylor 1978; Atkinson et al. 1986; Peraldi, Monceau, and Pieraggi 2002). This mechanism seems likely for producing the hollow NiO shell observed in the deactivated materials. In the current work, the calculated local temperature rise of Ni metal from absorption of the incident light is ~103 K/s. However, this excess heat can be carried away by the surrounding oxide thus the co-catalyst stayed at ambient temperature during water splitting. The thermal diffusion rate for both Ni cations and O anions at room temperature is negligible thus the formation of deactivated void-shell structure in this work is not a thermal effect. The following question is: could this be a light driven Kirkendall process where the incident light drives Ni diffusion through the NiO shell? Previous investigation of the Ni-NiO/TiO_2 system conducted by Liuxian Zhang suggests that this is also unlikely, as the Ni-NiO co-catalyst exposed to light and water vapor inside an ETEM (FEI Tecnai F20) for 16 h did not result in the Kirkendall type diffusion of the Ni phase (**Figure 3.8**).

The last possibility is that the NiO shell may contain micropores resulting from the thermal treatment during catalyst preparation, or from partial transformation to $Ni(OH)_2$ when immersed in liquid water (Domen et al. 1986; Han et al. 2017). The presence of micropores in the shell was an important hypothesis when reaction mechanism was proposed for the noble metal-Cr_2O_3 system, which determined the higher permeability for H_2 over O_2 of the shell (discussed in section 1.2.3) (M. Yoshida et al. 2009). Similarly, for the Ni-NiO system, these micropores may serve as diffusion channels for the H_2 produced at the buried Ni metal surface to migrate out through the NiO shell. However, it may also provide diffusion pathways for H^+ and OH^- to permeate the NiO shell and get into contact with Ni. The incident light deposits energy into the system which triggers the deactivation reactions listed before. This hypothesis has been tested on the Ni-NiO/TiO_2 system, using an etchant (0.07 M H_2O_2 + 0.07 M HCl) which can etch away a 0.12 g Ni wire within 24 h but cannot etch the same Ni wire with a NiO layer developed at 700 ^{o}C for 1h in air. As shown in **Figure 3.9**, after immersing Ni-NiO/TiO_2 catalyst powder in this etchant in dark for 15 min, loss of Ni metal phase with the presence of void-shell structure is observed, suggesting micropores actually exist in the NiO shell after catalyst preparation. This conclusion may also be applied to the Ni-NiO/Ta_2O_5 system due to the similar synthesis methods used.

3.5 Summary

Ni-NiO core-shell co-catalyst structures on Ta_2O_5 have been investigated for solar H_2 production. Core-shell co-catalysts with different morphologies were produced by varying the heat treatment conditions during catalyst preparation. The morphological changes resulted in large changes in photocatalytic activity. The presence of Ni metal phase is indispensable for the catalytic reactivity while increased H_2 production was found to be related to an increase in the thickness of NiO shell, due to suppression of the back reaction. The best catalyst made so far should at least generate 1950 μmol H_2 with 1 mg initial Ni co-catalyst before it completely deactivates.

The core-shell co-catalyst structures deactivated primarily due to a loss of metallic Ni from the core structure. During deactivation, the catalyst transformed either to structures consisting of NiO nanoblocks or hollow NiO shells. The phase transformations occurring during deactivation were associated with Ni diffusion processes that are driven by light illumination. However, the exact nature of this photocorrosion mechanism is not yet well understood.

Table 3.1: Heat treatment conditions for different co-catalysts.

Sample	(i)	(ii)	(iii)	(iv)	(v)
Name	Ni-NiO/ Ta_2O_5 OR*	Ni-NiO/ Ta_2O_5 O100	Ni-NiO/ Ta_2O_5 O150	Ni-NiO/ Ta_2O_5 O200	NiO/Ta_2O_5 O500
Reduction step	500 °C, 2h, flowing H_2/Ar				-
Oxidation step	-	100 °C, 1h, 200 Torr O_2	150 °C, 1h, 200 Torr O_2	200 °C, 1h, 200 Torr O_2	500 °C, 1h, flowing O_2

* OR means exposure to O_2 in air at room temperature.

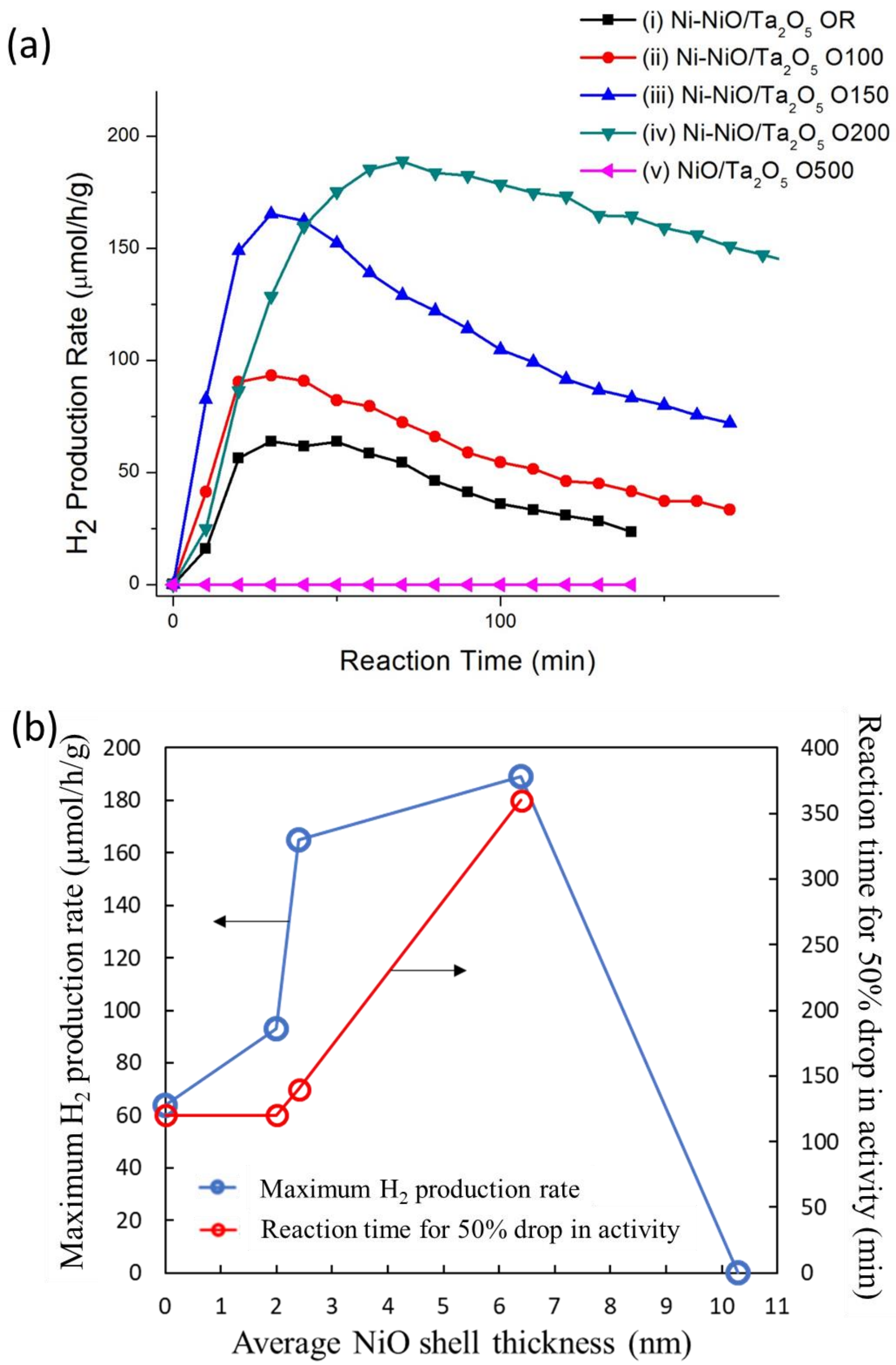

Figure 3.1: (a) H_2 production rate vs. reaction time of sample (i) to (v). (b) Maximum H_2 production rates of sample (i) to (v), and reaction time for 50% drop in activity (relative to maximum) of sample (i) to (iv) are plotted vs. the average NiO shell thickness of the corresponding sample.

Table 3.2: Activity and structure data of different co-catalysts.

Sample	(i)	(ii)	(iii)	(iv)	(v)
Name	Ni-NiO/Ta_2O_5 OR	Ni-NiO/Ta_2O_5 O100	Ni-NiO/Ta_2O_5 O150	Ni-NiO/Ta_2O_5 O200	NiO/Ta_2O_5 O500
Maximum H_2 Production rate (μmol/h/g)	64±3	93±3	165±12	189±3	0
Reaction time for 50% maximum activity (min)	120±10	120±10	140±10	360±10	-
Average particle size (nm)	10.6±4.8	11.4±4.0	12.9±4.2	19.0±9.1	10.3±2.3
Average oxide shell thickness (nm)	-	2.0±0.5	2.4±0.5	6.4±2.5	-
Average oxide shell thickness/particle size percentage	-	19±5%	19±4%	34±12%	-

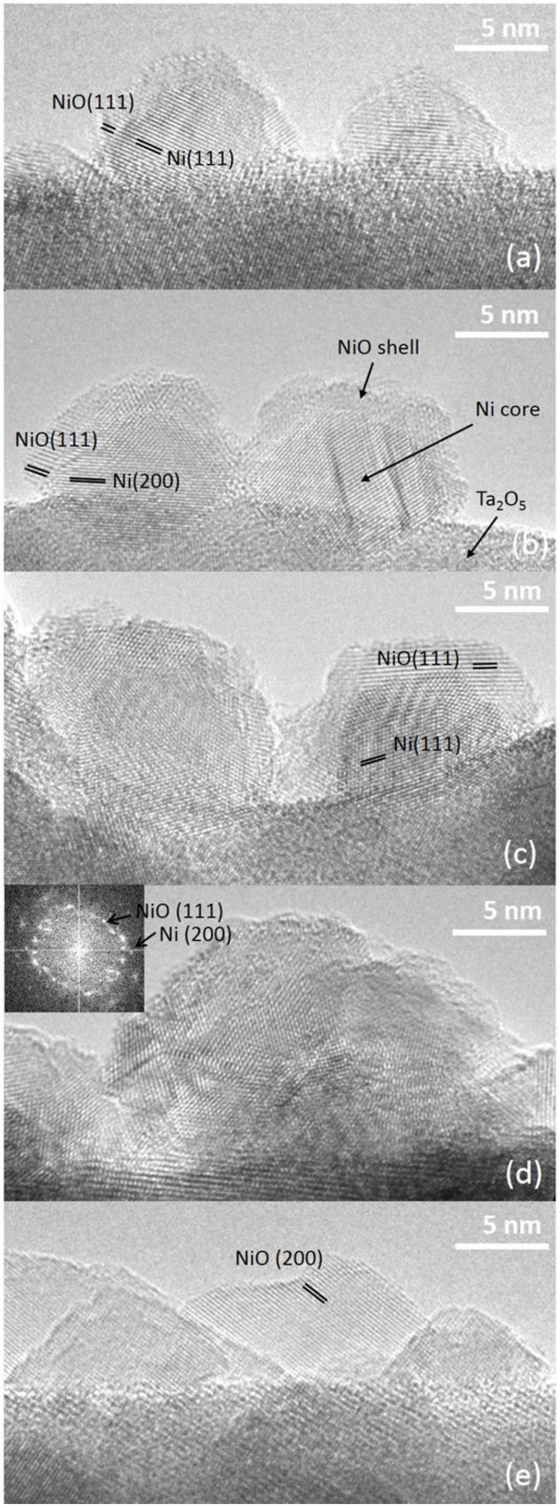

Figure 3.2: Image (a) - (e) show initial co-catalyst structures of sample (i) - (v) at the same magnification. (a): Co-catalyst of sample (i) was mainly Ni metal with a thin layer of native NiO; (b) and (c): Clear Ni core – NiO shell structures were observed for sample (ii) and (iii); (d) Most active sample (iv) showed complicated structure with presence of both Ni and NiO phases; (e) Pure NiO particles were observed on sample (v).

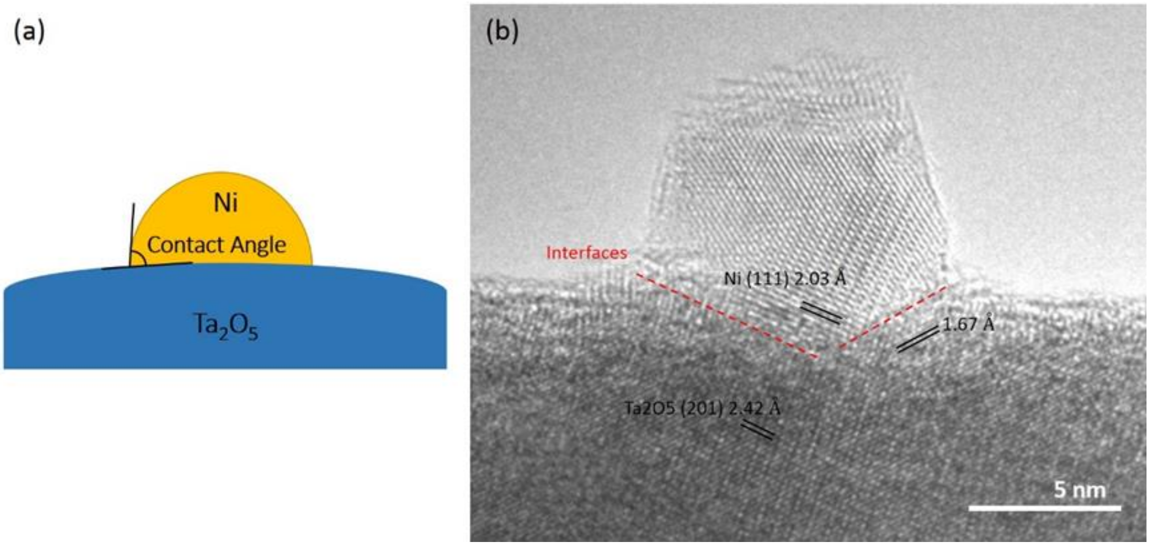

Figure 3.3: (a) Schematic graph showing the contact angle between Ni particle and Ta_2O_5 substrate. (b) Typical Ni metal/Ta_2O_5 semiconductor interface structure.

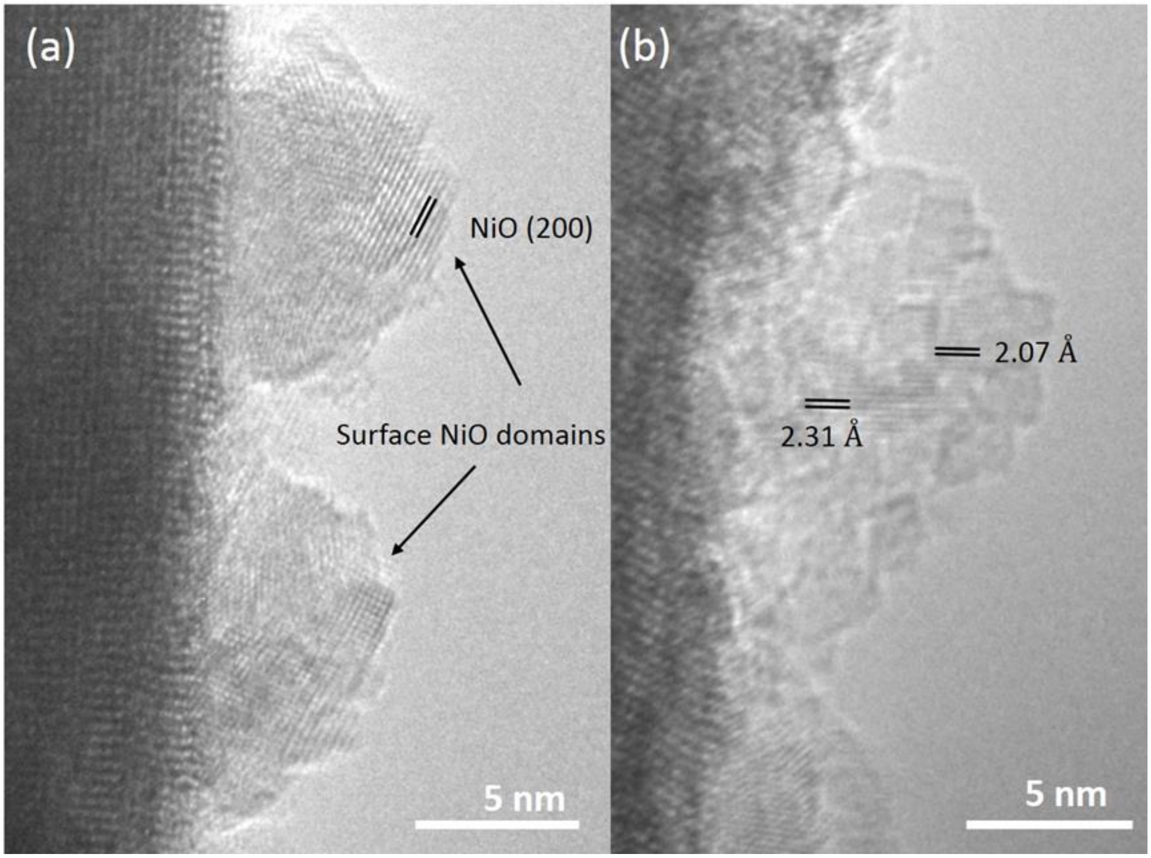

Figure 3.4: Sample (i) after water and UV exposure for 140 min showing morphology and phase changes: (a) Surface of the particles become more faceted, nanodomains and NiO lattice fringes emerge on the surface. (b) The whole particle turns to a cluster of NiO nanoblocks.

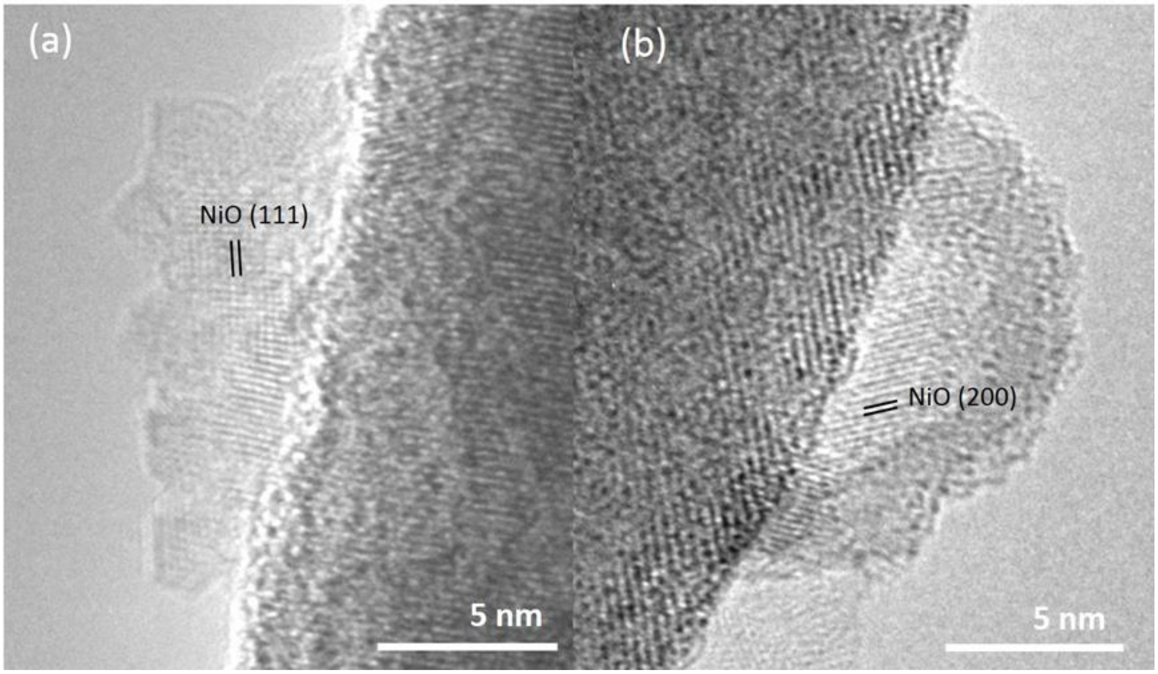

Figure 3.5: Sample (iv) after water and UV exposure for 16 h showing two types of structures of the used catalyst: (a) blocky NiO nanodomains. (b) void-shell structure.

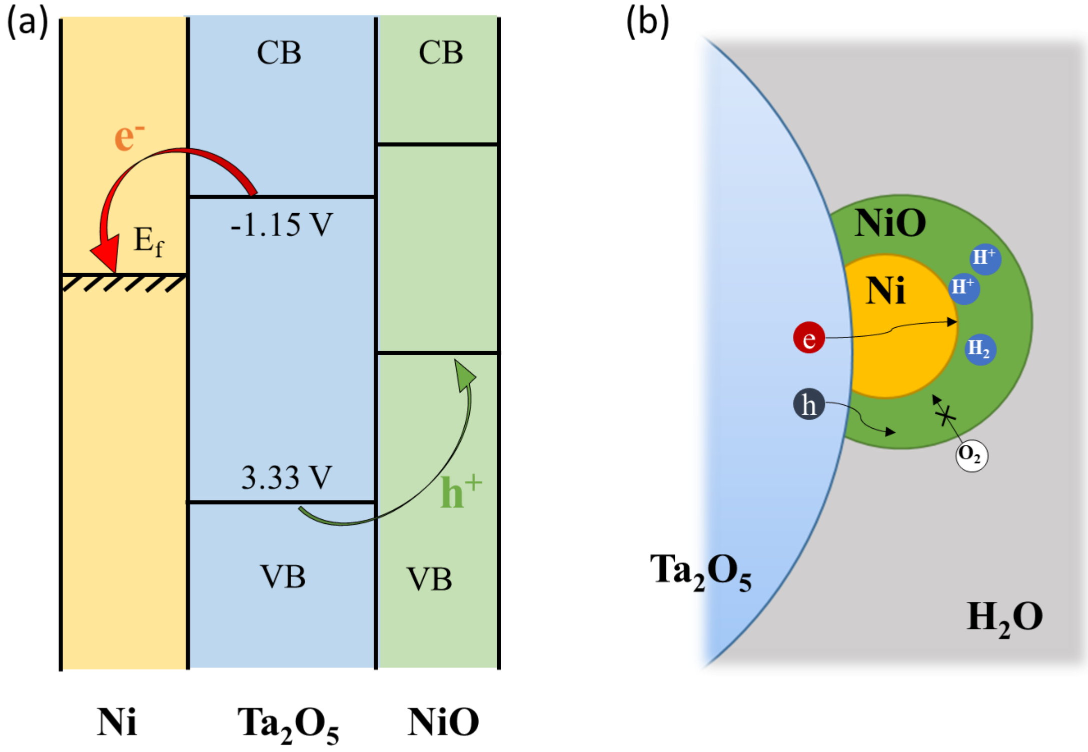

Figure 3.6: (a) Band alignments between Ta_2O_5, Ni and NiO. The band edge potentials relative to NHE (V) are labeled. (b) Schematic drawing of core-shell structure showing the NiO protective mechanism.

Table 3.3: The comparison between estimated H_2 production from photochemical reaction and the actual H_2 production detected by GC till 50% max reactivity.

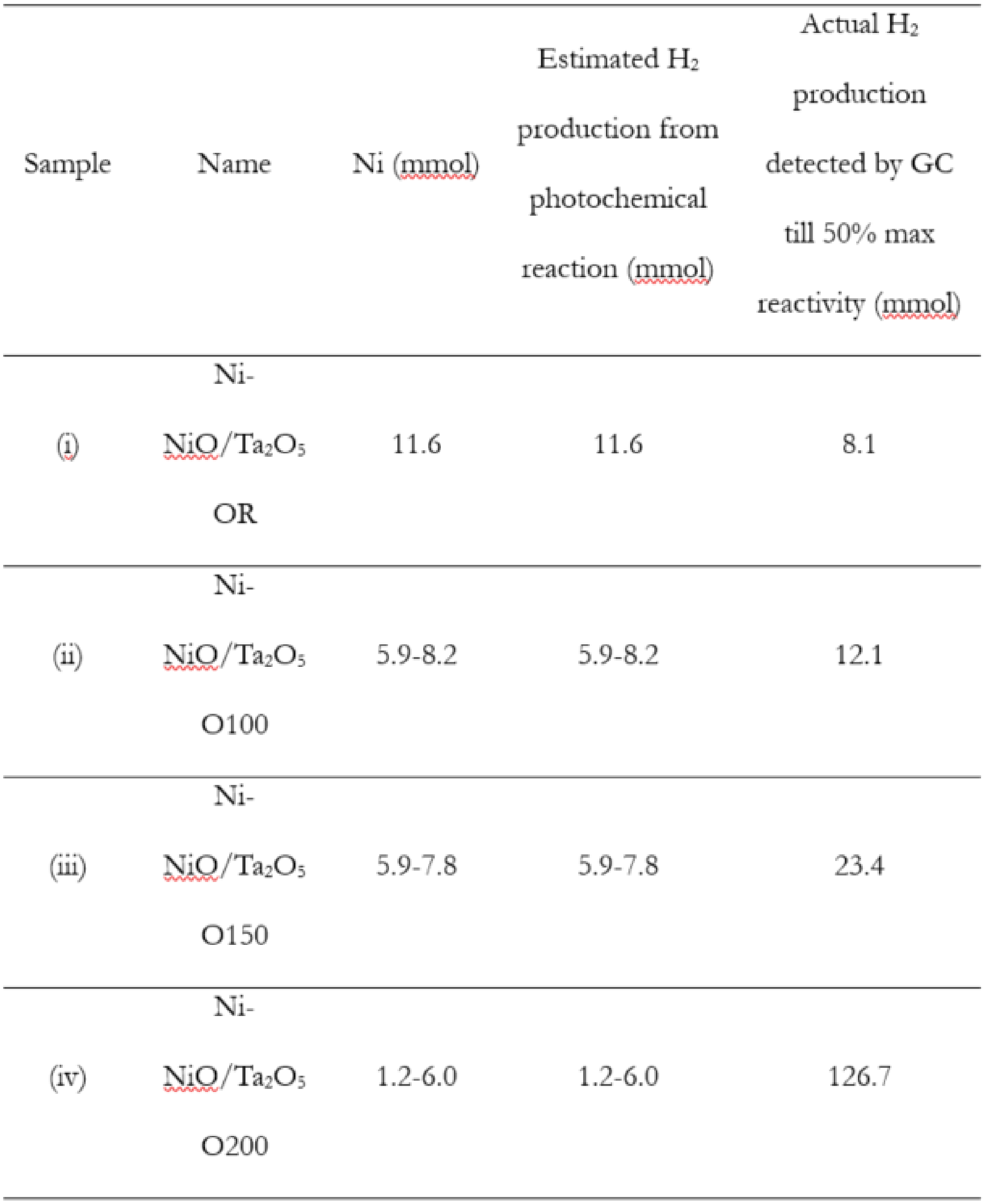

Sample	Name	Ni (mmol)	Estimated H_2 production from photochemical reaction (mmol)	Actual H_2 production detected by GC till 50% max reactivity (mmol)
(i)	Ni-NiO/Ta_2O_5 OR	11.6	11.6	8.1
(ii)	Ni-NiO/Ta_2O_5 O100	5.9-8.2	5.9-8.2	12.1
(iii)	Ni-NiO/Ta_2O_5 O150	5.9-7.8	5.9-7.8	23.4
(iv)	Ni-NiO/Ta_2O_5 O200	1.2-6.0	1.2-6.0	126.7

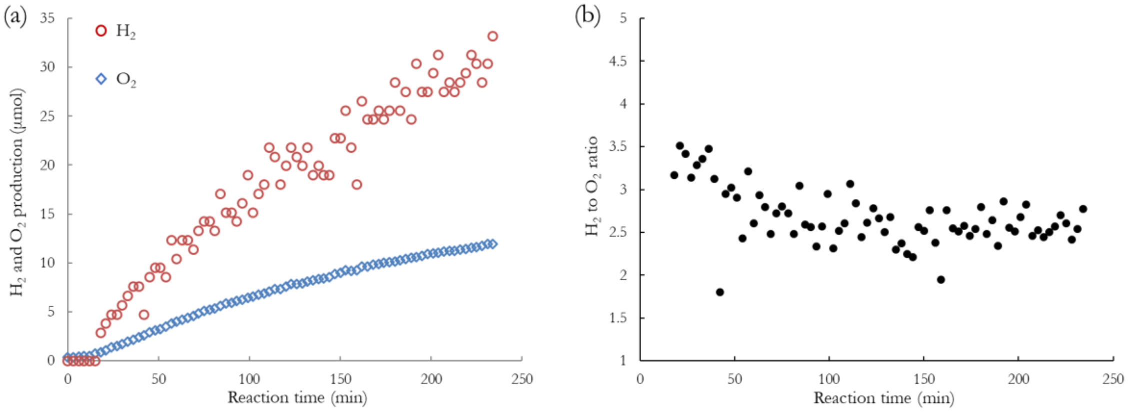

Figure 3.7: (a) H_2 and O_2 production over reaction time from 0.41 g of sample (iv). (b) The corresponding H_2:O_2 ratio over reaction time.

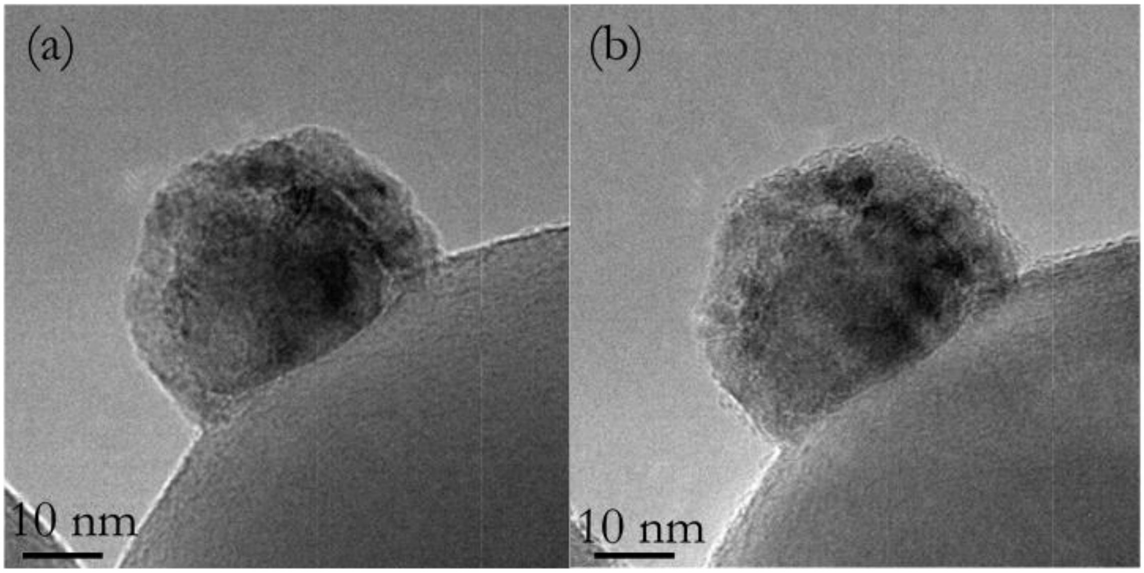

Figure 3.8: (a) An image of the initial Ni-NiO co-catalyst structure loaded on TiO_2, and (b) an image showing that no significant change occurred to the co-catalyst after it has been exposed to light and 18 Torr of water vapor for 16 h. Image courtesy of Liuxian Zhang.

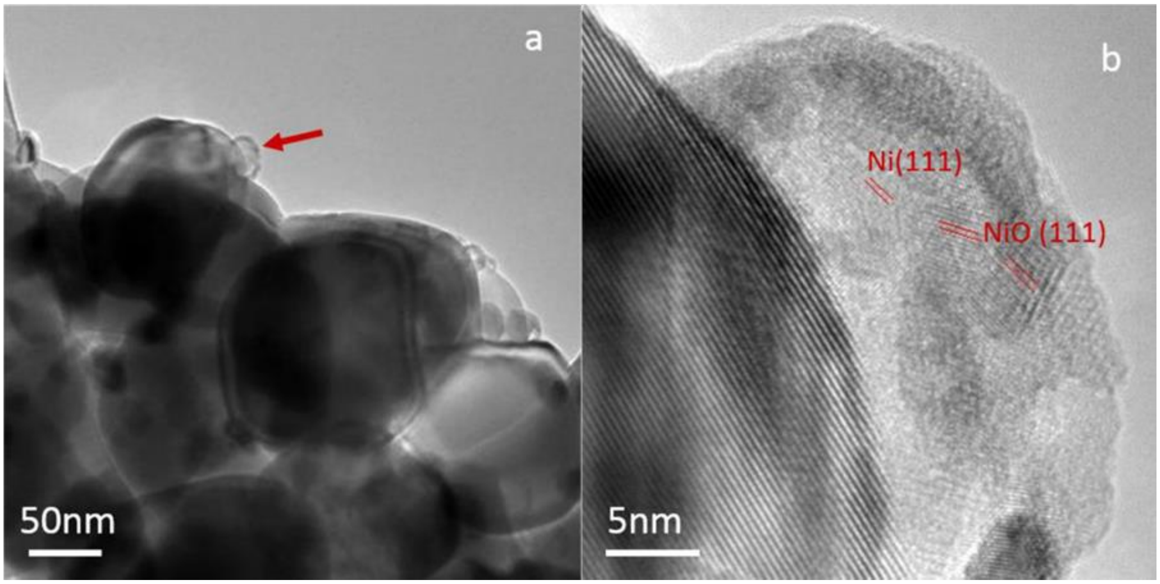

Figure 3.9: (a) An image of the Ni-NiO/TiO$_2$ catalyst after 15 min immersion in the etchant showing formation of void-shell structures. (b) A high resolution image of the co-catalyst particle pointed with the red arrow in (a).

4 Nanoscale Probing of Bandgap States on MgO Nanocubes Using Monochromated EELS

4.1 Motivation

As introduced in section 1.3.3, defects or adsorbed atoms on the surfaces of a semiconductor may result in extrinsic surface states which are electronic states within the bandgap. In more general definitions, electronic states can also be associated with surface and subsurface species which may form layers that are distinct from the underlying substrate phase. In particulate based catalysts, heterogeneity and defects generated during the preparation and processing of the materials, as well as exposure of the catalyst nanoparticles to gas or liquid reactants may give rise to different types of extrinsic surface states (Hardman et al. 1992; Diebold 2003).

The character of surface states influences charge transfer, and nanoparticle interactions with other particles or adsorbate species, thus controlling the selectivity and kinetics of the chemical reactions. For photocatalytic processes, electron-hole pairs migrate to the surface and may participate in catalytic reactions. Surface states play a vital role in photocatalytic reactions because they can serve as charge traps to increase the lifetime of a carrier and prevent recombination of electrons and holes (Linsebigler, Lu, and Yates 1995). Such traps may also lower the electrochemical potentials of the carriers and negatively impact catalytic properties. Characterizing the local nanoscale variation in oxide surface states is challenging but important for developing a fundamental understanding of catalyst functionality.

Experimentally, many techniques have been developed to measure electronic structures of materials' surfaces including ultraviolet photoemission spectroscopy (UPS) (Brause, Skordas, and Kempter 2000), reflection electron energy loss spectroscopy (REELS) (Z. L. Wang and

Cowley 1988; Henrich, Dresselhaus, and Zeiger 1980; Ibach and Mills 2013), metastable impact electron spectroscopy (MIES) (Brause, Skordas, and Kempter 2000; Harada, Masuda, and Ozaki 1997), scanning tunneling microscopy (STM) (Stroscio, Feenstra, and Fein 1986) and surface photovoltage spectroscopy (SPS) (Kronik and Shapira 2001). These techniques probe different aspects of the materials' electronic structure, usually requiring flat sample surfaces for better data quality, but, except for STM, do not have the ability of imaging sample microstructure simultaneously. Here a novel form of monochromated EELS is employ (Ondrej L. Krivanek et al. 2014), which is introduced in section 2.4, giving an energy resolution of 15 meV or better as well as a substantially smaller ZLP tail compared to regular cold FEG or Schottky FEG instruments, to detect and characterize electronic states on or near the surfaces of oxide nanoparticles. The energy-loss capability is coupled to an aberration-corrected STEM, allowing the ultra-high energy resolution spectroscopy to be performed with a sub-nanometer electron probe. With this configuration, atomic level electron imaging can provide high spatial resolution information on surface morphology while EELS can provide the local electronic properties of the near-surface region.

Most energy-loss spectra are recorded by transmitting a fast electron beam through the sample (**Figure 4.1a**). Recording energy-loss spectra with a sub-nanometer electron probe can permit electronic structure to be probed with atomic resolution (Muller et al. 2008; Ramasse et al. 2013). However, the high incident electron energy and the relatively large electron dose associated with this high spatial resolution analysis may damage the structure under observation. Radiation damage effects are particularly pronounced on surfaces because the open structure makes mass loss more facile (Raymond F. Egerton, Wang, and Crozier 2006). When the electron beam passes through the sample, two types of radiation damage mechanisms are possible: knock-on (direct displacement of the nucleus by the fast electron) and radiolysis (ionization by the fast electron), which are described in detail elsewhere (R.F. Egerton 2013, 2012). An alternative approach to spectral acquisition is the so-called "aloof beam" mode where the electron probe is parked some distance away from the surface of the sample (Crozier 2017; Batson 1982; Howie and Milne 1985; García de Abajo 2010) (**Figure 4.1b**). The delocalized component of the electron-solid interaction allows the electronic states at or near the surface to be excited even when the probe is positioned outside the sample. In aloof mode, the knock-on damage process is essentially turned off and radiolytic damage can be greatly reduced depending on the distance between the specimen surface and the electron beam. This opens up the possibility for nanometer resolution detection of surface states because radiation damage is significantly suppressed and the EELS signal is strong only when the probe is within a few nanometers of the surface.

To develop the aloof beam EELS approach, an initial test material is needed and is selected to be MgO nanocubes, because of their well-defined morphology and wide bandgap. Using low-energy REELS, Henrich et al. have observed an intrinsic surface transition signal at 6.2 eV and a 2.3 eV peak possibly associated with surface defects in MgO (Henrich, Dresselhaus, and Zeiger 1980). In this chapter, extrinsic surface states associated with exposing the (100) facets of MgO nanocubes to water vapor are investigated. Both experimental and theoretical work indicates that MgO readily absorbs water in ambient atmosphere and water molecule dissociation and hydroxyl species formation often occur on surface steps (Langel and Parrinello 1994). This hydroxylation process generates a source of extrinsic surface states on MgO nanocubes, leading to generation of spectral features in the bandgap region. Two different methods, a dielectric function and a DOS approach, are developed here to interpret the surface state induced spectral features. The relative simple MgO system is ideal for exploring the advantages and disadvantages of both approaches. It is hoped that the aloof beam EELS technique and the interpretation methods developed in this work can be applied to other photocatalyst materials to probe local surface states.

4.2 Materials and Methods

Materials: MgO is obtained by collecting the product particles while combusting Mg ribbon in air and then exposed to water vapor. A portion of the MgO particles were then dispersed in DI water and heated to 70 °C for about 10 h to produce a $Mg_x(OH)_y$ reference compound.

An aberration-corrected NION UltraSTEM 100 microscope coupled with a monochromator and a Gatan Enfinium spectrometer was employed to acquire all the spectra. The microscope was operated at 60 kV with an energy dispersion of 5 meV per channel. FWHM of the ZLP was better than 25 meV. Convergence angle α was 30 mrad, and detector collection angle β was 15 mrad with 1 mm EELS entrance aperture. Gatan Digital Micrograph software was used to process the data. Spot spectra were acquired where the beam was positioned either in bulk MgO or 4 nm away from the surface and the acquisition time was 50 s to maximize the signal-to-noise ratio.

4.3 Results and Discussion

In the most common form of EELS acquisition, the electron beam passes through the TEM specimen (**Figure 4.1a**) whereas in the aloof beam configuration, the beam is positioned some distance outside the surface of the sample as shown in **Figure 4.1b**. The distance of the beam from the surface is typically called the impact parameter b. Although the electron beam does not enter the sample in this case, it can still excite the electrons in the material via the Coulomb field interaction. In STEM, the electron beam is converged to a small spot using convergent illumination. Considering the specimen thickness t and an electron beam with a convergence angle α, the aloof beam geometry will apply only when the impact parameter $\mathrm{b} \geq \frac{t}{2} \times \tan(\alpha)$. This condition must be satisfied in the STEM to ensure that no electrons enter any part of the sample. For the experimental data presented in this chapter, a 30 mrad convergence angle was used and sample thicknesses were usually smaller than 100 nm so, in general, the aloof condition applied when the beam was at least 1.5 nm away from the surface. Also, a relatively small impact parameter was preferred to ensure that sufficient signal-to-noise ratios can be achieved. Therefore, a 4-nm impact parameter was often used when aloof beam EELS was acquired from MgO.

Transmission and aloof spectra from an MgO nanoparticle are shown in **Figure 4.2**. A HAADF image shows the nanocubes are terminated with (100) surfaces which are well known to be the low-energy surface facet (Gibson, Haydock, and LaFemina 1992). The beam was positioned on top of a nanocube for the transmission spectrum, and 4 nm away from the nanocube for the aloof spectrum. Both raw spectra (**Figure 4.2a**) show an abrupt increase in intensity at 7.3 eV corresponding to the bandgap onset and a bandgap of 7.3 eV is in agreement with literature value (Roessler and Walker 1967). The tail on the ZLP was best fitted by a first order lognormal-polynomial background model available in the Gatan Digital Micrograph software, and the background subtracted spectra are compared in **Figure 4.2b**. For a 60 kV electron, significant Cherenkov will only occur when the refractive index of the material is larger than 2.24 (R. Egerton 2011) and the refractive index of MgO is 1.7. Thus, in this case significant energy-losses due to Cherenkov radiation is not expected. Interestingly, the aloof spectrum shows an additional continuous intensity rise starting from 5.6 eV leading to a plateau which merges into the conduction band onset at 7.3 eV. There is some evidence for a similar effect in the transmission spectrum but of much smaller relative intensity. The high intensity of this plateau in the aloof beam spectrum suggests that this spectral feature is associated with surface state transitions. The weaker feature observed in the transmission spectrum is associated with the beam passing through the top and bottom surfaces of the cube.

4.3.1 Dielectric Approach

To investigate the origin of this spectral feature, dielectric theory is employed to simulate the energy-loss spectra for transmission and aloof beam geometries. The simulations employed MgO dielectric properties derived from reflectance measurements (Roessler and Walker 1967) and slightly adjusted to fit with the experimental bandgap onset (displayed in section 8.3). Dielectric based theories have been developed to simulate transmission and aloof beam spectra (Batson 1983; Howie and Milne 1985; García de Abajo 2010). Since 60 kV electrons are used for the current experiments, relativistic effects can be ignored. In the non-relativistic limit, treating the experimental data as single scattering distribution, the transmission spectra, S(E), can be simulated using the energy loss function Im(-1/ε), where ε is the energy dependent complex dielectric function (Raether 1965; R. Egerton 2011). For the bandgap region and sample thickness of interest here, plural scattering effects are small and are neglected.

For a bulk terminated sample illustrated in **Figure 4.3a**, the aloof spectrum for an electron travelling parallel to surface at a distance of b (impact parameter) can be written as (Howie and Milne 1985)

$$\mathrm{I(E)} \propto \mathrm{Im}(-\frac{1}{\varepsilon+1})\times K_o(\frac{2\omega b}{v}) \quad 4.1$$

where I(E) is the intensity in the EELS spectrum, K_o is the zero-order modified Bessel function, ω is the frequency corresponding to each energy loss, v is the velocity of the fast electron in the beam. One limitation of the model is that it assumes the beam is parallel to the sample surface while in reality the STEM probe is a convergent beam. However, it has been demonstrated this approximation is reasonable and does not significantly affect the shape of the EELS spectra (Moreau et al. 1997).

The simulated transmission and aloof spectra of bulk MgO were calculated and compared with experimental transmission data in **Figure 4.4**. Each spectrum was normalized so that the signal intensity at 7.9 eV was set to unity. The dielectric approach produces a good match in the overall shape between the simulated spectra and the experimental data reproducing the two peaks at about 7.9 and 11.8 eV. No pre-bandgap intensity was seen in the simulated aloof spectrum from pure MgO suggesting the additional intensity at 5.6 eV is associated with extrinsic states caused by the presence of a surface phase.

The most likely origin of the surface phase is the presence of hydroxyl species leading to a possible thin layer of magnesium hydrate. To simulate the influence of a surface phase, a more sophisticated dielectric model is required which explicitly includes a thin film on a bulk substrate. Such a model is illustrated in **Figure 4.3b** in which the surface phase is represented by a thin layer of thickness 2a with dielectric function ε_1 on a substrate material with dielectric function ε. In the non-relativistic limit, the aloof beam spectrum, I(E), for an electron travelling parallel to the surface with impact parameter b is given by (Howie and Milne 1985):

$$I(E) \propto \{F(\varepsilon, \varepsilon_1, K, a)\times \exp(-2K\times b)\} \quad 4.2$$

$$K^2 = q^2 + (\frac{\omega}{v})^2$$

$$F(\varepsilon, \varepsilon_1, K, a) = Im\{[(\varepsilon_1 + \varepsilon)(\varepsilon_1 - 1)\exp(2Ka) - (\varepsilon_1 - \varepsilon)(\varepsilon_1 + 1)\exp(-2Ka)] \times [(\varepsilon_1 + \varepsilon)(\varepsilon_1 + 1)\exp(2Ka) - (\varepsilon_1 - \varepsilon)(\varepsilon_1 - 1)\exp(-2Ka)]^{-1}\}$$

where q is the momentum transfer parallel to the plane of the interface. The geometry of this so-called infinite slab model is an approximation because in reality, the top and bottom of the substrate should also be coated with ε_1 surface dielectric layers. But their contribution to the aloof EELS spectrum is small as they are further away from the beam.

To explore the hydrate hypothesis, it is necessary to know the dielectric function for magnesium hydrate. No accurate experimental dielectric data of magnesium hydrate was found from the literature so an estimate of the dielectric function was made from experimental energy-loss spectra from the $Mg_x(OH)_y$ reference compound. The $Mg_x(OH)_y$ had a non-uniform morphology (**Figure 4.5a inset**) and was extremely beam sensitive. This made it impossible to apply standard Kramer-Kronig methods to determine the dielectric function (J. Zhu et al. 2014). Experimental EELS spectra of $Mg_x(OH)_y$ were acquired in aloof mode to minimize radiation damage (**Figure 4.5a**), and a bandgap onset at about 5.3 eV was detected, which was very close to the 5.6 eV starting point of the plateau features observed within the bandgap of the MgO. As mentioned previously, EELS intensity generated from a material is closely related to its bulk dielectric function, especially the imaginary part of the function (R. Egerton 2011). In fact, examination of the MgO dielectric function showed that the experimental EELS signal generated from MgO resembled the imaginary part of the bulk MgO dielectric function despite a small energy shift. It was thus assumed that the aloof beam EELS intensity generated from the $Mg_x(OH)_y$ reference was approximately proportional to the imaginary part of the $Mg_x(OH)_y$ dielectric function, which stayed at zero below the bandgap onset and then gradually increased following the spectral intensity trend. Since no peak is present within this energy range, the real part of the $Mg_x(OH)_y$ dielectric function was assumed to be constant before the bandgap onset and then slowly increasing. In addition, the values of the dielectric data were set so that the refractive index matched the value that has been reported (Al-Gaashani et al. 2012). Then Eq. 4.1 was used to simulate the aloof beam EELS of $Mg_x(OH)_y$ using the hypothesized imaginary and real parts of the dielectric function, and the simulated spectrum was compared to the experimental spectrum. Several iterations were performed by adjusting the hypothesized values until a reasonable match between the simulation and experiment was reached as shown in **Figure 4.5a**.

The final real and imaginary values of $Mg_x(OH)_y$ which produced the best simulated spectrum were used to represent the dielectric characters of the surface layer (ε_1) on top of the MgO bulk (ε) in the model illustrated in **Figure 4.3b**. To perform the simulation based on Eq. 4.2, the impact parameter b was fixed at 4 nm, while the surface layer thickness 2a was changed to match the experiment. A thickness of less than 2 nm for the surface phase gave the best fit to the experiment data as shown in **Figure 4.5b**.

The dielectric function derived from bulk $Mg_x(OH)_y$ sample had a shape that matched the experimental spectrum but there is uncertainty in the absolute value introducing considerable uncertainty in the thickness of the surface layer. Moreover, while the dielectric approach provides information on excitation energies of the surface it does not directly provide information on the energy of the surface states with respect to the MgO band edges. An alternative approach is to simulate the energy-loss spectra using an approximation that starts from knowledge of the DOS. With this approach, the spectral intensity within the bandgap region arises from specific states that are present within the bandgap. The energy, width and number of the states are adjusted to match the experimental observations.

4.3.2 DOS Approach

The DOS approach works in part because, for an insulator, the aloof beam spectrum can be approximately decomposed into bulk and surface contributions. For MgO, examination of the real and imaginary parts of the dielectric function shows that $\mathrm{Im}\left(-\frac{1}{\varepsilon+1}\right) \sim \mathrm{Im}(\frac{-1}{\varepsilon})$. Thus, the bulk contribution to the aloof beam spectrum closely resembles the transmission spectrum with the signal arising from the higher energy-loss attenuated because they are more strongly localized. The localization attenuation is contained in the Bessel function term of Eq. 4.1. Thus, the energy-loss intensity can be approximately re-written in the form:

$$I(E) \propto Im(-\frac{1}{\varepsilon}) \times K_o(\frac{2\omega b}{v}) \qquad 4.3$$

Figure 4.4 shows that a simulated spectrum from Eq. 4.3 closely matches the spectrum determined from the more rigorous Eq. 4.1. Thus the bulk contribution to the aloof beam spectrum strongly resembles the transmission spectrum.

The transmission single scattering distribution, S(E) can also be interpreted in terms of a convolution between the valence and conduction band DOS through the equation (R. Egerton 2011):

$$S(E) \propto \rho_{VB}(E) * \rho_{CB}(E) \qquad 4.4$$

where the right hand side, the so-called joint density of states (JDOS), is the convolution of the initial (occupied) projected density of states (PDOS) in the VB, $\rho_{VB}(E)$, with the final (empty) PDOS in the CB, $\rho_{CB}(E)$. The convolution is usually performed following the dipole selection rules which dominate the features in the energy-loss spectrum. The JDOS approach does not take many body effects (like excitons) into account but can often provide a guide to identify the origin of electronic structure features in the spectrum. This simple approach has been successfully employed to locate the position and width of bandgap states with respect to the CB edge in doped ceria (Bowman et al. 2016). The similarity between the aloof and transmission spectra for MgO suggests that this approach may be useful for the interpretation of surface states. In this interpretation, the bulk contribution to the aloof beam spectrum is assumed to arise from the bulk DOS and the surface contribution comes from states located within the bandgap.

The DOS for MgO has been calculated by various researchers (Bredow and Gerson 2000; King et al. 2009; Malashevich, Altman, and Ismail-Beigi 2014) and a first-principles calculation by Xu et al (Y.-N. Xu and Ching 1991) was employed here, and slightly modified to better fit the experimental data (**Figure 4.6a**). **Figure 4.6b** shows the derived JDOS obtained by convolving the PDOS following the dipole selection rules which approximately apply to EELS. Because the VB is mainly O 2p and the CB is mainly Mg 3s, the O 2p → Mg 3s transition predominates and determines the shape of the JDOS. Compared to the experimental data, the peak at 7.9 eV in the experiment is missing. Sobolev and others have indicated that this peak is associated with exciton states in MgO which could only be observed when the material is in the excited state (Sobolev 2004; Roessler and Walker 1967; Y.-N. Xu and Ching 1991). This exciton phenomenon is not included in the one electron ground state calculation of the DOS data and will introduce some uncertainty in the number of surface states present.

The bulk contribution to the aloof beam spectra can be simulated by using Eq. 4.4. The surface contribution will then arise by inserting additional states into the bandgap region. It should be emphasized that the inserted bandgap states are only associated with the surface species on the MgO nanocube because experimentally, the plateau features were observed in the aloof beam geometry where signals were surface sensitive. It is informative to consider the effect of introducing a bandgap state on the form of the energy-loss spectrum. A fully occupied bandgap state will give transitions into the empty CB and the convolution shows that this will yield a spectral intensity distribution in the bandgap region that looks like the CB DOS. A fully unoccupied state will be associated with transitions from the VB so it will give rise to an intensity distribution in the bandgap that resembles the VB DOS. Thus, a sharp bandgap state will essentially give a spectrum in the bandgap that looks either like the bulk conduction or bulk valence band DOS.

The theoretical data in **Figure 4.6** shows that the DOS for both the valence and conduction band varies rapidly within the 2-3 eV of the band edges. However, the experimental data of **Figure 4.2b** shows a more slowly varying smooth increase suggesting that the bandgap states must be broad. The simulated spectrum with a broad filled bandgap state is shown in **Figure 4.7**. As expected, the exciton feature at 7.9 eV was not reproduced, but, for the intensity below the bandgap, the best agreement with the experiment was obtained with a Gaussian shaped filled state centered at 1.1 eV above the VB with a FWHM of 0.7 eV. Moreover, simulating the plateau feature with a broad empty bandgap state has also been attempted and the best result that can be achieved in this scenario is displayed in **Figure 4.8**. It can be seen from **Figure 4.8b** that the simulated spectral feature before the MgO bandgap onset did not match the continuously increasing intensity in the experimental data very well, due to the shape of the VB DOS. Therefore, the most likely bandgap state associated with the surface species on the MgO nanocube is a filled broad state about 1 eV above the VB of bulk MgO.

Other comments

It should be mentioned that vibrational EELS has also been employed to probe the surface species from the same MgO nanocube sample in a separate work (Crozier, Aoki, and Liu 2016), and the obtained aloof beam vibrational spectrum reveals the presence of a broad peak centered at 430 meV with a FWHM of ~60 meV (**Figure 4.9**). This is consistent with the OH vibrational fingerprint detected from a reference hydrate ($Ni(NO_3)•6H_2O$) using either vibrational EELS or infrared spectroscopy, which lies at 430 meV with a FWHM of ~80 meV. Based on the vibrational results, the presence of OH species on the surface of the MgO nanocube is unambiguously confirmed, validating the results obtained based on the dielectric approach.

Furthermore, the vibrational peaks detected from the nanocube surface and the hydrate material are relatively wider than the OH signal detected from a hydroxide reference, $Ca(OH)_2$, which shows a FWHM of ~24 meV. This may imply that the OH bonds on the nanocube surface are not as well-defined as those exist in the hydroxide material, possessing a variety of different stretch modes. This is consistent with the DOS based and dielectric based interpretations discussed above. Narrow energy states are associated with isolated point defects such as oxygen vacancies or impurities/dopants and as the defect densities increases, these states become broader. Finding that a relatively broad defect state fits the experimental data using the DOS based simulations qualitatively agrees with the dielectric interpretation of a continuous layer of $Mg_x(OH)_y$ on the surface.

4.4 Summary

Ultra-high energy resolution EELS in a STEM is used to investigate the electronic states associated with the (100) surfaces of MgO oxide nanocubes after exposure to water vapor. By employing the so-called aloof beam mode, radiation damage to oxide surfaces can be suppressed while still allowing nanometer spatial resolution to be maintained. The surface states introduce plateau shaped features before the bandgap onset in the EEL spectrum which can be interpreted within either a dielectric function or DOS framework.

The experimental spectrum from a 60 nm MgO cube agrees well with a simulated spectrum based on the dielectric theory, where the spectral features before the bandgap onset is found to be associated with a surface hydrate layer less than 2 nm thick. On the other hand, the DOS approach cannot simulate the exciton peak observed in the experiment as it does not include many body effect. However, the purpose of conducting DOS based calculations is to find out the energy level and width of the surface electronic states in the bandgap of the material. A broad occupied state located 1.1 eV above the VB of MgO substrate is found to be associated with the hydrate overlayer.

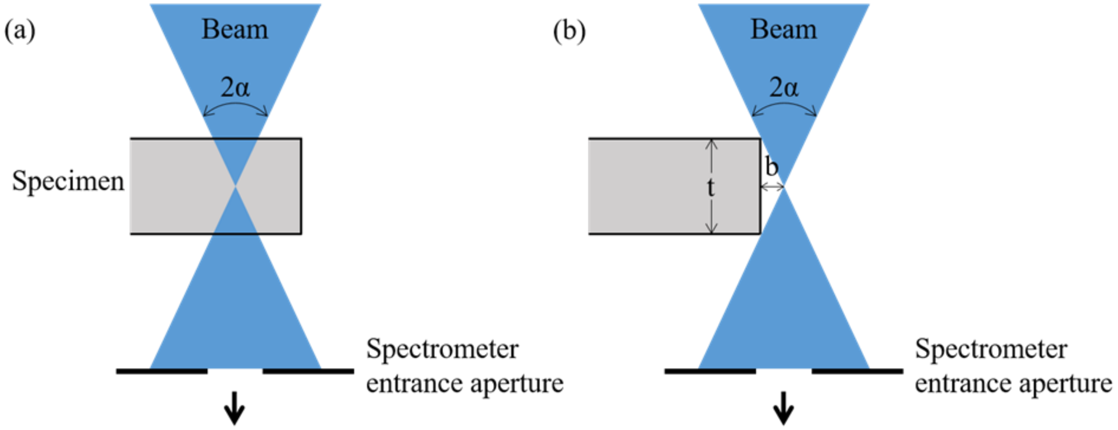

Figure 4.1: Schematic diagram showing the geometry of (a) transmission and (b) aloof convergent beam configuration.

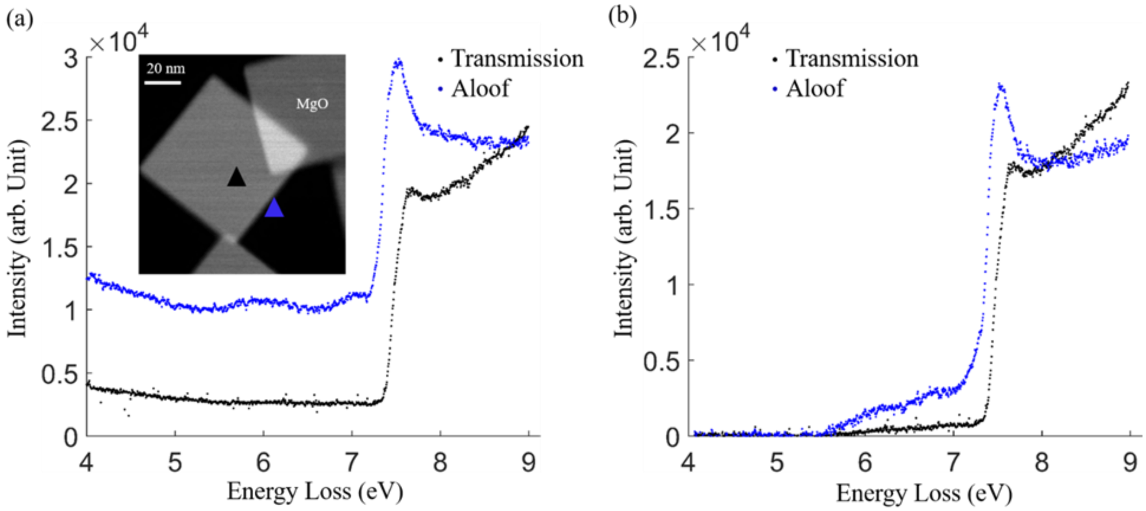

Figure 4.2: (a) HAADF image showing MgO nanocubes and beam positions for transmission (black triangle) and aloof (blue triangle) configurations. Raw spectra from the two positions are plotted. (b) Background removed transmission and aloof spectra.

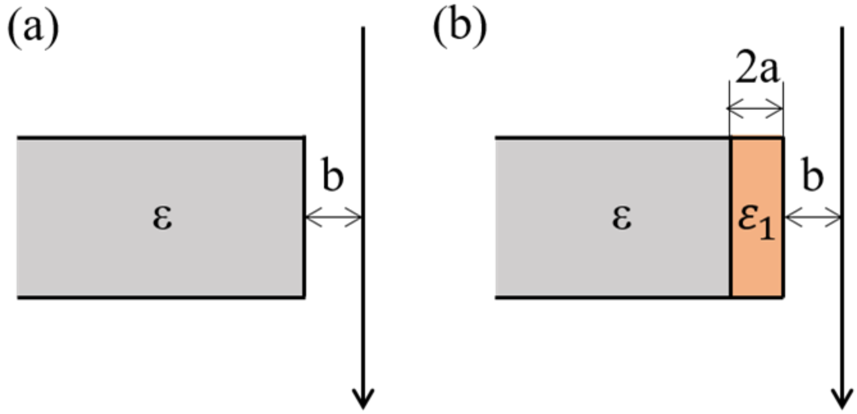

Figure 4.3: Schematic drawing of (a) a dielectric bulk terminated structure with a parallel beam outside the sample, at a distance b. (b) a dielectric model of substrate (ε) and surface (ε_1) structure with a parallel beam at a distance b. The surface layer thickness is 2a.

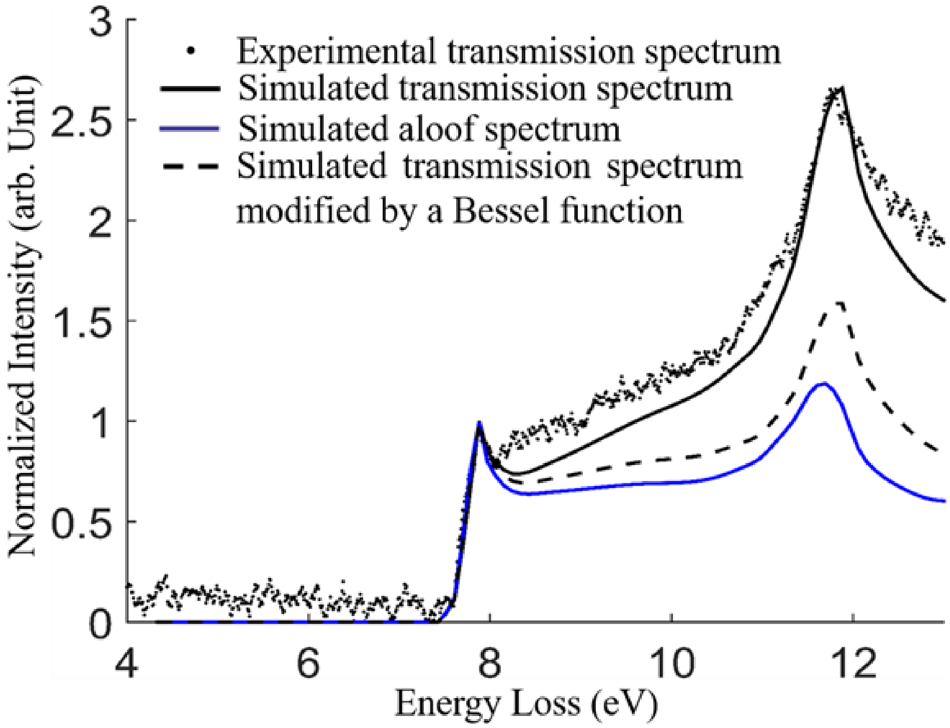

Figure 4.4: Experimental (dotted) and simulated (solid black) MgO bandgap onset in transmission mode. Simulated aloof mode spectrum (blue) using dielectric model, and simulated transmission multiplied by a Bessel function (dashed black) are also shown. All are normalized to set the intensity at 7.9 eV to be 1 unit.

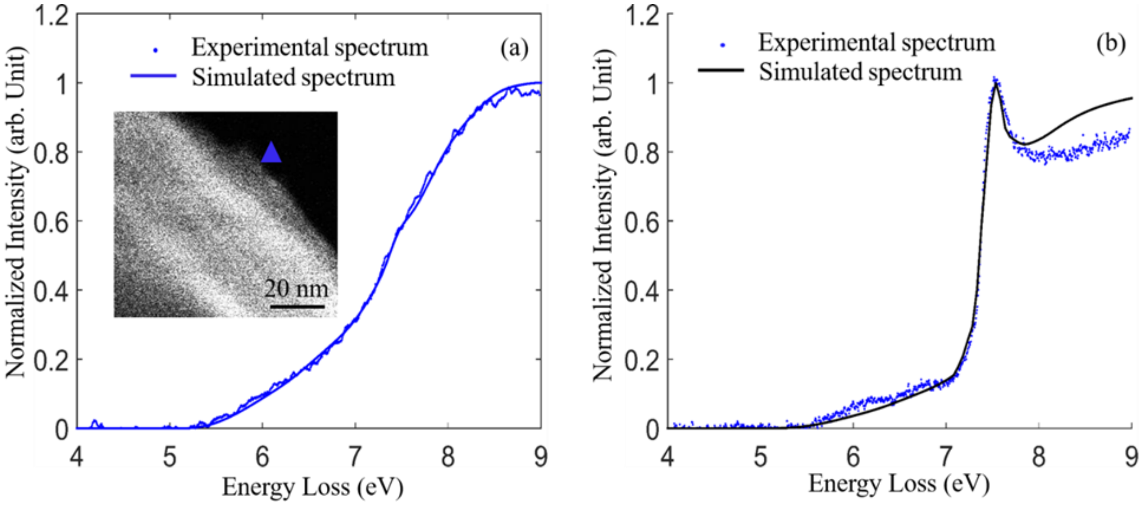

Figure 4.5: (a) Experimental and simulated bandgap onsets of Mg$_x$(OH)$_y$ when the beam is 3 nm away from the sample surface. (b) Simulated aloof energy-loss spectrum for a 1.7 nm overlayer of Mg$_x$(OH)$_y$ on MgO compared with the experimental aloof spectrum.

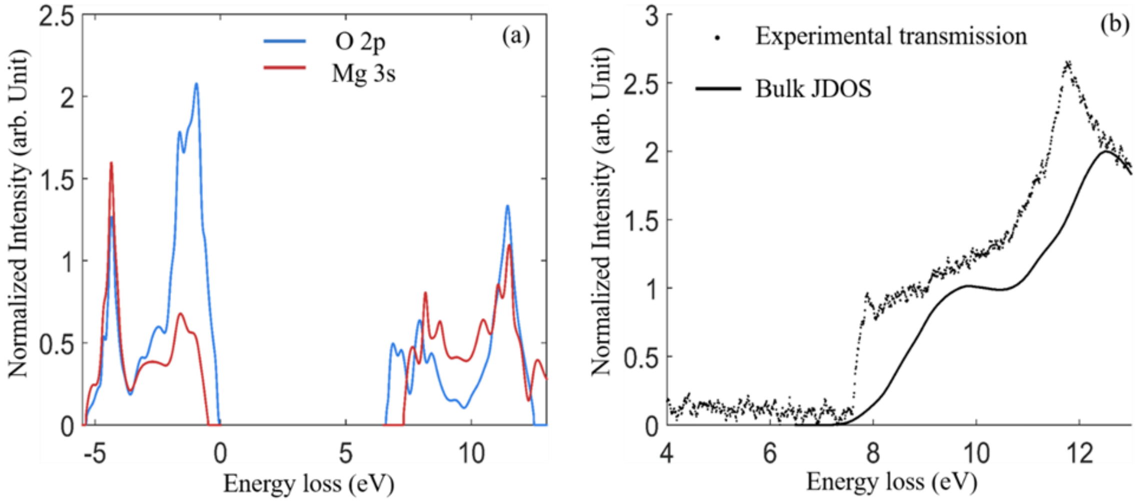

Figure 4.6: (a) Modified PDOS of MgO, with top of VB set to 0 eV. (b) Experimental bulk spectrum and calculated bulk JDOS.

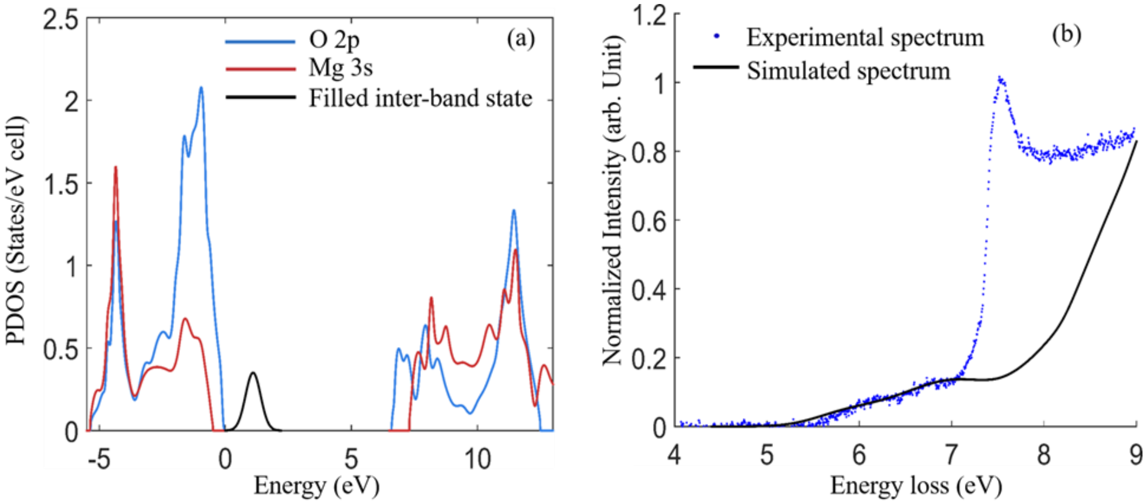

Figure 4.7: (a) PDOS of MgO with a Gaussian shaped filled state centered at 1.1 eV above the VB with FWHM of 0.7 eV. (b) Black curve is the simulated spectrum from the DOS in a), compared with the experimental aloof spectrum (dotted blue).

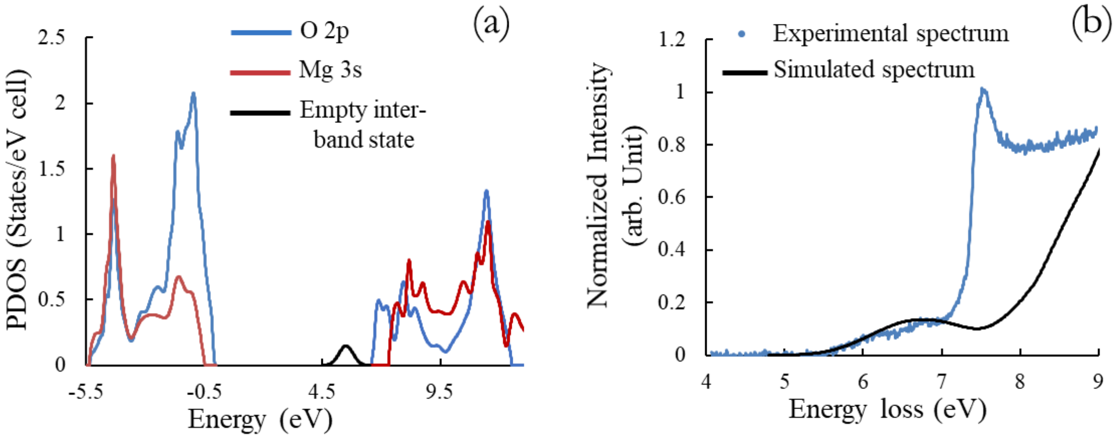

Figure 4.8: (a) PDOS of MgO with a Gaussian shaped empty state centered at 5.5 eV above the VB with FWHM of 0.7 eV. (b) Black curve is the simulated spectrum from the DOS in a), compared with the experimental aloof spectrum (dotted blue).

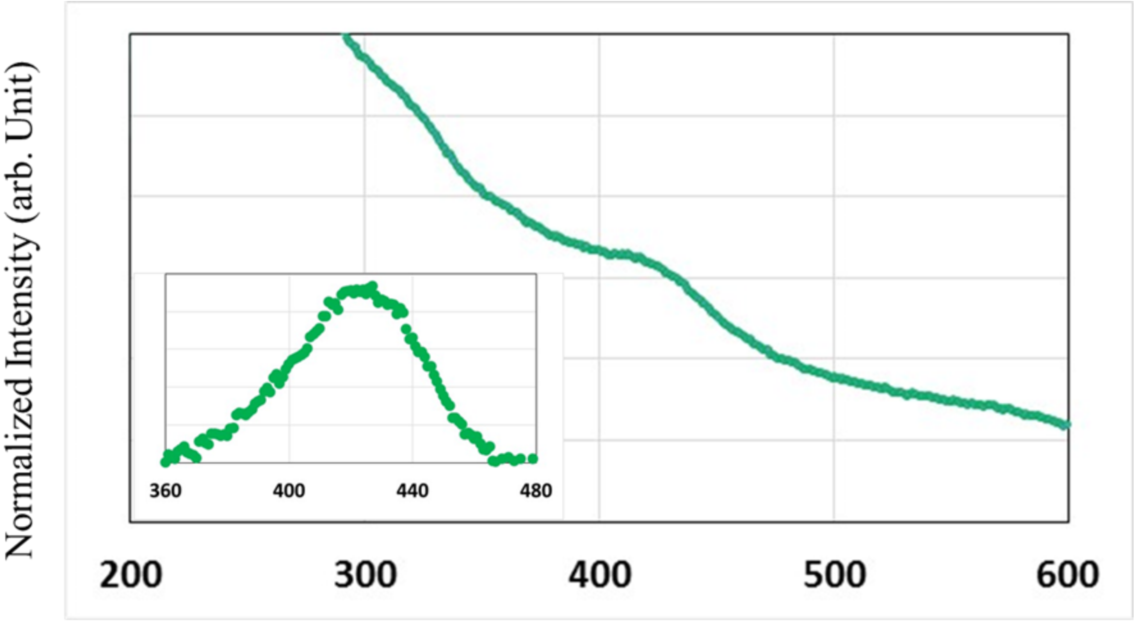

Energy loss (meV)

Figure 4.9: Aloof beam vibrational EELS showing OH stretch at 430 meV associated with surface OH layer. The inset is the vibrational peak after background subtraction.

5 Cavity Modes of Oxide Nanoparticles Probed by Monochromated EELS

5.1 Motivation

In Chapter 4, an aloof beam EELS technique for characterizing surface electronic structure has been developed on the model system of MgO nanocube, where surface states associated with hydrate species are detected and interpreted. The same technique was applied to other oxide nanoparticles of importance in photocatalysis, with the aim of understanding how nanoparticle composition, shape, and size affect surface electronic structure and light-particle interaction such as excitation of geometry-induced optical-frequency resonant modes, which are critical to functionality. The focus of this chapter is on investigating the behavior of the latter geometric resonant modes of catalytically relevant oxide nanoparticles using monochromated STEM EELS.

STEM EELS provides a unique approach for locally probing a materials' optical properties with nanometer spatial resolution, since the probing or so-called fast electrons in a STEM can be viewed as an evanescent source of supercontinuum light. Said differently, an electron in uniform relativistic motion generates predominantly transverse electromagnetic fields, which are often referred as virtual photons with a broad frequency spectrum (Zolotorev and McDonald 2000; García de Abajo 2010). Under certain circumstances, a target material may exhibit resonance effects when interacting with this supercontinuum light source, causing a deceleration or kinetic energy loss in the uniform motion of the STEM probing electrons. In addition, the evanescent character of the transverse electromagnetic fields accompanied with the fast electron enables local resonance modes rather than bulk averaged modes to be probed/excited. This will allow, for example, enhancing or diminishing excitation strength of certain resonance modes as the STEM probe is positioned at different locations relative to the target dielectric structure. STEM EELS, therefore, can be a suitable tool to probe local resonance phenomena, although traditionally it is used to measure the distribution of energy losses of the probing electrons resulting from inelastic scattering due to electronic excitation.

As discussed in section 2.4, the high energy-loss region of a spectrum (core-loss EELS, ≳50 eV) is usually used for identifying elemental and bonding information, while the low-loss region (≲50 eV) provides information on interband transitions, plasmons, and states within the bandgap as it mainly involves excitations of valence electrons or collective modes (R.F. Egerton 2011). In this low-loss region, the energy-loss intensity arising from interband transitions, plasmon excitations, and radiative losses can be described by dielectric response theory, and is thus linked to the optical properties of a material (Hubbard 1955; Ritchie 1957; Z. L. Wang 1996). For example, low-loss signals can be used to derive a materials' complex dielectric function through Kramers-Kronig analysis in ideal cases (Alexander, Crozier, and Anderson 2008; J. Zhu et al. 2014; Stöger-Pollach 2008; García de Abajo 2010; van Benthem, Elsässer, and French 2001). Recent developments in monochromators has improved the energy resolution of EELS to ~10 meV, leading to a much narrower ZLP, with significantly reduced background from the ZLP tail intensity (Ondrej L. Krivanek et al. 2013, 2014). The improved signal-to-background allows subtle features in the low-loss region of the spectrum to be observable. For the purpose of our work here, monochromated EELS enables detection of local resonance modes with energies in the infrared-visible range and peak widths on the order of hundreds of meV.

Excitation of resonance modes can be due to confinement of the progression of optical standing waves by the target's boundary surfaces, which is geometry specific. Depending on the specific target material and its geometric shape, different types of resonance phenomena have been realized and studied using fast electrons. For example, using cathodoluminescence (CL), intensity maxima were observed within the optical bandgap of ZnO wires and tapered ZnO nanoneedles with hexagonal shaped cross-section, which is interpreted as whispering gallery modes (WGM) (Nobis et al. 2004; Czekalla et al. 2010). Similar WGM peaks were also observed in EELS at energies ranging from 6 to 9 eV, where a 200 kV electron beam was positioned 5 nm away from SiO_2 nanospheres (Hyun et al. 2008). Thickness dependent peaks were measured within the direct bandgap region of the spectrum of silicon nanocomposite materials and interpreted as waveguided Cherenkov modes (Yurtsever, Couillard, and Muller 2008). Also, simulated dispersion maps were compared with the experimental EEL spectral peaks observed from GaN and Ge nanowires, and understood to be waveguide modes induced by transition radiation from the relativistic electrons (Arslan et al. 2009; Hyun et al. 2010).

Because the resonances studied in this work are nanoparticle geometry specific, they are referred as "cavity modes" herein. TiO_2, Ta_2O_5, MgO and CeO_2 nanoparticles have been employed to study the behavior of the cavity modes. The results shown in the following sections will focus only on TiO_2 and CeO_2 since observations from Ta_2O_5 are very similar to those from TiO_2 (displayed in section 8.4), and no cavity modes are observed experimentally from MgO as will be discussed. STEM EELS, which is a local measure of extinction (absorption + scattering), is particularly sensitive to resonances in the bandgap region where intensity from electronic excitation is small (i.e., where absorption is minimal). When spectral features within the bandgap were first observed using aloof beam EELS from TiO_2 and Ta_2O_5, there were questions about the origin of these features, as other phenomena apart from cavity resonance, such as surface channeling, have also been argued to generate similar EELS signals.

Therefore, effects of experimentally controlled variables such as crystal orientation, probe position, and electron velocity on the spectral features are investigated. To interpret the complicated spectral features detected, theoretical models and numerical simulations based on classical electrodynamics are performed (by Steven C. Quillin and David J. Masiello from University of Washington as collaborators). With the combination of theory and experiment, the underlying physics involved in generating these cavity modes is elucidated, and the various factors that affect their behavior is examined in detail.

5.2 Materials and Methods

Commercial TiO_2 anatase particles (99.8%) were purchased from Sigma-Aldrich. CeO_2 nanocubes with predominantly {100} surfaces were hydrothermally synthesized by Ethan Lawrence, following a recipe described elsewhere (Zhiqiang Yang et al. 2007; Zhijie Yang et al. 2009). The TiO_2 nanoparticles were dispersed onto TEM sample grids (holey carbon film) using a dry preparation method. For CeO_2 nanocubes, in order to maximize the possibility of finding isolated cubes, the powders were first ground and dispersed in de-ionized water then ultrasonicated for ~15 min. Dispersion from the top layer of solution was drop cast onto a TEM grid to prepare a sample with isolated CeO_2 cubes.

An aberration-corrected NION UltraSTEM 100 microscope coupled with a monochromator and a Gatan Enfinium spectrometer was employed to acquire all the spectra. The microscope was operated at 60 and 40 kV with an energy dispersion of 5 meV per channel. Full width half maximum (FWHM) of the zero-loss peak was better than 25 meV. Convergence and collection semi-angles were 30 mrad and 15 mrad respectively with a 1 mm spectrometer entrance aperture. Gatan Digital Micrograph software was used to process the data. Both EELS line scans and spot acquisitions were performed, where 40 - 50 s acquisition time was used for each spectrum to improve signal-to-noise ratio.

Computational results were produced using the DDA approach (Draine and Flatau 1994), and the basic principles associated with DDA is introduced in section 2.4. Previously, a numerical implementation of the electron-driven discrete dipole approximation (e-DDA) has been developed (Bigelow et al. 2012). This DDA generalization incorporates the electric field profile of an electron beam in a STEM as a substitute for a plane-polarized electric field source. The nanoparticles under study were modeled as perfect cubes, with a dipole spacing chosen to ensure convergence. The dielectric data for each material (displayed in section 8.3) was taken from the literatures: TiO_2 from (Landmann, Rauls, and Schmidt 2012), CeO_2 from (Järrendahl and Arwin 1998), and MgO from (Roessler and Walker 1967).

5.3 Results and Discussion

An example of cavity modes excitation using the electron beam leading to spectral peaks within the bandgap region of an oxide is illustrated in a ~100 nm nanoparticle of anatase (bandgap of 3.2 eV) in **Figure 5.1**. In a defect free crystal, electronic excitations of the valence electrons into the conduction band will only generate spectral intensity in the loss-energy range above the bandgap energy (or the bandgap onset). The focused electron beam is scanned from the vacuum onto an anatase particle sitting at the edge of an aggregate, across a flat facet roughly 80 nm in length, as shown in the HAADF in **Figure 5.1**. In this line scan, the beam starts 25 nm outside the particle and is scanned to 15 nm inside the particle. The corresponding spectra can be grouped as aloof and transmission, depending on whether the electron beam is in vacuum or passing through the crystal. In the aloof beam geometry, the electron beam is positioned outside the sample and the energy-loss signal is generated as a result of delocalized electron-solid interactions (Crozier 2017). The distance from the electron beam to the crystal surface, defined as the impact parameter b, and its influences on the aloof spectral intensity have been discussed previously in Chapter 4 and in the literature (Howie and Milne 1985; Q. Liu, March, and Crozier 2017).

At 25 nm outside the particle (i.e. aloof beam geometry), the EEL spectrum shows a series of weak peaks in the energy range between 0.5 and 3.5 eV, while the bandgap onset is ~3.2 eV. As the beam approaches the particle surface, the aloof spectral intensity rises with the peaks in the bandgap becoming most intense when the electron beam is positioned on the surface. This strong increase in the signal with decreasing impact parameter is expected for the aloof region of the scan (Howie and Milne 1985), however, once the beam enters bulk TiO_2, a pronounced reduction in overall spectral intensity is observed. This overall intensity drop in the transmission spectra is mainly associated with elastic scattering of the incident electrons by the nanoparticle, making it difficult to directly compare the bandgap peak intensities with those in the aloof beam spectra. This comparison can be made via simulation which can separate elastic and inelastic scattering processes (**Figure 5.5**) as will be discussed. In practice, the aloof beam geometry with a rather small impact parameter is desired to generate high intensity spectral peaks in the bandgap region rather than the traditional transmission geometry, as there is no complication from elastic scattering. Therefore, for the following experiments, spot acquisitions are performed in the aloof beam configuration. Considering the cone-shape STEM electron probe and the average nanoparticle thickness (~100-200 nm), the optimum impact parameter to observe the spectral signatures of cavity modes while avoiding elastic scattering contributions is ~4-5 nm, although experimental measurement error and specimen drift will slightly alter the actual impact parameter used for each acquisition.

To understand the dependence of these bandgap peaks on crystal lattice orientation, further experiments are carried out by tilting the anatase nanoparticle target relative to the electron beam source. Two aloof spectra are acquired with the same impact parameters near a {011} surface, when the crystal is tilted both onto and 14° off the [100] zone axis (ZA), as shown in the Kikuchi patterns in **Figure 5.2a**. Tilting the crystal onto the low order ZA ensures that the columns of atoms in the {011} surface facet are parallel to the beam trajectory, ignoring the small convergence angle. **Figure 5.2a** shows no obvious difference in the energies, and only subtle differences in the strengths of the bandgap peaks in the two aloof spectra are observed. This implies that electron channeling effects are not important in generating the spectral peaks observed in the bandgap region.

In contrast to crystal orientation, the velocity of the fast electron significantly affects the strength of the bandgap peaks. Aloof beam spectra are acquired with 4 nm impact parameter from the same anatase crystal using accelerating voltages of 40 and 60 kV (**Figure 5.2b**). The 40-kV spectrum is normalized and vertically shifted so that the conduction band edge is well aligned with the 60-kV spectrum, facilitating comparison of the relative intensities of the bandgap peaks. Here it is evident that there is not only an overall suppression of the bandgap peak intensities with lower beam voltage (which corresponds to a 16% decrease in fast electron velocity), but also the degree of suppression seems larger for the higher energy loss peaks.

To investigate the origin of these bandgap peaks, classical electrodynamics simulations are performed with simulation parameters taken from experiment. The commercial anatase nanoparticles studied here have complicated geometrical shapes and tend to aggregate into irregular clusters, making it challenging to determine their precise three-dimensional shape from the projected HAADF images. However, hydrothermally synthesized CeO_2 nanoparticles exhibit a more well-defined near-cubic morphology (**Figure 5.4**), with refractive indices similar to those of TiO_2 (**Figure 5.3 inset**). **Figure 5.3** compares the simulated EEL spectra of individual TiO_2 and CeO_2 nanocubes, both 160 nm in size. In both spectra, the electron beam is positioned at a low symmetry point outside of the particle with a 4 nm impact parameter so that the beam is not located on any mirror planes (shown as dashed lines in the two dimensional projection of the cube in **Figure 5.5a**). The simulated spectra in **Figure 5.3** show peaks in the bandgap region that are qualitatively similar to those observed in the experiment. Moreover, the simulated spectral features below 3.5 eV from TiO_2 and CeO_2 are quite similar, except for a small blue shift in the peak positions in the CeO_2 spectrum. The similarity of the spectra correlates with the similarity in the energy-dependent refractive indices of CeO_2 and TiO_2 (**Figure 5.3, inset**). This implies that the optical responses in the bandgap region of these two materials will be very similar if their geometrical shapes are the same.

To further illustrate the effect of refractive index on cavity modes in oxide nanoparticles, the aloof spectrum of a 160 nm MgO nanocube is also simulated in **Figure 5.3**, as MgO represents a material with much smaller refractive indices compared to ceria. All spectra are normalized so that the EEL intensities are approximately equal above the band gap. In the MgO spectrum, a gentler intensity variation in the bandgap region (< 7.3 eV) is displayed, suggesting that the bandgap peaks from similarly-sized nanoparticles composed of materials with lower refractive indices are much weaker. This agrees with our experimental observation from MgO where sharp EELS peaks within the bandgap region are not observed (Chapter 4; Liu, March, and Crozier 2017).

Figure 5.4 displays two aloof beam EEL spectra from the same ~250 nm CeO_2 nanocube (experiment: red, simulation: black). Peaks in the bandgap region are similar to those observed in the TiO_2 particles. Comparing the two spectra acquired from two beam positions (**Figure 5.4 a and b**), it can be seen that although the peak energies are roughly the same, the strengths of these peaks are different, illustrating the effect of the electron beam position on the cavity modes strength. This particular nanocube is isolated from other large cubes, although several particles with much smaller sizes are attached to its surfaces. Due to their small sizes, these particles will not themselves contribute to the generation of spectral peaks in the bandgap as will be discussed, but may affect the appearance of the experimental spectrum as the overall effective shape of the specimen is altered. Based on the HAADF image, the cube edge length is measured to be about 270 nm and the particle is tilted roughly 20^o off the [100] ZA. However, these numbers are adjusted when simulations are conducted to achieve the best results. In simulations, the nanocube edge length is set to be 253 nm and the electron beam is tilted by 10^o off the [100] ZA. The discrepancy in the cube edge length may be due to the inaccurate calibration associated with the relatively low magnification, but the reason for the different tilting angles is unclear. Two sets of simple power law background intensity are added to the two simulations respectively to account for the tails of the ZLP in the experimental spectra, producing excellent agreement between experimental and the simulated aloof EEL spectra. The small discrepancies in the peak energies and strengths between simulation and experiment may be due to inaccuracies in the CeO_2 dielectric data from the literature and an incomplete description of the specimen's morphology.

To understand the effects of beam position, electron velocity, particle size, and aggregation scheme on the formation of cavity modes, a series of exploratory EELS simulations of the inelastic electron-nanocube scattering are performed. **Figure 5.5a** shows the 2D projection of a 160-nm ceria cube looking down the [100] ZA which is also the beam direction, and three low symmetry probe positions. For the aloof beam mode, probe position (black) is 4 nm away from the surface. For the two transmission (red and blue) geometries, the probe positions are 4 nm (transmission near surface) and 69 nm (transmission near center) away from the surface respectively. Different than the experiment, elastic scattering is not taken into account in these calculations thus the probabilities of exciting cavity modes with an aloof and transmission geometries can be compared in a more straightforward manner. Interestingly, when the transmission beam is close to the surface of the particle, the cavity modes intensity resembles that with the aloof beam, while the cavity modes intensity is much suppressed in the transmission mode when the beam is away from the surface. Meanwhile, a higher probability for electronic excitation of the valence electrons is found when the beam is near the center of the cube, as evidenced by the larger EELS intensities after the bandgap onset.

Variation of the CeO_2 nanocube size (edge length l = 80 nm and 160 nm) and electron beam acceleration voltage is explored in **Figure 5.6**, using electron voltages ranging from 20 to 100 kV, corresponding to electron velocities of 0.27c to 0.55c where c is the velocity of light in vacuum. Consistent with experiment (**Figure 5.4**), the 80 nm nanocube does not support cavity mode resonances for any of the accelerating voltages considered while the 160 nm nanocube shows an increasing probability for excitation of cavity modes with increasing acceleration voltage (i.e., electron kinetic energy). In both cases the intensity of the electronic excitation of the valence electrons decreases with increasing electron velocity as the inelastic scattering probability is inversely related to electron velocity (R.F. Egerton 2011; Howie and Milne 1985).

To investigate the effect of aggregates on the cavity modes, aloof spectra were calculated for a pair of ceria cubes 160 nm in size, forming a "dimer" structure. The two cubes were initially in close contact with no separation, then the separation distances were increased and the corresponding aloof spectra were calculated. In all cases, the impact parameter was 5 nm and the probe positions are illustrated in **Figure 5.7**. Comparing the peak features from a single cube system with those from the dimer systems shows that extra peaks and energy shifts are associated with the dimer structure, until the separation distance reaches 320 nm which is twice the cube edge length. In practice, particle clusters or aggregates are often present in nanoparticulate systems where it is necessary to consider this interaction between particles in vicinity, as it strongly affects the cavity modes generation by changing the characteristic length and shape of the system. This is the reason why spectral features in **Figure 5.1** and **Figure 5.2** were very complicated and difficult to interpret.

Factors affecting the cavity modes

Factors that determine the exact energies and shapes of the cavity modes include the size, geometry and dielectric of the particle, which are all material related factors. Particle size has the most prominent effect on these cavity modes energies, as shown in **Figure 5.4** and **Figure 5.6**. In fact, a blue shift of the EEL spectral peaks with decreasing size of the isolated CeO_2 cube has been observed experimentally, which is in analogy with the behavior of plasmon modes from metallic nanoparticles (Yamamoto, Araya, and García de Abajo 2001). This can be explained by viewing the cavity modes as a set of standing electromagnetic waves supported by a dielectric particle. The basic idea can be illustrated through a simple analysis considering the hypothetical one-dimensional (1D) particle in a box model as illustrated in **Figure 5.8**, where the standing waves associated with the first three modes or energy states are shown.

Whether this hypothetical model can represent the cavity modes are evaluated using DDA based simulations, where the electrical field intensity profiles and distributions within a 160 nm CeO_2 cube are examined when it is excited by a nearby electron probe. As shown in **Figure 5.9a**, the two electrical field intensity profiles (insets) at 2.37 and 3.22 eV (bandgap peak positions) correspond to two cavity resonant modes or two standing waves with a half wavelength and a full wavelength respectively. The intensity maps in **Figure 5.9b** reveal the same information. This is similar to the standing wave profiles at S= 1 and 2 shown in **Figure 5.8**, although intensity perturbations at the particle surfaces are observed in cavity modes excitations, which are due to the finite potentials associated with the surfaces of a dielectric particle. This result shows that the simple 1D particle in a box mode can be used to establish intuitive understandings of the cavity modes behaviors. From **Figure 5.8**, it can be seen that the mode with the lowest energy (S=1) corresponds to the longest wavelength. Also, shorter characteristic length scale of the dielectric particle (i.e., shorter effective dimension for supporting cavity modes) leads to decreased wavelength of the lowest energy mode (S=1) that can be supported. Thus, for a sufficiently small particle, the smallest mode energy it can support will be larger than the bandgap onset energy, and the strengths of the cavity modes are suppressed as energy absorption occurs in the region above bandgap. The threshold particle size may be estimated based on the simple 1D particle analysis, given the refractive indices of the material (Crozier 2017).

In addition, the geometry of the particle, or the aggregate of particles, is also a critical factor and an important input when solving for the allowed optical eigenmodes of a given structure. Finally, the dielectric effect on cavity modes is clearly illustrated in **Figure 5.3**, where lower refractive indices lead to suppressed cavity modes for a given size and shape of the structure. Moreover, in all the experimental and theoretical EEL spectra, the spectral peaks at higher energy losses (higher dielectric indices) tend to be narrower in width, and two possible interpretations are discussed as follows. First, a large peak FWHM may indicate that rather than one standing wave, several standing waves with very similar energies/wavelengths are allowed to be supported by the dielectric particle when this cavity resonant mode is excited. Therefore, the change of the FWHM of the spectral peaks suggests that for modes with lower energies (smaller S in **Figure 5.8**), the particle can support a larger range of standing waves with similar wavelengths. The second interpretation is that the peak FWHM is an indication of the lifetime of the corresponding cavity mode, therefore cavity modes with higher energies seem to show longer lifetime. For example, the experimental aloof spectrum from the 250-nm ceria cube (**Figure 5.4**) shows a sharp peak at about 3.22 eV with a FWHM of ~0.12 eV, and a broad peak at about 2.16 eV with a FWHM of ~0.36 eV. According to the time-energy uncertainty principle, the lifetimes of these particular modes are $\gtrsim$3 fs and $\gtrsim$0.9 fs respectively. It should be noted that these lifetimes are comparable with the time it takes for light to pass through this CeO_2 particle, which is about 2 fs.

Other influencing factors such as electron velocity, probe position relative to the dielectric structure, and relative orientation of the particle surface to the electron trajectory can be categorized as fast electron related factors. The effects from the probe position are observed in experiment (**Figure 5.1** and **Figure 5.4**) and investigated in theory (**Figure 5.5**). Based on the experiment, the cavity modes intensities are much more significant when the electron beam is on or a few nanometers away (aloof) from the surface of the particle, compared to when the beam is at a transmission position in the bulk area of the particle. This is consistent with work of others where a nonpenetrating electron beam has been commonly used to excite optical waveguide modes or WGM from nanowires and nanospheres (Arslan et al. 2009; Hyun et al. 2008, 2010). Here the drop in the cavity modes strengths in the transmission conditions is mainly due to elastic scattering of the fast electrons by the bulk material. Another possible attribution is that the photons associated with the generated cavity modes may be absorbed by defects in the crystal as TiO_2 can be easily damaged by the transmitted electron beam.

As for the theoretical calculations, in which the effect from elastic scattering is excluded, it is revealed that as long as the probe is near the surface of the cube, the excitation strengths of the cavity modes are very similar for both aloof and transmission conditions. The attenuated intensities after the bandgap onset in the aloof spectrum compared to the transmission near surface spectrum are resulted from the lower inelastic scattering probabilities for the aloof beam condition. Quite different result is obtained when the probe is at the transmission near center position. First, as the probe moves away from the surface, the intensity after the bandgap onset increases due to the reduced Begrenzungs effect (R.F. Egerton 2011). Second, the cavity modes strengths are greatly suppressed and the proposed reason is that when the source of the virtual photons (i.e. electron probe) is close to the center of the particle, it significantly affects the effective geometry of the dielectric structure for supporting the cavity modes (or the standing waves). In other words, the virtual photon source may interact with the standing waves excited in the particle in a destructive way, leading to suppressed cavity modes strength.

In addition, moving the probe around an oxide particle while keeping the impact parameter to be roughly the same can also generate slightly different spectral features (**Figure 5.4**). Its effect is similar to changing the crystal orientation with respect to electron trajectory

(**Figure 5.2a**), where the excitation strength of certain modes may be altered, leading to a change in relative spectral peak intensities, without shifting the energies of the modes.

Insights on Energy-Loss Mechanism

The experimental observations and the numerical results discussed above can be rationalized through a careful analysis of the mechanisms in which fast electrons can lose energy to a dielectric target. The transverse electromagnetic field or the virtual photons associated with the fast electron may be converted into real photons when coupled with a nearby dielectric structure, resulting in real energy losses of the fast electron. This coupling effect has a resonance character, meaning energy is transferred into the photonic modes of the system therefore the spectral features observed in EELS are intensity maxima or peaks (for a spherical particle these resonance modes can be identified as Mie modes). Generally speaking, two most discussed mechanisms for converting virtual photons into real photons are Cherenkov radiation and transition radiation, both of which are coherent electron-induced radiation emission (García de Abajo 2010). Cherenkov radiation is expected when the speed of the electron is faster than the phase velocity of the electromagnetic fields (or light) in the dielectric medium. For semiconductors, it occurs mainly in the bandgap region in the EEL spectra where negligible absorption is allowed, and the energy radiated (or the intensity $I_{Cherenkov}$) increases as increasing electron velocity (v) and material's refractive index (or dielectric ϵ), as $I_{Cherenkov} \propto 1 - \frac{1}{\left(\frac{v}{c}\right)^2 \epsilon}$ (Jackson 1999). For CeO_2 and TiO_2, the refractive indices are in the range of 2.2-3.2 before 3.4 eV (**Figure 5.3** inset), both satisfying the Cherenkov threshold of 2.24 for a 60 kV beam. One way to determine whether Cherenkov radiation significantly contributes to cavity modes excitation is to calculate the cavity modes intensities of a hypothesized material with a small refractive index (e.g. 1.8) for a series of fast electron velocities/voltages. At each incident electron voltage, an aloof beam EELS was simulated over the same energy-loss range (0.6 – 5 eV) from this hypothesized material. The spectral intensities were then summed over the entire energy-loss range for each simulated EELS. These summed intensities, which represent the cavity modes intensities, are plotted vs. the incident electron voltages in **Figure 5.10**. The condition for exciting Cherenkov radiation is not satisfied until electron voltage reaches ~110 kV for this hypothesized material. However, no obvious change in the cavity modes intensity is observed at 110 kV, suggesting that Cherenkov radiation is not a main source for cavity modes excitation. This conclusion may be reasonable because it is known that Cherenkov radiation is inhibited when the thickness/size of the target material is small (Erni and Browning 2008).

Transition radiation, or transition scattering, occurs when a charge uniformly moves in or near an optically inhomogeneous medium in space (Ginzburg 2005). Sometimes, the situation where the electron moves in the vicinity of a localized inhomogeneity in a medium is also called diffraction radiation (Potylitsyn 1998). Unlike Cherenkov radiation, these phenomena are expected at any electron speed (Pogorzelski and Yeh 1973). Experimentally, transition radiation was observed as intensity oscillations in the aloof EEL spectra from MgO and NiO by Cowley, in which the signal increases with decreasing impact parameter and disappeared in the transmission mode (Cowley 1982b, 1982a). The energy loss mechanism was argued to be the result of a "surface channeling" effect where transition radiation is generated due to the modification of the electromagnetic field of the fast electron by the polarization of the crystal, when the fast electron runs parallel to the crystal surface. Such channeling effect is known to be very sensitive to the tilting of the atomic columns relative to the fast electron direction

(Loane, Kirkland, and Silcox 1988). However, as illustrated in **Figure 5.2a**, the cavity modes did not show significant changes when the crystal was tilted onto or off a low-order ZA, thus it can be concluded that surface channeling is negligible in the current observations.

Another energy-loss mechanism is proposed when studying diffraction radiation from relatively large Al_2O_3 spheres, where inelastic signals were found in the energy region where the dielectric function of the material is real, implying negligible energy absorption. It was argued that the observed energy losses originated from the oscillating polarization charges in the material, induced by the passing electron (Abe, Kurata, and Hojou 2000; García de Abajo 2010). Accordingly, the energy loss of the fast electron is argued to result from the retarding force produced by the induced electromagnetic field in the dielectric structure when it acts back on the electron (García de Abajo 1999). Whether this diffraction radiation is the main source of cavity modes excitation remains unclear.

In this work, an analytic Mie analysis is performed (by collaborators, and communicated to the author of this thesis) to elucidate the underlying energy-loss mechanism, since Mie theory exactly describes the inelastic scattering of electrons by a dielectric sphere and has the potential to uncover the origins of the observed bandgap resonances. While idealized, the bandgap energy losses of an oxide nanosphere are qualitatively similar to those of a correspondingly sized oxide nanocube of the same composition, meaning that analytic analysis of the nanosphere's bandgap resonances should provide an understanding of those occurring in the nanocube.

Recall that the Mie scattering cross section for light scattering by a dielectric sphere of radius r is (Bohren and Huffman 2008):

$$\sigma_{\text{sca}}(\omega) = \frac{2\pi c^2}{\omega^2}\sum_{l=1}^{\infty}(2l+1)(|a_l|^2 + |b_l|^2) \qquad 5.2$$

expressed in terms of the Mie coefficients:

$$a_l = \frac{n^2 j_l(nx)[x j_l(x)]' - j_l(x)[nx j_l(nx)]'}{n^2 j_l(nx)[x h_l^{(1)}(x)]' - h_l^{(1)}(x)[nx j_l(nx)]'} \qquad b_l = \frac{x j_l(nx) j_l'(x) - nx j_l(x) j_l'(nx)}{x j_l(nx) h_l^{(1)\prime}(x) - nx h_l^{(1)}(x) j_l'(nx)}$$

where *n* is the refractive index, $x = \frac{2\pi r}{\lambda} = \frac{\omega r}{c}$, j_l and $h_l^{(1)}$ are the Bessel and Hankel functions. It is the denominators of a_l and b_l that encode the resonant frequencies ω of the target as zeros, which are dependent upon both the target index of refraction and the ratio of nanosphere radius *r* to wavelength λ. The dielectric function of oxide nanoparticles is real-valued and nearly constant below the bandgap. This means that absorption is negligible and scattering, if finite, is not due to individual or collective electronic transitions. In addition, analysis of the behavior of the Bessel and Hankel functions in the Mie coefficient denominators demonstrates that the bandgap resonances correspond approximately to the situation where an integer multiple of half wavelengths fit within the nanosphere, similar to the situations illustrated in **Figure 5.8** and **Figure 5.9**. This analytical observation justifies the physical picture of these scattering features as geometric cavity modes.

Although the experimental observations reported in this work do not rely on light scattering but rather upon inelastic electron scattering, Mie theory can be applied equally to both optical and electron beam sources (García de Abajo 1999). Especially in the case where the sphere's refractive index is real-valued, a simple relationship between the two cross sections is established. Further analytic Mie analysis shows that EELS is a local measure of extinction, with extinction being equivalent to scattering since absorption is zero, and proves that these size-dependent EEL bandgap resonances are precisely those geometric cavity modes emerging in light scattering.

Other comments

It should be noted that the cavity modes need to be differentiated with electronic states within the bandgap of the material, as both generate intensity variations and spectral features in the bandgap region of EEL spectrum. Bandgap states are usually associated with defects, dopants or surfaces adsorbates, and they tend to generate plateau shape spectral feature with a more continuously change in the intensity, as shown in Chapter 4 and recent publications (Bowman et al. 2016; Liu, March, and Crozier 2017). In contrast, cavity modes induced features are usually intensity maxima or sharp peaks. In practice, cavity modes can be suppressed or eliminated in smaller oxide nanoparticles, enabling the detection of the bandgap states in the materials.

5.4 Summary

The excitation of resonant optical-frequency geometric modes in oxide nanoparticles are explored using focused electron beams. Employing monochromated EELS in a STEM, the local optical responses of nano-sized dielectric structures can be determined. Excitation of the resonant geometric modes, or the so-called cavity modes, in different oxides gives rise to peaks within the bandgap regions of the energy-loss spectra. TiO_2 and CeO_2 nanoparticles are employed as model materials and a series of experiments have been carried out to characterize the behaviors of these modes. Complementary simulations based on classical electrodynamics are performed to interpret the complex spectral features, as well as elucidating the material-related and fast-electron-related factors that influence the energies and strengths of these resonances. The size, geometry and dielectric function of the system determine the energies and shapes of these cavity modes, while electron velocity, probe position, and relative orientation of the particle surface to the electron trajectory influence the strength of different cavity modes without shifting their energies. Possible energy-loss mechanisms involved in this phenomenon are discussed. Using an analytical Mie analysis, it is revealed that these geometric cavity resonances are encoded in the scattering properties of an oxide particle when exposed to light or electron irradiation.

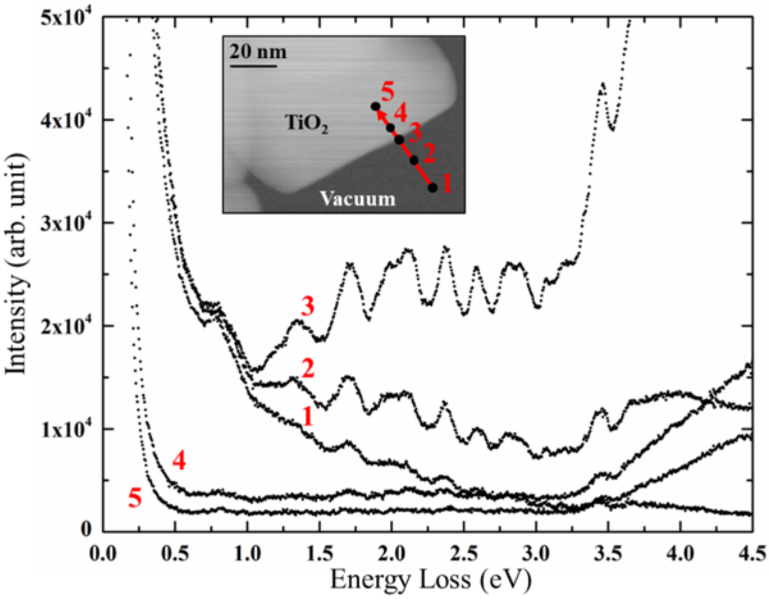

Figure 5.1: An EELS line scan was conducted at 60 kV from vacuum onto an anatase particle as shown in the inset. A series of spectra are displayed with different probe positions as marked, and the distances from these beam positions to the TiO_2 particle surface are: 1 - 25 nm; 2 - 12 nm; 3 - on surface; 4 - 6 nm; 5 -15 nm.

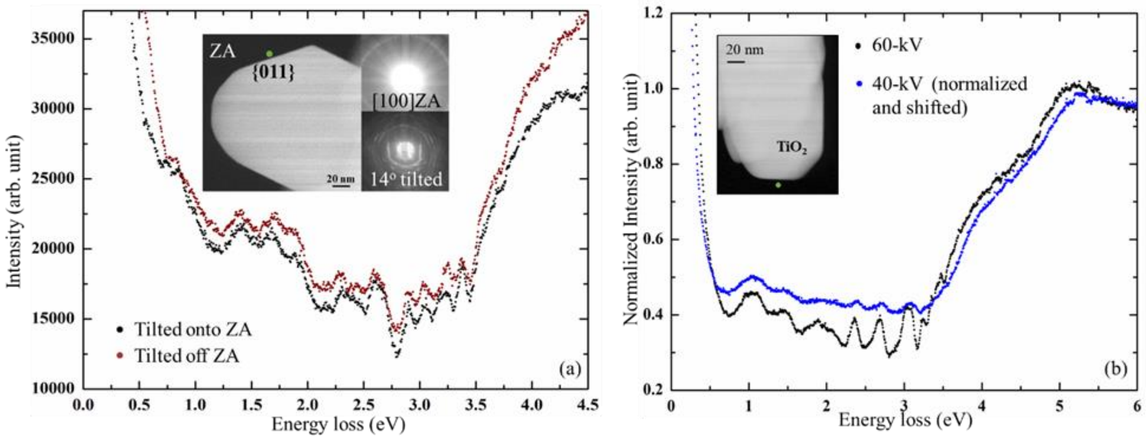

Figure 5.2: (a) Two aloof spectra were taken when the probe (green dot) was about 4 nm away from an {011} surface of an anatase particle, when it was tilted onto (black) and 14° off (red) the [100] ZA at 60 kV. Inset shows the HAADF image of this particle on ZA, and the two Kikuchi patterns taken when the particle was on ZA and 14° tilted. (b) Two aloof spectra from an anatase particle acquired at 60 kV and 40 kV. The impact parameter was kept at about 4 nm in the two acquisitions and the probe position was shown in the HAADF image (inset). The 40-kV spectrum was normalized and shifted so that intensity after the bandgap onset aligns well with the 60-kV spectrum.

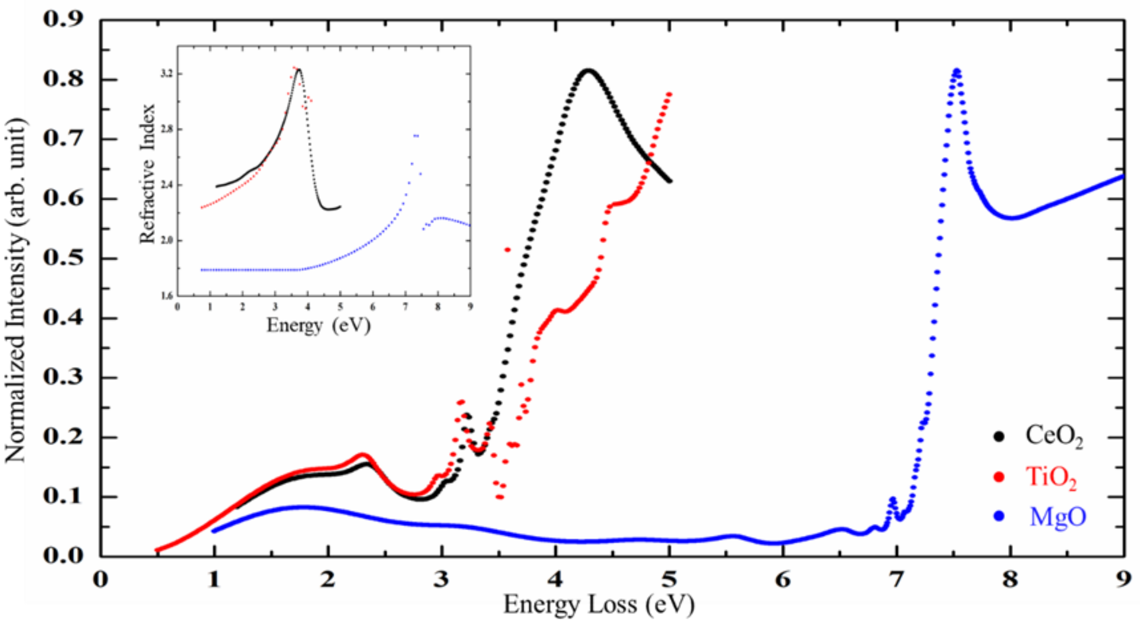

Figure 5.3: Calculated aloof EEL spectra of TiO_2, CeO_2 and MgO cubes with the same edge length (160 nm). The electron beam is positioned at 4 nm outside of the nanoparticle surface at a low symmetry point. The inset displays the real-valued component of the energy dependent refractive indices of the three materials.

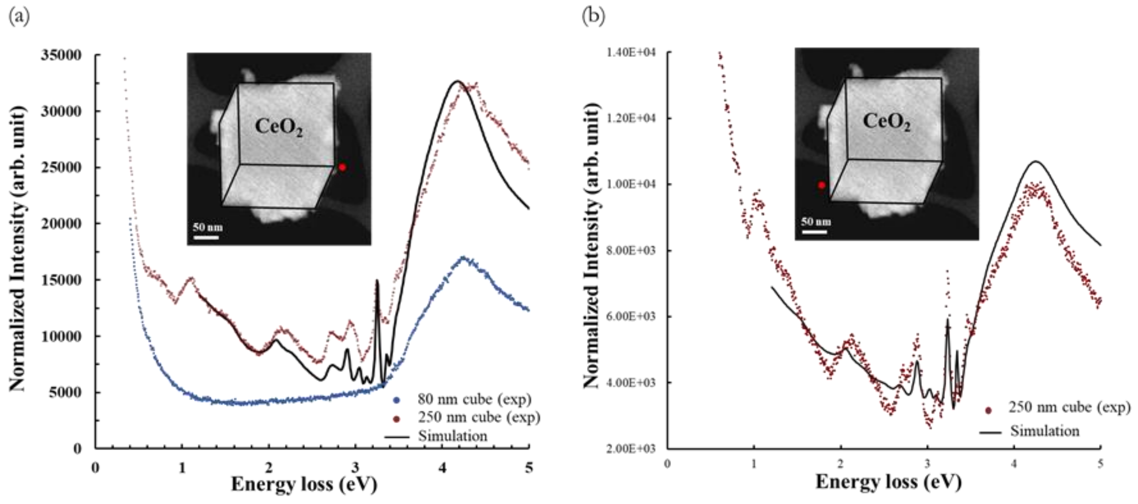

Figure 5.4: Experimental (red) and computed (black) aloof EEL spectra with the electron beam positioned 4 nm (a) outside of a corner, and (b) away from a facet of a well-defined CeO_2 cube ~250 nm in size. The aloof EEL spectrum (blue) from an isolated 80 nm cube shows a featureless bandgap. The insets are the HAADF images of the ~250 nm cube with the two beam positions denoted by the red bullets.

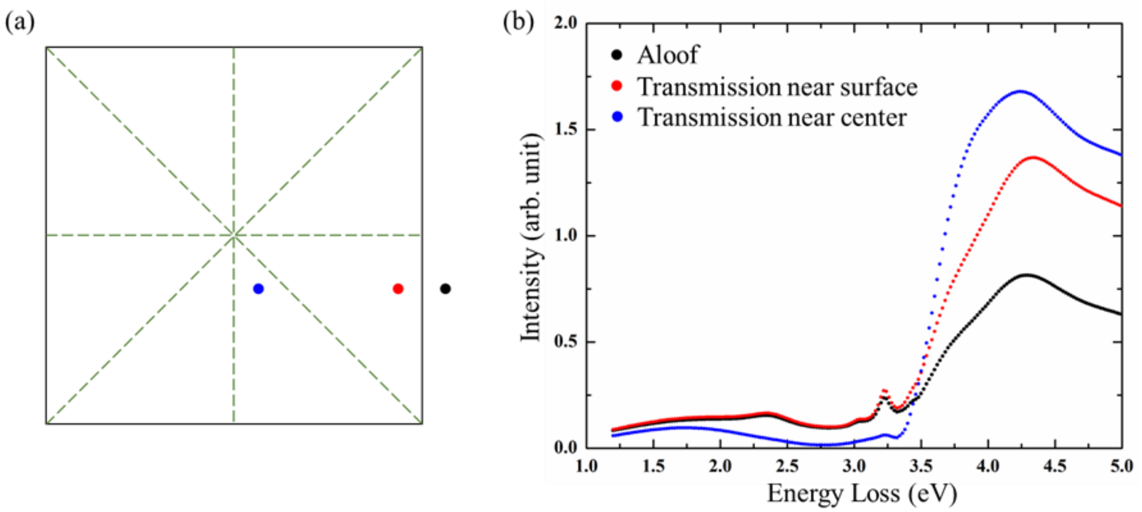

Figure 5.5: (a) 2D projection of a CeO_2 cube model with three low symmetry beam positions (colored dots) when looking down the beam direction. Edge length is 160 nm. Dash lines represent the mirror planes for the cube. (b) Calculated spectra from the three beam positions with 60 kV incident electrons.

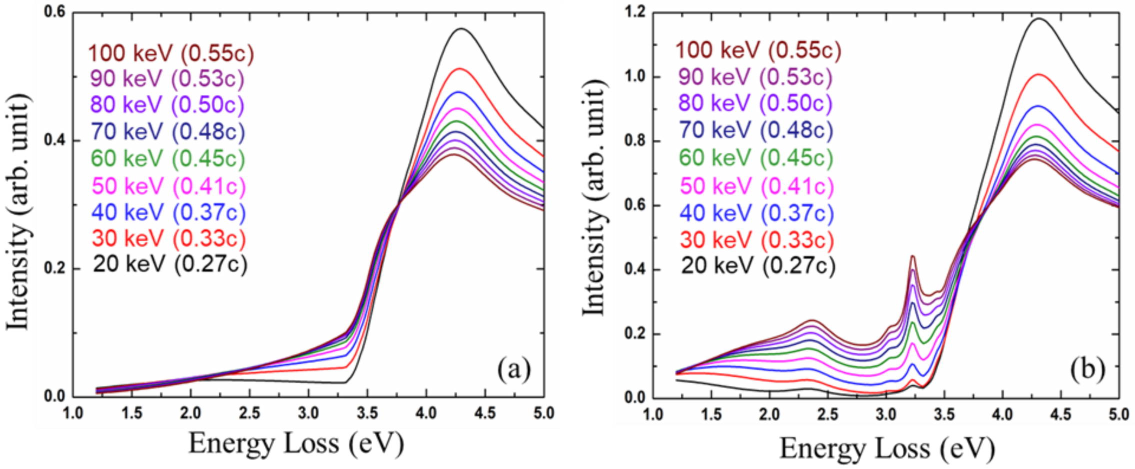

Figure 5.6: Calculated aloof spectra from CeO_2 cubes with two different particle sizes, (a) 80 nm and (b) 160 nm. Beam position was kept at 4 nm away from the surfaces. For each cube size, the incident electron voltage varies from 20 to 100 kV with a 10-kV step.

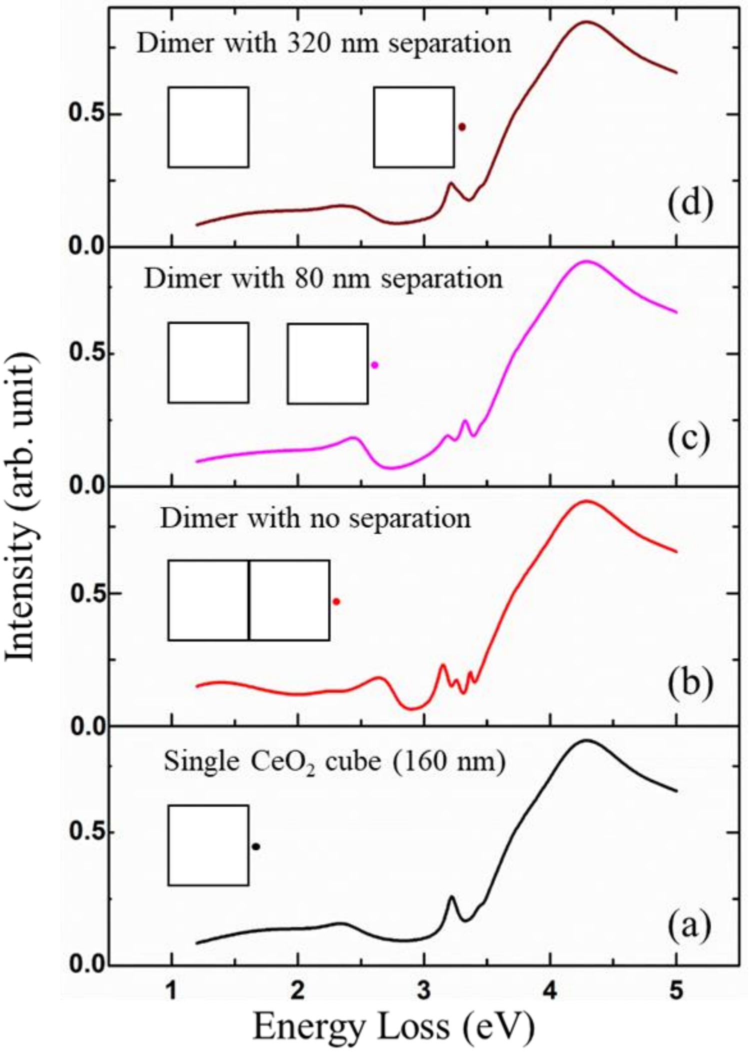

Figure 5.7: Calculated aloof spectra showing the interaction between two cubic particles. The cube size is kept the same with 160 nm as the edge length. Beam position was kept at 5 nm outside the cube surface. (a) Spectrum from a single cube; (b) Spectrum from dimer cubes adjacent to each other with no separation; (c) spectrum from dimer cubes separated by 80 nm; (d) spectrum from dimer cubes separated by 320 nm.

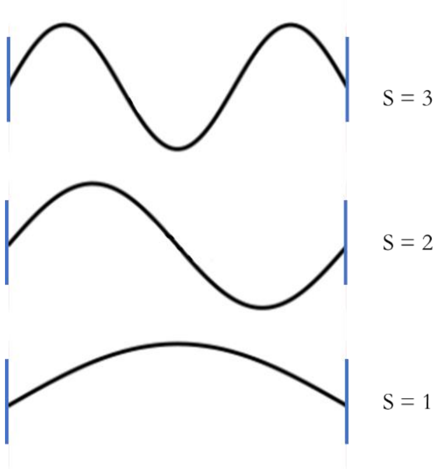

Figure 5.8: A schematic illustrating the standing waves for the three low energy modes/states (S = 1, 2, 3) supported by a one-dimensional particle in a box.

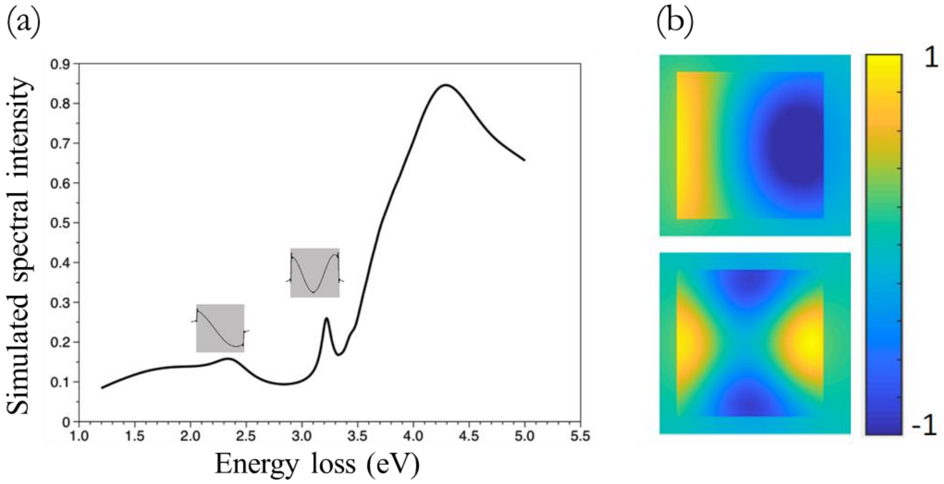

Figure 5.9: (a) Simulated aloof beam EELS from a single CeO_2 cube (160 nm). Beam geometry is the same as that in Figure 5.7a. The two insets are the electric field intensity profiles within the cube, at the two spectral peak energies corresponding to two cavity modes. (b) The intensity maps show the internal electric field distributions associated with the cavity modes at 2.37 eV (top) and 3.22 eV (bottom).

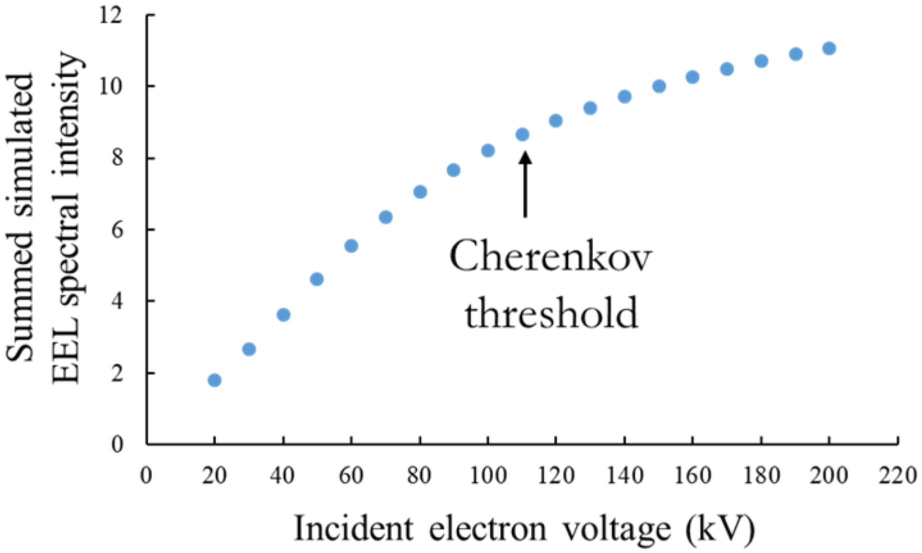

Figure 5.10: Summed simulated EEL spectral intensities (energy-loss range: 0.6-5 eV) from a hypothesized material with low refractive index (1.8) when various incident electron voltages (20 to 200 kV with a 10-kV step size) are applied.

6 *In Situ* Light Illumination System for an Aberration-corrected Microscope

6.1 Motivation

As discussed in section 2.5, *in situ* TEM has been recognized as an essential tool in the field of catalysis, and developing specific *in situ* (S)TEM techniques for the study of photocatalysts is of great importance for probing their fundamental reaction and deactivation mechanisms. An *in situ* light illumination system, therefore, needs to be built so that photoactive nanomaterials can be exposed to photon irradiation in a TEM. Combining the superior spatial resolution with the *in situ* capability, it is hoped that the optical and catalytic behaviors of photoactive materials can be observed under (near) reaction conditions at the nano- or atomic-level.

Several approaches that allow exposure of TEM samples to photons have been investigated over the years and are summarized as follows. A light illumination system was built by Yoshida et al. and coupled to a high resolution TEM, which was used to study the decomposition of hydrocarbons on catalytic TiO_2 at the atomic level (K. Yoshida, Yamasaki, and Tanaka 2004). Cavalca et al. developed two types of TEM specimen holders where a lens-based and a fiber optics-based illumination system was integrated on the holder respectively, and proof-of-concept experiments were demonstrated (Cavalca et al. 2012). Additionally, a novel optical TEM holder with a multimode fiber, a piezo-motor driven metal tip, and a bias voltage of around 10 V was developed by Zhang et al. for a more specific purpose, which measures the optoelectronic property of nanostructures (C. Zhang et al. 2014).

Although *in situ* photon irradiation has been realized, each approach described above has some limitations. The disadvantage of the first approach is that the TEM samples would always sit in the ultrahigh vacuum of the high resolution microscope, unless a windowed cell *in situ* holder is used, which will introduce issues such as light shadowing, absorption and scattering by the holder material and high pressure gases or liquids. By coupling the illumination systems onto TEM specimen holders, the last two approaches exclude the possibility of having heating or cooling elements on the holders, thus the specimen can only be observed under ambient temperature.

Recently, Miller and Crozier have developed an illumination system in which light is introduced via a fiber optic based device through a separate port of an ETEM (FEI Tecnai F20 at Arizona State University) (B. Miller et al. 2012; B. K. Miller and Crozier 2013). This *in situ* light illumination system is referred to as the Tecnai system hereinafter. This design allows simultaneous exposure of the sample to high intensity photon irradiation with a broad wavelength range, various gas species with pressures up to a few Torr, as well as heating, cooling, biasing or mechanical stimulus since various specially designed specimen holder can be employed. Using the Tecnai system, Zhang et al. have conducted the first atomic resolution study of the surface structural transformation of anatase nanoparticles upon exposure to light and water vapor. It was observed that, under conditions relevant to gas-phase photocatalytic water splitting, the initially crystalline surface structure of anatase nanoparticles converts to a disordered phase one to two monolayers thick, accompanied with formation of Ti^{3+} cations. This surface phase resulted from a direct photo-reaction between the top one or two monolayers of the anatase crystal surface and the adsorbed water, and is most likely a stabilized form of titania hydroxide (L. Zhang, Miller, and Crozier 2013). In fact, this amorphization of anatase surface structure has also been observed after *ex situ* photocatalytic water decomposition reaction is performed (L. Zhang 2015), proving that the structural changes observed *in situ* can actually represent the changes occurred during real catalytic reactions.

Later, an aberration-corrected ETEM (FET Titan 80-300) was installed at Arizona State University in 2014. With the imaging C_S corrector, much higher interpretable resolution and suppressed image delocalization can be achieved compared to the uncorrected ETEM, making it possible to reveal further detailed information on nanoparticle surfaces. It is thus valuable to add an *in situ* illumination capability to this Titan microscope, using design concepts similar to that of the Tecnai system. In this chapter, the design, testing and application of the *in situ* light illumination system for the Titan aberration-corrected ETEM are discussed in detail.

6.2 Instrument Development

6.2.1 Design Criteria and Considerations

Two primary goals are set for this project: (A) the desired optical functionality of this *in situ* light illumination system needs to be realized, i.e. sufficiently high photon intensity needs to be achieved at the sample area, and (B) integration of this illumination system onto the ETEM should not significantly affect the microscope capabilities of introducing reactive gases into the environmental cell, as well as obtaining high resolution images and good quality EELS data. In short, goal (A) deals with the functionality of the system, while goal (B) deals with the compatibility of this system with the microscope. To achieve these two goals, various factors/issues need to be considered, which are discussed as follows.

Considerations related to functionality (goal (A))

The first step involved in realizing the functionality of the *in situ* light illumination system is to decide how to direct and focus light from a light source onto the TEM sample. A fiber optic based approach has been used previously in the Tecnai system due to its simplicity and flexibility, compared to a lens based design. It is thus rational to continue using this approach for the design of the current system. To allow greater flexibility in the specimen holder choice, a separate port on the side of the column close to the sample region needs to be selected for inserting the fiber optic. The EDX port is used in the Tecnai system, which is not feasible for the current design on the Titan microscope as access to EDX spectroscopy is desired. Instead, the port that has initially been designed for inserting the objective aperture rod was selected to also serve as the port for inserting the fiber optic. Directing the light from the source, through the port and onto the sample area is a challenging task, mainly because of the geometric constraints set by the spatial limitations of the port and the limited space between the microscope pole pieces and the specimen stage (**Figure 6.1** and **Figure 6.3**). In other words, the fiber going through this port is constrained to have a much flatter contour, compared to that going through the EDX port, limiting the upward pointing angle of the fiber tip. Basically, the spatial limitations associated with the objective aperture port can be viewed as two bores with diameters of 10 and 6 mm respectively, illustrated by red dash-dotted lines in **Figure 6.1**. The distance between the upper and lower objective pole pieces in this microscope is roughly 5.4 mm. Also, if a bulk heating holder (Gatan, Inc.) is employed, the TEM sample sits inside a bulk furnace which has a thickness of ~2.4 mm with an inner diameter of ~3.4 mm (**Figure 6.3**). All of these geometric constraints, along with the maximum allowable curvature of the fiber, limit the maximum angle at which the fiber can approach the sample.

The spatial distribution of the photon intensity reaching the sample area is another factor that needs careful consideration in order to achieve the desired functionality. Since the materials of interest in this work are nanoparticles, standard TEM grids or metal meshes (both of which are circular in shape with ~3 mm diameter) are the most common supports used for loading these nanoparticles. Ideally, it is desired to have high intensity light uniformly illuminating the whole support. In practice, however, the light emitted from the fiber is not collimated, and has a non-uniform intensity distribution (B. Miller et al. 2012). In other words, a bright spot containing relatively higher photon intensity is expected to be present near the center of the spatial distribution of the light intensity (discussed later). To ensure that sufficient photon intensity can reach the sample area, the light source needs to have high brightness or radiance. Furthermore, it is essential to be able to adjust the position of the fiber once it is installed on the microscope, ensuring that the bright spot can be aligned with respect to the electron optical axis of the TEM. Thus, a mechanism that can precisely control the position of the fiber optic is required. Fortunately, this is also the requirement for the objective aperture rod. Therefore, retracting/inserting (x-direction) as well as lateral shifting (y-direction) of the installed fiber can be achieved with 0.1 μm precision using two rotors and a bellows originally built by FEI for controlling the objective aperture rod. Movement in the vertical direction or z-direction (up or down) is not available but also not a requirement for achieving the desired optical functionality. The x and z directions are labeled in **Figure 6.3** for clarification.

Additionally, the emitted light from the light source need to be focused to a sufficiently small spot at the entrance of the fiber to suppress intensity loss, which can only be achieved when a small source is used (i.e., light originates from a small spot). Also, as UV photocatalysts are the focus of this work and TiO_2 anatase is the model material involved in this project, it is required that the wavelength range of the emitted light should cover the UV range, i.e., at least a portion of the emitted photons should have energies larger than the bandgap energy of anatase (>~3.4 eV or <~365 nm). For this work, high radiance or power is desired specifically for the UV portion of the emitted light, in order to expedite the photocatalytic or photochemical reactions taking place when anatase is used as the material under investigation. Also, the optical fibers and fiber connectors used to direct light should be able to withstand the possible damages caused by high energy UV photons.

Considerations related to compatibility (goal (B))

Integrating the fiber optic based light illumination system onto an ETEM is not trivial. First of all, seals need to be made so that after installation of the system, the microscope chamber can be pumped down to the desired vacuum level (~10^{-7} Torr in the objective pole pieces area). This also means that the components sitting inside the microscope vacuum should be vacuum compatible (no outgassing) and residual air in these components should be easily pumped out. In addition, it is desired that these components can be baked at 100-150 °C before installation to suppress contaminations to the microscope chamber.

Second, these components need to be stable when exposed to various reactive gases such as water vapor, O_2, H_2, etc., during *in situ* experiments. Therefore, they should not be made of materials that are easily hydroxylated, oxidized or reduced.

Third, these materials should not degrade the imaging and spectroscopy performances, which means they should not interfere with the strong electromagnetic field (usually ~1-2 T) in the pole piece area, and should be able to conduct away the spurious, scattered, and secondary electrons in order to eliminate any charging effect.

Other considerations

In addition to the considerations related to the system's functionality and compatibility, it is also important to ensure that no significant leakage of X-rays generated from electron-solid interactions is present after installing the system through the objective aperture port. Moreover, the system should be designed in a way that it can actually be fabricated at an affordable cost. Also, the assembling/disassembling of various components, as well as installation/dismount of the system should not be too difficult.

6.2.2 Design Implementation

Each of the considerations discussed above has been addressed in the current system. The light source employed in this work (and also in the Tecnai system) is an Energetiq EQ-99 laser powered broadband light source. A detailed description of the source and associated operation principles can be found in (B. Miller et al. 2012). Basically, an infrared laser beam is focused to a spot to heat a Xenon plasma ~100 μm in size, where broadband light is then emitted. This light source provides high radiance over the wavelength range of ~200 to 800 nm, with a quoted total power output as 800 mW. It should be noted that due to various losses, the final power reaching the TEM sample is 45.6 mW if all wavelengths are counted, or roughly 8 mW if only the UV portion of the wavelengths is considered. The light emitted from the source is then focused onto an optical fiber with a diameter of 600 μm and a length of 2 m (Ocean optics, Inc.) using a pair of parabolic mirrors coupled to the light source constructed by Energetiq. This long fiber, which is labeled as fiber 1 in the figures, is necessary as it connects the light source with a second fiber which goes through the objective aperture port on the microscope for directing light onto the TEM sample as shown in **Figure 6.1**.

Designing a device that supports the second fiber and fulfills the requirements described in the previous section was thus the primary task of this project. AutoCAD was used to construct the original design of this device (shown in section 8.5), which was then fabricated by the technicians at the mechanical instrument shop at Arizona State University. **Figure 6.2a** shows a design drawing of the assembled device, located at the optimum position with respect to a tilted sample in between the objective pole pieces. A picture of the actual device is also shown below the design drawing.

This device has five major components: a fiber holder, a specially designed optical fiber (fiber 2), a fiber adapter, a vacuum feedthrough and a screw cap, as illustrated in the exploded view drawing in **Figure 6.2b**. The main function of the fiber holder is to support the optical fiber while maintaining a certain contour/bend so that the tip of fiber points upwards leading to the TEM sample. This is realized by careful design of the shape and structure of the fiber holder, which consists of an axial symmetrical portion (on the right side of vacuum seal A) and a non-symmetrical portion (on the left side of vacuum seal A). It should be mentioned that the non-symmetrical portion sits inside the microscope high vacuum while the axial symmetrical portion does not, and an O-ring is placed at their joint (point A in **Figure 6.1**) to form the vacuum seal. A 3-mm diameter hole is drilled along the center axis of the symmetrical portion of the fiber holder for inserting the optical fiber (outer diameter: 0.8 mm). The bend is only present within the non-symmetrical portion with a designed radius of 25 cm, which is the maximum allowable curvature of the fiber to avoid inefficiency in light transmittance. A copper tubing is attached to this portion of the holder following its contour, and the fiber goes through this tubing so that the desired bend is achieved. The non-symmetrical portion of the holder also needs to fit within the 6-mm spatial limitation of the objective aperture port, limiting the maximum obtainable upward angle of the fiber tip which is measured to be ~9^{o} (**Figure 6.3**). In addition, several small apertures are drilled on the copper tubing as well as the main body of the fiber holder (made of phosphor bronze) but only within the non-symmetrical portion. These small apertures allow the residual air trapped in the device to be pumped out faster.

Fiber 2, which is specially designed and ordered from Ocean Optics, has a total length of 268.55 mm, a refractive index of 1.47 and is suitable for transmitting UV light (solarization-resistant). In contrast to fiber 1, which has a standard polymer-based protective buffer and jacket, this fiber is only coated with an aluminum buffer to protect its silica core and cladding. This is because fiber 2 is exposed to high vacuum or reactive gasses once installed onto the microscope, and the aluminum buffer fulfills the criteria of no outgassing or degradation in these conditions. It is also conductive and non-magnetic, therefore does not induce unwanted charging effect or interfere with the magnetic field introduced by the pole pieces. One end of the fiber, which is referred as the fiber tip in this chapter, has a 30° cut as shown in **Figure 6.3**. This cut is essential because, based on Snell's law, light coming out of the fiber tip is refracted upwards. When the fiber is inserted at an optimum position and the TEM sample is tilted 30° towards the fiber, the light cone (shown in green in **Figure 6.3**) emitting from the fiber tip strikes the sample without being blocked by the bulk furnace in the specimen holder. Moreover, calculations suggest that majority of the light is emitted from the center of the cross section of the fiber tip (B. Miller et al. 2012), giving rise to a high intensity light cone (shown in dark green) which covers the center of the TEM sample. The other end of this fiber is terminated with a ferrule which is a standard SMA 905 fiber connector (shown in black in **Figure 6.2b**). Care has been taken when selecting the composing materials for this ferrule so that this entire fiber can be baked in the 100-150 °C range.

The 3-mm hole drilled in symmetrical portion of the fiber holder is too small for accommodating the ferrule, thus a fiber adapter is made which has a 9-mm drilled hole along its center axis. In addition, a rotatable 1.33 CF flange is placed at one end of the fiber adapter, which interfaces with the same size flange on the vacuum feedthrough (ordered from Ocean

Optics). The interface of this flange pair is noted as vacuum seal B in **Figure 6.1**, which allows fiber 2 sits under the microscope high vacuum while fiber 1 does not. Having a rotatable flange is essential, as the 30° cut at the fiber tip needs to be in the correct orientation (**Figure 6.3**) for refracting light upwards and the rotatable flange allows easier aligning of this orientation. In addition to forming the vacuum seal, another purpose of the vacuum feedthrough is to couple fiber 2 with fiber 1 using the two SMA fiber connectors on both sides of the flange. This vacuum feedthrough is selected to be extreme solarization-resistant (XSR) to suppress inefficiency in transmitting the UV light.

Besides the vacuum feedthrough and the fiber adapter, a hollow screw cap is also a necessary component of this device which is used for fixing the assembled device onto the objective aperture port of the microscope, as well as forcing the O-ring to be compressed when the fiber holder is screwed in thus forming the vacuum seal at point A.

X-ray leakage test has been performed after installing this device onto the microscope, and the detected leakage is below the maximum allowable limit, confirming that the emitted X-rays can be sufficiently absorbed by the fiber holder.

Light distribution and fiber alignment

As mentioned in the previous section, the spatial distribution of the light intensity coming out from the fiber tip is expected to be non-uniform. Two methods have been developed to gain knowledge on the detailed intensity distribution (B. Miller et al. 2012). In principle, the distribution can be calculated based on Snell's law using a numerical model, or it can be measured outside the TEM using an optical microscope. The latter method is considered to be more accurate thus is also applied here. The vertical distance between the center of a TEM grid and the center of the fiber tip cross section is designed to be 1.5 mm and is measured to be about 1.4 mm after the device is fabricated. Outside the microscope, a translucent screen representing the TEM sample is placed close to this vertical distance away from the fiber tip and then tilted 30° towards the fiber tip. An optical microscope (Lumenera Infinity 2) is used to record the projected light spot on the screen. A series of exposure time needs to be used as the intensity range on the screen exceeds the dynamic range of the digital camera on the optical microscope. More specifically, shorter exposure time is used for obtaining the higher intensities near the center of the distribution, while longer exposure time is used for acquiring the lower intensities in the tails of the distribution. By normalizing and combining images with different exposure times, a plot of the measured intensity distribution of the current system is shown in **Figure 6.4**. The three contours (black dashed lines) correspond to 10%, 50% and 90% of the maximum intensity. As expected, light intensity drops quickly as it goes further away from the most intense point. The bright spot may then be defined as the area where light intensity is above 90% of the maximum intensity. The dimension of the bright spot is estimated to be 0.5×0.3 mm, which only covers ~1.7% of the total area of a standard 3-mm TEM grid.

Because of the small coverage area of the bright spot, it is essential to precisely align the fiber tip with respect to the optic axis of the TEM so that the bright spot strikes at the center of the sample area. This is challenging because the location of the fiber tip cannot be directly observed once the fiber is installed onto the TEM. An aligning procedure is thus developed based on the principle of reversibility of optical path, and a schematic is shown in **Figure 6.5a**. To find the optimum position of the fiber, green phosphor nanoparticles (ZnS based P22) are first loaded onto a standard TEM grid which is then placed at the eucentric height in between the pole pieces and tilted 30° towards the fiber. Upon irradiated by the electron beam, a phosphor particle is assumed to emit photons isotropically. A portion of the emitted light may enter fiber 2 if it is placed nearby, which is then transmitted to fiber 1. Instead of connecting to the light source, fiber 1 is interfaced to a photosensor system during the alignment procedure. The main component of this photosensor system is a photomultiplier tube (PMT) made by Hamamatsu Corporation, which is chosen to be most sensitive to green light (H6780-02 module). The output voltage from the PMT increases with increasing incoming photon intensity or number, and a position of fiber 2 can be found by moving it in the x and y directions until maximum voltage is achieved, which is noted as the maximum voltage position.

An important question is whether this maximum voltage position coincides with the optimum working position of the fiber shown in **Figure 6.3**. As illustrated in **Figure 6.5b**, point O is the location of the phosphor nanoparticle which is also the origin of the isotropically emitted green photons. The blue line represents the cross section of the fiber tip with point F being the center point of the cross section, and the dashed red line is the perpendicular bisector of the blue line. The black arrow is along the center axis of fiber 2. Based on Snell's law, light emitted from O must strike at F at a fixed angle (47° relative to the red dashed line), in order for it to travel along the center axis of fiber 2. As fiber 2 is moved along the x-direction, there is only one x coordinate allowing the above described light path geometry to be set up (shown in **Figure 6.5b**), and it is assumed that this coordinate is both the maximum voltage position and the optimum working position. In other words, at this particular light path geometry, it is assumed that maximum number of photons enter the fiber when a phosphor particle is irradiated by electrons, and meanwhile, maximum light intensity strike at the electron optical axis when the light source is connected to the end of fiber 1. Since the vertical distance between

F and O is measured to be about 1.4 mm and is fixed when fiber 2 is moved in the x-direction. The horizontal distance between O and F when this geometry is fulfilled can be calculated and is about 2.9 mm. However, when fiber 2 is at the maximum voltage position, the horizontal distance between O and F is measured to be about 1.1 mm. The discrepancy may be due to inaccuracy in the measurements or it may indicate that the assumption above is not correct. Careful modeling and calculations still need to be performed to verify if this assumption is correct, thus determining if the alignment procedure developed here is reliable.

Testing

It is important to know if the imaging and spectroscopy conditions will change when high intensity light strikes onto a TEM sample. Commercial anatase nanoparticles are used as the test material supported by a standard grid, which is tilted 30° towards the fiber that is placed at the maximum voltage position. An adjustable aperture attached to the Energetiq light source can be used to control the number of the photons entering the optical fibers thus controlling the light intensity striking at the sample. As the diameter of this aperture is switched between its maximum (12 mm) and minimum (0.8 mm) limits, the photon intensity arriving at the sample area changes significantly, and a corresponding image shift is observed. **Figure 6.6ab** are images of the same anatase cluster taken under minimum and maximum light intensity conditions without shifting the specimen stage or changing any other microscope parameters. The location of the cluster image on the CCD detector under minimum photon intensity condition (**Figure 6.6a**) is represented using an outline (red dashed curve) in **Figure 6.6b** to reveal the image shift resulted from changing the light intensity. It should be noted that the shift is not a movement of the anatase particles relative to the supporting holey carbon film, but is rather associated with the entire image. It has been confirmed that this image shift is not due to mechanical or thermal instability and only occurs upon switching of the photon intensity. When high intensity photon strikes the sample area, significant number of secondary electrons is likely to be emitted which can result in a tilt of the electron beam leading to the observed shift of the image. However, this image motion is only observed during the process of adjusting the aperture size, and is not present once the light intensity is kept unchanged. To some extent, this light induced image motion confirms that the sample area is actually exposed to high photon flux when fiber 2 is placed at the maximum voltage position. Furthermore, it may be possible to testify if the maximum voltage position coincides with the optimum working position using this image motion. It is expected that, if the size of the electron beam is kept small while changing the position of fiber 2, the maximum image motion (i.e. largest shift magnitude) will be observed when the bright spot of the emitted light strikes at the optical axis. This is because, a small electron beam will be more sensitive to changes of the exact origin of the secondary electron emission, which is assumed to be the location of the bright spot projected on the sample, resulting in different degrees of electron beam tilting when photon intensity is switched by adjusting the aperture size. Future experiments need to be conducted to evaluate the feasibility of this method.

Low-loss EEL spectra have also been acquired under maximum and minimum light intensity conditions using 80 kV monochromated electron beam, as shown in **Figure 6.7**. The image movement after changing the light intensity was partly compensated by adjusting the projector lens currents. No significant change in the energy resolution or spectral features is observed under these two conditions, except for a small difference in the signal intensity which is probably due to a change in the electron path length in the sample caused by the image shift.

6.3 Application

The motivation of building this system is to study detailed structural transformations of photocatalysts when they are exposed to (near) reaction conditions. Therefore, apart from conducting the primary testing described above, it is also desired to apply this system onto studies of photo-reactions and related structural changes. The first photo-reaction that is chosen to be performed using this system is actually the reaction that has been studied in the Tecnai system, i.e. the photo-reaction between the surface of the anatase nanocrystals with water vapor. This reaction is selected because of two reasons. First, since this reaction has already been studied, the experimental results or the observations can be predicted. If the predicted results can be achieved then it is evident that the desired functionality of the current system is successfully achieved. Second, since the Titan microscope is equipped with an image corrector which is supposed to benefit the study of surface structures, it is hoped that a deeper understanding of the structural change resulted from this reaction can be gained.

Pure crystallized and shape-controlled anatase nanoparticles have been synthesized using a hydrothermal method described elsewhere (H. Y. Zhu et al. 2005; Deng et al. 2010; L. Zhang 2015). A 3-mm Pt mesh was used as the support for the anatase nanoparticles for the following *in situ* experiments. This is because the standard holey carbon film can be easily etched away when exposed to light and water, whereas Pt mesh does not degrade under these experimental conditions. A Gatan hot stage was used as the specimen holder and the sample was heated to 150 °C to suppress contamination.

To expose the anatase nanoparticles to conditions relevant to vapor phase photocatalytic water splitting, the sample is tilted 30° towards the fiber which is placed at the maximum voltage position obtained using the alignment procedure described in the previous section.

The Energetiq light source is employed with the maximum aperture size selected and with no optical filter inserted, i.e., the sample is illuminated with both UV and visible photons. To introduce water vapor into the environmental cell, a glass bottle containing liquid DI water is connected to a leak valve on one gas inlet of the cell. The liquid water is partly vaporized as the vapor pressure of water at room temperature is approximately 20 Torr. By adjusting the opening of the leak valve, the water vapor pressure in the environmental cell can be controlled. In this experiment, the water vapor was first kept at 1 Torr for 11 h then increased to 8 Torr for 3 h while the sample is exposed to light.

The Titan microscope is operated at 300 kV and anatase surface structures were examined before and after the 14 h *in situ* exposure to light and water, under high vacuum condition ($\leq 10^{-4}$ Torr) with the light fiber in the retraction position (no photon irradiation) and the specimen stage at zero tilt position. It should be noted that both electrons and photons can generate electron-hole pairs in the anatase which may result in the formation of surface active sites for water dissociation (L.-Q. Wang, Baer, and Engelhard 1994; L. Zhang, Miller, and Crozier 2013). Therefore, relatively low electron dose rate (~300 $e^{-}/\text{Å}^2 \cdot s$) is used for acquiring the high resolution images to suppress the effect of electron irradiation on the structural changes taking place in anatase. This electron dose rate, or the corresponding incident electron power density is much larger than the incident photon power density (L. Zhang, Miller, and Crozier 2013). However, the per unit area energy transferred from the electron beam to the sample is estimated to be ~54 J/cm^2 while that from the light is ~2777 J/cm^2, since the time it takes to adjust the focus and acquire a few high resolution images (i.e., electron irradiation time) is roughly 100 s whereas photon irradiation lasts for 14 h in this experiment. Therefore, the energy deposited to the sample is primarily from photon irradiation and it is reasonable to assume that the structural transformations observed in this experiment is mainly related to photon irradiation instead of electron irradiation. In addition, only a very small fraction of the anatase nanoparticles has been exposed to this 300 $e^{-}/\text{Å}^{2} \cdot s$ electron fluence before in situ exposure to light and water vapor, as the diameter of electron beam is quite small (<50 nm at high magnifications). This allows checking of the structural changes in anatase particles that have not been imaged (or have not been exposed to electrons) before the *in situ* treatment, further verifying if the changes are due to light irradiation.

Figure 6.8ab display initial images of anatase nanoparticles before exposure to light and water vapor. The particle surfaces appear clean, bulk-terminated and crystalline. The center particle in **Figure 6.8a** is close to the [100] ZA, revealing that it is bounded mainly by the {101} and the {001} surfaces, which seems to be consistent with the calculated equilibrium shape of anatase presented in **Figure 1.3**. After 14 h *in situ* exposure to light and water vapor, an order-to-disorder transformation is observed on the surfaces of this particular particle as well as the two adjacent particles, as shown in **Figure 6.8c**. This transformation is expected as it has been observed using the Tecnai system, and is associated with hydroxylation of the oxide surface triggered by the presence of light induced oxygen vacancies on the surface (L. Zhang, Miller, and Crozier 2013). Interestingly, this image also reveals that the disordered phase on the {001} surface displays a layered structure, which was less apparent from the previous work using a non-aberration corrected microscope. This is because image delocalization was greatly suppressed due to the use of the aberration corrector, allowing improved resolution of the surfaces, as discussed in section 2.2.

Furthermore, **Figure 6.8b** shows another particle with a stepped {101} surface and a highly curved surface, both of which can be noted as vicinal surfaces. After *in situ* exposure to light and water, a disordered phase with varying thicknesses and contrasts is present on these surfaces, as indicated by the red and black arrows in **Figure 6.8d**. The disordered area pointed by the red arrows show larger thickness and enhanced contrast compared to the area pointed by the black arrow. This variance is observed when different defoci were selected, suggesting that it is not an imaging artifact but rather due to the different degrees of hydroxylation occurred on this particle surfaces. This heterogeneity in the hydroxylation degree may be related to the heterogeneity in the initial surface structures. In other words, surfaces initially containing higher concentration of steps or undercoordinated sites may result in higher degree of hydroxylation after exposing to light and water, possibly due to lower oxygen vacancy formation energies and lower activation energies for dissociative adsorption of water molecules at these sites. Further analysis needs to be conducted in order to testify this hypothesis.

6.4 Summary

The capability of exposing photocatalysts to light and water in a TEM is desired, as it allows direct observation of photocatalysts' dynamic responses to conditions relevant to photocatalytic water splitting. Water vapor can be introduced to the specimen region if an environmental TEM is employed. However, a method of introducing light illumination at the sample area is needed. An optical fiber based *in situ* light illumination system is thus designed and built for an aberration-corrected ETEM (FEI Titan) in this work. A broadband, micron sized light source with high radiance is employed. A specially designed fiber with a cut at the tip is used to guide light onto a tilted TEM sample and is inserted into the microscope through the objective aperture port. The fiber also needs to be bent to direct light to the desired angle. A fiber holder and an adapter are designed and fabricated to support the fragile fiber as well as maintaining its curvature. Apart from fulfilling the optical functionality which is having high intensity light striking at the sample area, this device also meets other design criteria such as no significant influence on the imaging and spectroscopy performances and the capability of introducing reactive gases to the sample region.

The spatial distribution of the light coming out from the fiber tip is measured and the size of the bright spot is much smaller than a TEM grid. Therefore, an alignment procedure is developed using a photosensor system in order to place the fiber at the optimum position with respect to the tilted TEM sample. Testing of the system shows an image motion is associated with significant changes of light intensity. Anatase nanoparticles are employed as a model photoactive material for studying structural changes upon *in situ* exposure to light and water vapor. An order-to-disorder transformation is observed on the nanoparticle surfaces, and the disordered surface phase displays a layered structure, which is associated with formation of hydroxyl species on oxide surfaces triggered by light induced oxygen vacancies.

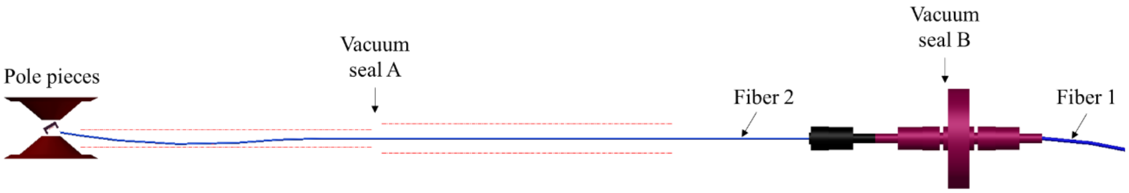

Figure 6.1: Geometric constraints of the objective aperture port, which are basically two bores (10 mm and 6 mm diameters) shown using the red dash-dotted lines. Light is directed from the light source to the sample area using fiber 1 and 2. Vacuum seals are made at point A and B so that fiber 2 and certain parts of the system are under the microscope high vacuum.

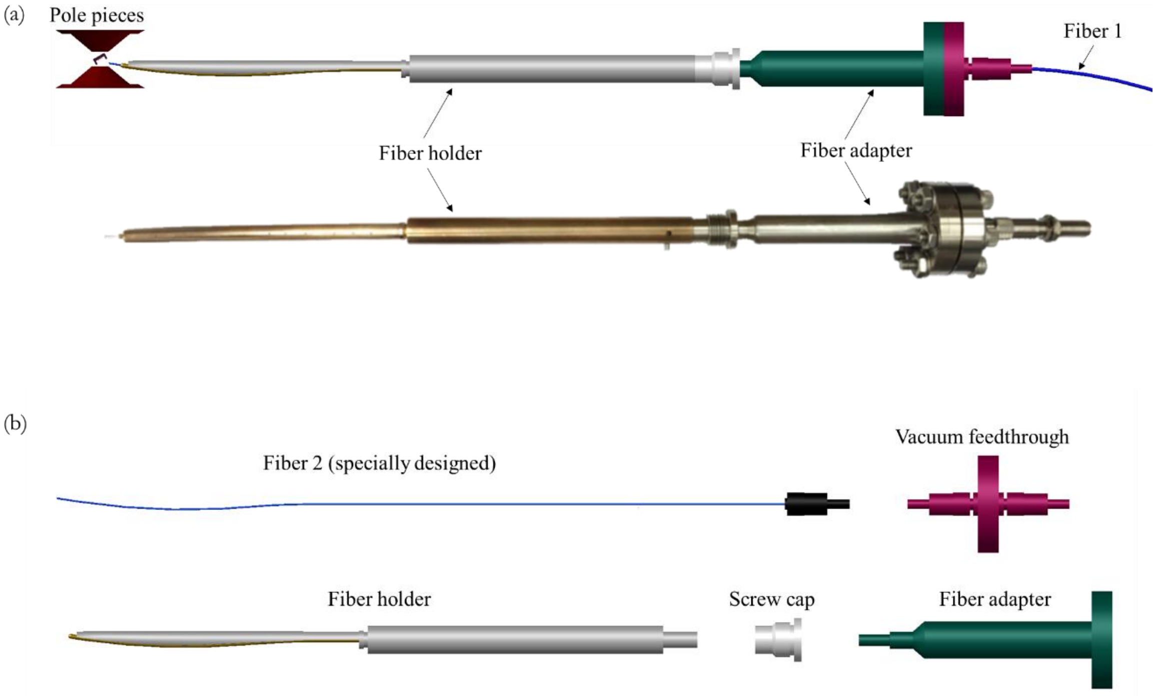

Figure 6.2: (a) A design drawing of the assembled device is compared with a picture of the fabricated device. (b) An exploded view drawing of the major components of this device.

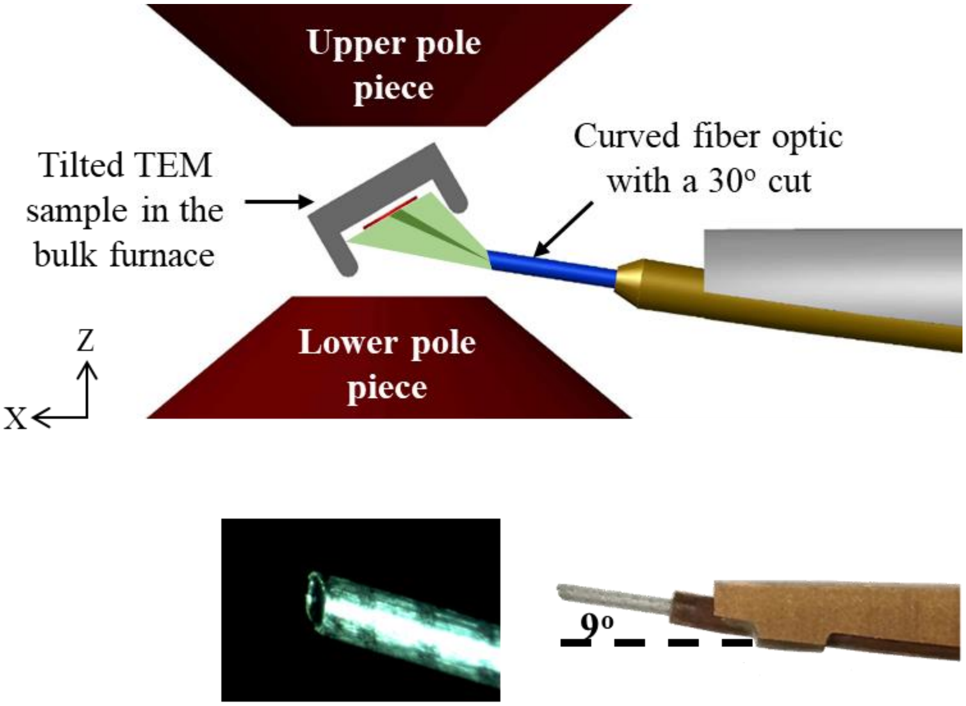

Figure 6.3: A zoom in design drawing focusing at the fiber tip region, showing high intensity light striking at the electron optical axis (also the center of the tilted sample grid) when fiber is at the optimum position. A picture of the fiber tip region of the fabricated device and an optical micrograph of the fiber tip showing the aluminum buffer are also displayed.

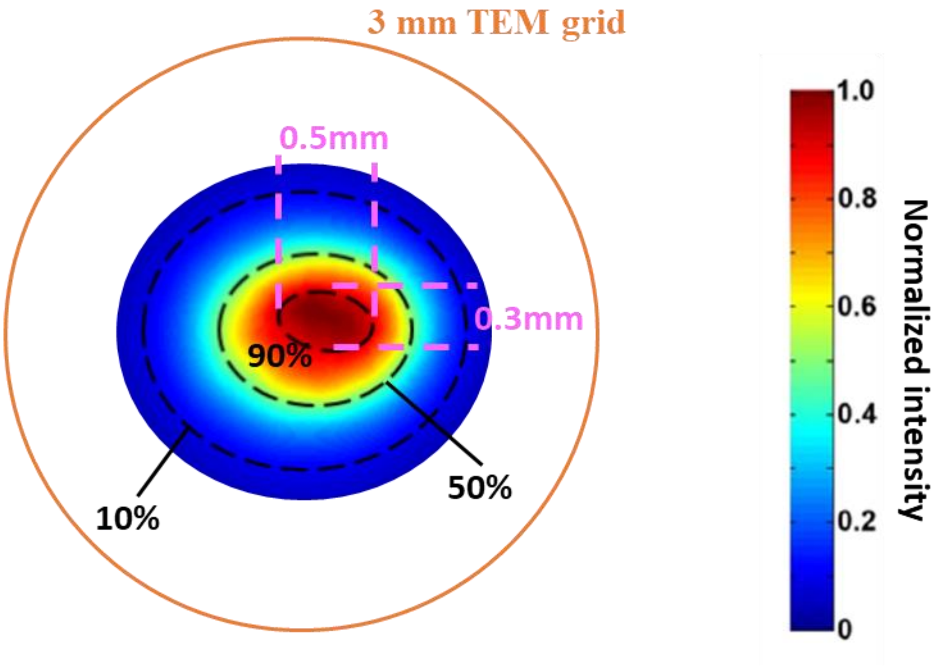

Figure 6.4: The measured spatial distribution of light intensity compared to the size of a TEM grid.

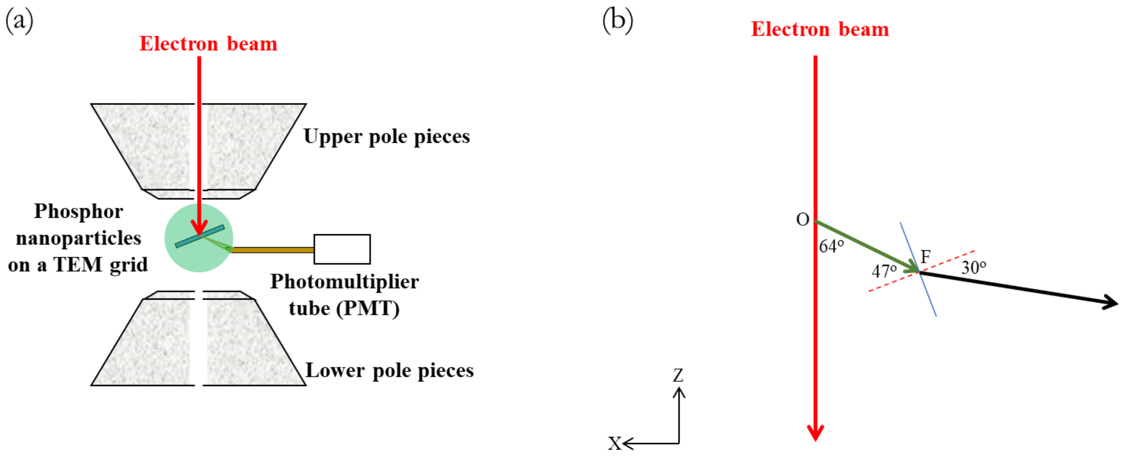

Figure 6.5: (a) A schematic showing the principle of the alignment procedure using a photosensor system. (b) Red arrow is electron beam trajectory. O represents the location of the phosphor particle or the center of the TEM grid. Blue line is the cross section of the fiber tip and the red dashed line is the perpendicular bisector. Green arrow and black arrow represent a light path where the emitted photons from O strikes at F and then travel along the center axis of fiber 2.

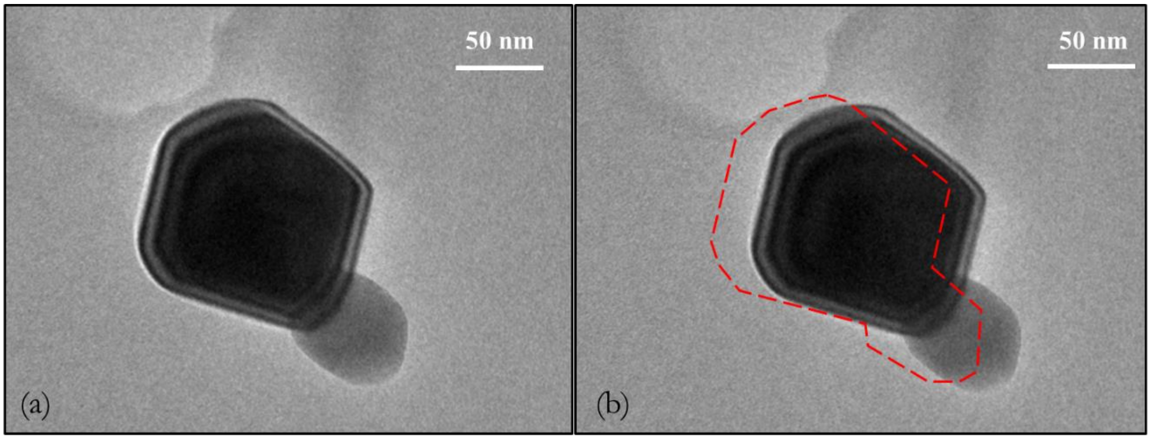

Figure 6.6: Images of the same commercial anatase cluster acquired when minimum light intensity (a) and maximum light intensity (b) is striking at the sample area. The red dashed curve in (b) outlines the exact cluster location in (a).

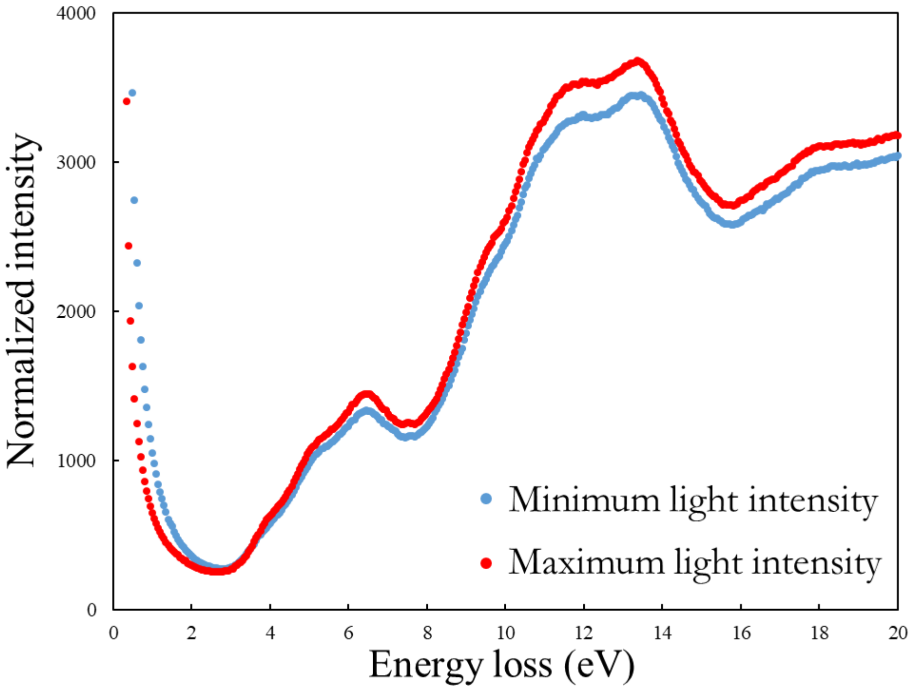

Figure 6.7: Transmission EEL spectra from commercial anatase particles acquired when maximum and minimum light intensity is striking at the sample area.

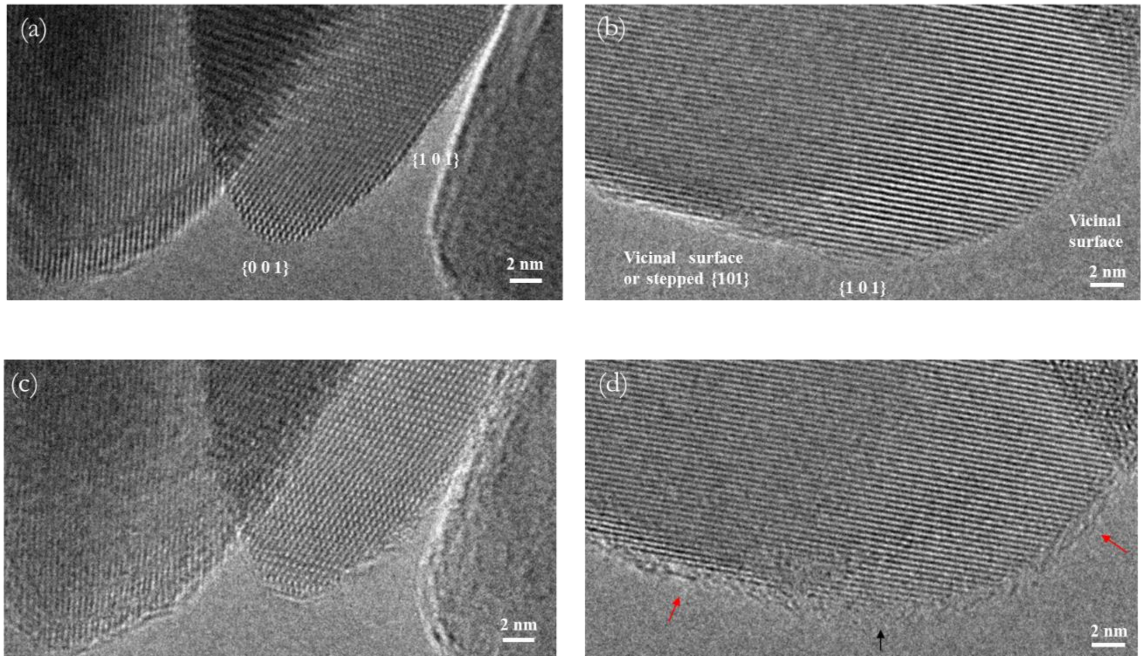

Figure 6.8: (a)(b) are initial images of anatase nanoparticles in vacuum before exposing to water vapor and light. (c)(d) are images of the same anatase nanoparticles after 14 h exposure of light and water vapor.

7 Conclusions and Future Work

7.1 Conclusions

In this work, various imaging and spectroscopy techniques have been applied or developed to characterize the atomic, electronic and optical structures of selected photocatalyst systems and model materials. High resolution imaging using an aberration-corrected TEM was applied to study the nano-level structure-reactivity relationships as well as the deactivation mechanisms of Ni-NiO co-catalysts loaded on Ta_2O_5 particles, which is an active UV photocatalyst system for overall water splitting. A series of Ni core-NiO shell co-catalysts with different morphologies were obtained by controlling the heat treatment condition during the synthesis process, which exhibit quite different photocatalytic reactivities. It was found that the presence of Ni metal phase is indispensable for the catalyst to be active, and an increase in the NiO shell thickness results in improved H_2 production, possibly due to suppression of the backward reaction. The optimum co-catalyst structure that gives the best reactivity appears to have a particle size of ~20 nm or larger with an oxide shell thickness percentage of 30-40%. In addition, a drop in H_2 production over reaction time was observed, which is related to structural transformations of these co-catalysts when exposed to liquid water and light. A loss of the Ni metal phase and formations of NiO nanoblocks or hollow NiO shells were found to be associated with catalyst deactivation, which is a photo-driven diffusion controlled process where Ni is probably oxidized or corroded away by oxidizing agents present during the reactions. It was proposed that Ni metal core is brought into contact with the oxidizing species due to the likely presence of micropores in the thermally synthesized NiO shells.

Apart from characterizing the atomic structures of photocatalysts, it is also desirable to locally probe the surface electronic structures of the photocatalysts, especially after they are exposed to water. Surface states associated with hydrate species on the surfaces of MgO nanocubes (a model system) were probed using aloof beam EELS, because it is surface sensitive and can suppress radiation damage significantly. Plateau shaped features before the bandgap onset were observed in the aloof beam EEL spectra. Simulations based on dielectric response theory revealed that the spectral features before the bandgap onset can be interpreted as signals induced by a surface hydrate layer less than 2 nm thick. This was supported by the observation made on the same sample using vibrational EELS, where a broad peak at 430 meV is detected, unambiguously revealing the presence of water species on the surface. To further investigate the energy position and width of the surface state associated with this surface layer, density of states modeling was performed to simulate the EEL spectrum and a broad occupied state located at 1.1 eV above the VB of MgO gives the best match. The FWHM of this bandgap state is 0.7 eV, suggesting the presence of a relatively high defect density and various forms of surface species, which was consistent with the simulation result using dielectric response theory and the vibrational EELS result.

Applying aloof beam EELS to commercial TiO_2 and Ta_2O_5 particles (which are typical light harvesting semiconductors used in photocatalysis) leads to excitation of cavity modes, due to their relatively large refractive index compared to MgO and relatively large particle sizes (~100-200 nm). This means if one needs to study surface states on these photocatalyst nanoparticles, it is preferable to employ particles which individually has a size smaller than 100 nm, or reduce the fast electron voltage to below 40 kV. The excitation of these geometry-specific optical-frequency resonant modes using fast electrons provides a novel way of studying light-particle interactions with high spatial resolution, since these geometric cavity resonances are encoded in the scattering properties of an oxide particle when it is exposed to either light or electron irradiation. CeO_2 nanocubes were employed as a model system to study the behaviors of these cavity modes because, compared to TiO_2, it has very similar refractive index but much more simpler geometry. Classical electrodynamics based spectral simulations were performed to interpret the experimentally observed spectral peaks within the bandgap region. It is concluded that the energy and strength of the cavity modes are affected by the size, geometry, dielectric function, and aggregations of the dielectric particles, as well as electron probe position and fast electron velocity.

Furthermore, since the atomic and electronic structures of photocatalyst nanoparticles are likely to undergo transformations upon exposure to reaction conditions, it is necessary to perform *in situ* studies to observe these structural changes. Therefore, a fiber optic based *in situ* light illumination system was designed, built and installed onto an aberration-corrected ETEM. A specially designed fiber with a 30^{o} cut at the tip is supported and bent by a fiber holder, and is inserted into the microscope chamber through the objective aperture port. The fiber was designed in a way that allows the bright spot of the light to irradiate the center of a tilted TEM sample. An alignment procedure using a photosensor system was developed to place the fiber at an optimum working position once it is installed. By exposing anatase nanoparticles to water vapor and high intensity broadband light, an order-to-disorder transformation was observed on the particle surfaces, which is caused by hydroxylation of the oxide surfaces triggered by formation of oxygen vacancies due to photon irradiation. Moreover, the disordered phase on the {001} anatase surface exhibit a layered structure. Based on previous studies, this hydroxylation related structural change only occurs when anatase is exposed to water and light simultaneously. Therefore, this observation implies the desired functionality of this *in situ* light illumination system is achieved.

7.2 Future Work

Further investigation on the reaction and deactivation mechanisms of core-shell co-catalysts

Many fundamental questions have not yet been answered when detailed reaction and deactivation mechanisms of core-shell structured co-catalysts (either Ni-NiO or noble metal-Cr_2O_3) are considered. As discussed in section 3.4.1, proton reduction is argued to take place at the buried surface of the metal core while water oxidation occurs at the surface of the oxide shell. This implies that, protons and the produced H_2 molecules can diffuse or migrate through the oxide shell suggesting the presence of micropores in the shell after the catalyst is prepared. These micropores are also argued to be the likely reason why the Ni-NiO system undergoes deactivation. It is hypothesized that the loss of Ni metal phase is caused by direct contact with oxidizing agents which also diffuse through the micropores in the shell. However, direct observation of the micropores have not been obtained, and methods that can prove the existence of the micropores still need to be developed.

In the noble metal-Cr_2O_3 system, the oxide shell is photodeposited onto the metal particle generating an amorphous oxide shell with nearly uniform thickness (Maeda, Teramura, Lu, Saito, et al. 2006). On the contrary, in the Ni-NiO system, the NiO shell is generated by partially oxidizing the Ni metal particles through thermal treatments, which results in a crystalline oxide shell with less uniform thickness and complicated morphology. It may be helpful to develop a third synthesis method of the oxide shell, for example, atomic layer deposition (ALD) which can produce pinhole-free, uniform oxide layer covering the surfaces of the metal particles as well as the light harvesting semiconductor particles (Johnson, Hultqvist, and Bent 2014). Testing the photocatalytic reactivity of catalysts with ALD produced oxide shell may give insights on the reaction and deactivation mechanisms of core-shell co-catalysts.

In situ probing of surface states and investigation on the sensitivity of aloof beam EELS

It would be interesting to develop an *in situ* aloof beam EELS technique to detect and follow the evolutions of surface electronic structures. MgO nanocube can be used as the model material and *in situ* exposure of MgO to water vapor is expected to result in surface hydroxylation. The degree of the hydroxylation, or the thickness of the surface hydrate layer can be controlled by varying the pressure of water vapor and the temperature of the heating holder. Aloof beam EELS can be performed on the initial MgO nanocubes and then on the gradually hydroxylated MgO. Spectral interpretation using the dielectric response theory and the DOS modeling developed in this work can be conducted to reveal how the energy and strength of the surface states evolve with increasing degree of hydroxylation.

In addition, insights into the sensitivity of aloof beam EELS may also be gained by conducting the above described experiment. The ultimate question is: could aloof beam EELS detect surface states induced by a monolayer of extrinsic species, dopants or defects on the surfaces of nanoparticles? If not, what is the minimum thickness/amount required? Simulations of a 0.1 nm surface layer of TiO_2 adsorbed on MgO bulk or a drude metal substrate have been performed, suggesting that higher sensitivity is obtained when the surface layer induced spectral features sit on a low background signal from the substrate, and when surface species with a large dielectric (especially the imaginary part) are involved (Crozier 2017). This sensitivity strongly depends on the detective quantum efficiency (DQE) of the EELS detector, since detectors with high DQE (e.g. direct electron detectors) are expected to show better signal-to-noise, which will allow subtle signals induced by thin surface layers to be observed.

Applying the in situ light illumination system to study photo-driven reactions

The *in situ* light illumination system built in this work can potentially be employed to a variety of material systems to observe structural transformations during various photo-driven chemical reactions. Photocorrosion, for example, is a process often taking place during photocatalytic water splitting and leads to deactivation of photocatalysts. It is thus important to learn the reaction steps/mechanisms involved in photocorrosion and the active sites in the materials where photocorrosion occurs more rapidly. *In situ* observations of the structural changes occurred when nanomaterials are exposed to conditions relevant to photocorrosion are thus desired. In many cases, exposing the TEM samples to liquid water rather than water vapor is desired. Therefore, methods need to be developed where the sample can be surrounded by a thin layer of liquid water, so that high resolution imaging can still be performed.

8 Appendix

8.1 Gas Chromatograms

As described in Chapter 3, the photo-reactor system was employed either in continuous flow or recirculation set up to measure the catalytic reactivities of various Ni-NiO/Ta_2O_5 photocatalysts. **Figure 8.1a** shows a typical gas chromatogram during a reactivity test focusing on H_2 production detection, where continuous flow set up was used and Ar was selected to be the carrier gas. Both peaks in this chromatogram correspond to H_2 gas, as the sample gas was split into two parallel PLOT columns in a GC Varian 450. Signal intensities of the first peak (left one) were measured for each chromatogram from the reactivity test, assuming a linear background model, which were then converted to H_2 production based on correction factors (discussed later). Plotting the signal intensities vs. reaction time for various photocatalysts generates **Figure 3.1a**.

The recirculation set up was also employed in order to obtain both O_2 and H_2 productions. In this case, He was used as the carrier gas and a GC Varian 3900 with one PLOT column was employed. A typical gas chromatogram acquired using this set up during a reactivity test is shown in **Figure 8.1b**. In addition, calibration run was conducted as described in section 2.1 to obtain the correction factors, and a typical chromatogram from the calibration run is also plotted in **Figure 8.1b**. Both chromatograms show three peaks corresponding to H_2, O_2 and N_2 from left to right. The presence of N_2 signal reveals the presence of air leak (N_2 peak intensity is smaller in the chromatogram in orange due to better gas seal in the photo-reactor system compared to that in the calibration run set up). This means that a portion of the O_2 signal detected by GC is from the air leak rather than water decomposition, which can be estimated based on the N_2 signal intensity. The remaining portion of the O_2 signal intensity which represents the evolved O_2 from water decomposition can then be calculated. As the amount of the evolved O_2 and H_2 are known in the calibration run, correction factors can be calculated and applied to obtain the O_2 and H_2 productions from the reactivity test generating **Figure 3.7**. It should be noted that the H_2 signal intensity is quite small in the chromatogram when He is used as the carrier gas, resulting in the noisier dataset of H_2 production in **Figure 3.7a**.

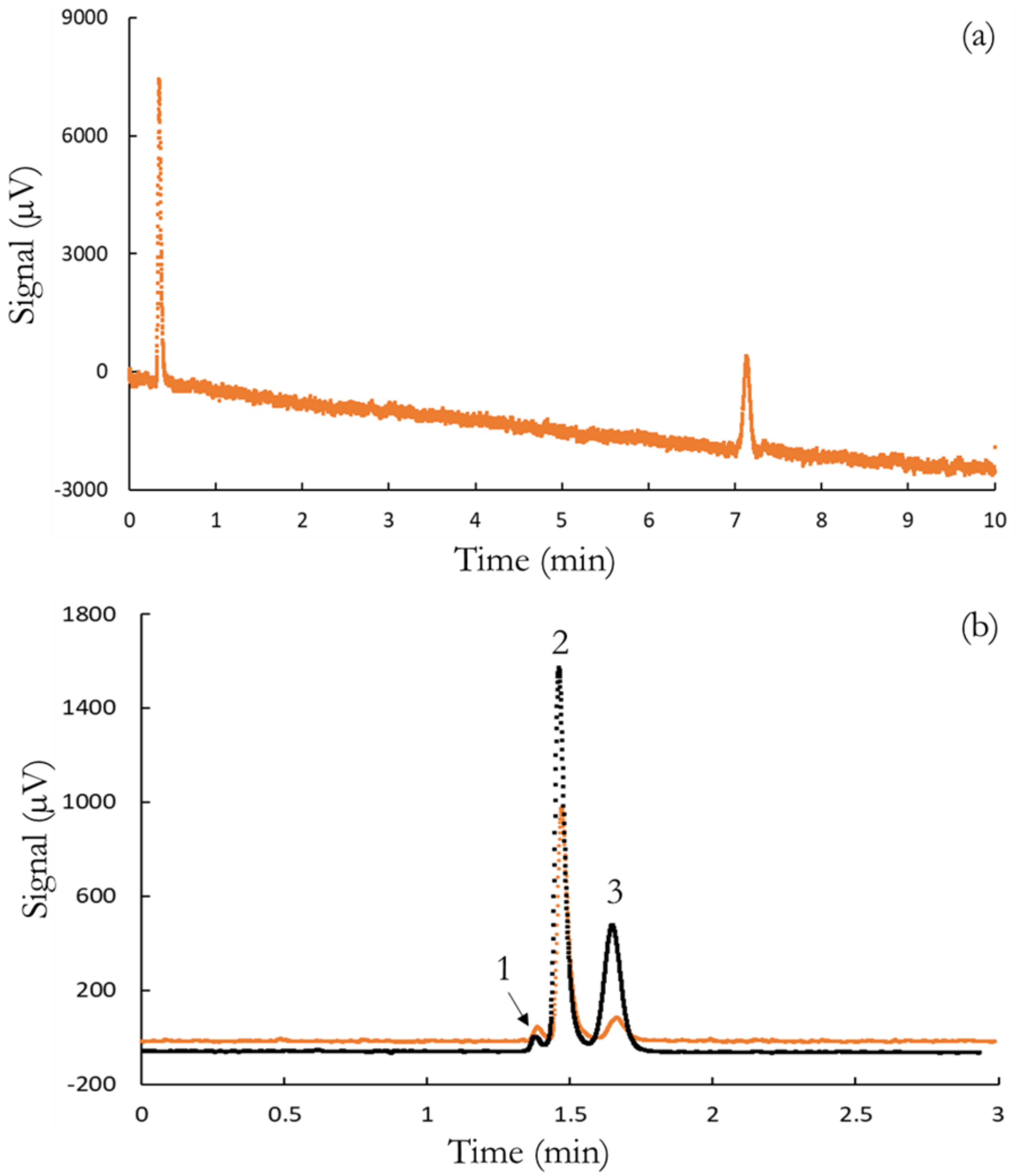

Figure 8.1: (a) A typical gas chromatogram acquired using GC Varian 450 with a parallel set up of 2 PLOT columns. Both peaks correspond to H_2 gas, generated during a reactivity test of ~0.09 g Ni-NiO/Ta_2O_5 photocatalyst where Ar was used as the carrier gas and the photoreactor system was employed in the continuous flow set up. (b) A typical gas chromatogram (orange) acquired using GC Varian 3900 with only one PLOT column, during a reactivity test of ~0.4 g Ni-NiO/Ta_2O_5 photocatalyst where He was used as the carrier gas and the photoreactor system was in the recirculation set up. The chromatogram in black was acquired using the same GC and the carrier gas, during a calibration run where electrolysis of water was conducted. Peak 1, 2 and 3 in each chromatogram corresponds to H_2, O_2 and N_2 respectively.

8.2 Images of Used Co-catalysts Structures

Typical examples of used or deactivated structures of Ni-NiO/Ta_2O_5 photocatalysts have been discussed in detail in section 3.3.3, and here several supplemental images are displayed. **Figure 8.2a** shows that after exposing sample (i) to liquid water and UV light, blocky shaped NiO nanoparticles (confirmed by FFT analysis) were found finely dispersed on the surface of Ta_2O_5. In addition, complicated NiO shells with a void in the center were observed from the deactivated sample (ii) and (iii), as shown in **Figure 8.2bc**. These NiO shells are polycrystalline and crystallographic defects can be observed as indicated by the red arrow. The grain boundaries as well as the defects present in these NiO shells (which may be viewed as micropores) may provide diffusion pathways to bring the Ni metal core into contact with oxidizing agent leading to deactivation of the co-catalysts, as discussed in section 3.4.2. Finally, apart from the NiO nanoblocks and the void-shells, another type of deactivated co-catalyst structure was found from sample (iv), where small crystalline nanodomains (indicated by the red arrows) embedded in a larger disordered particle cluster was observed (**Figure 8.2d**). The d-spacings derived based on FFT analysis from these crystalline nanodomains include ~2.7 Å, suggesting the presence of $Ni(OH)_2$ phase, which is in part consistent with the observation made by Han et al. (Han et al. 2017).

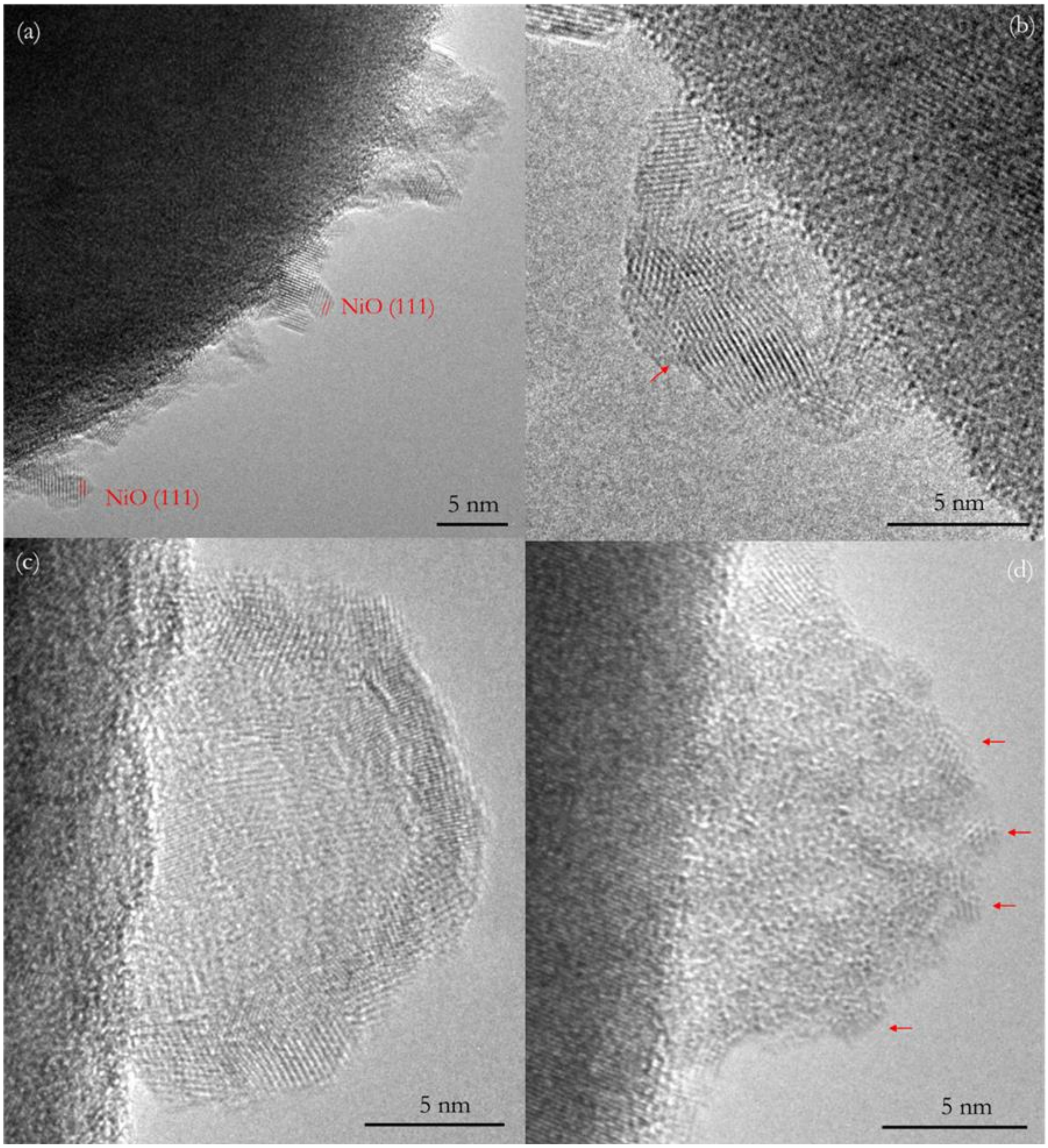

Figure 8.2: Images (a) – (d) show used co-catalyst structures of sample (i) – (iv) (defined in Table 3.1) respectively.

8.3 Dielectric Data

Dielectric data of MgO, CeO_2 and TiO_2 have been employed to conduct EELS spectral simulations, as shown in section 4.3.1 and Chapter 5. Here the complex dielectric function of these three materials are displayed in **Figure 8.3** and **Figure 8.4**. It should be noted that TiO_2 anatase shows polarization-dependent dielectric properties therefore two sets of complex dielectric functions (for ordinary and extraordinary polarizations) are associated with this material (**Figure 8.4ab**). In this study, an averaged dielectric function (**Figure 8.4c**) was calculated based on these two sets of data and was employed in the spectral simulation.

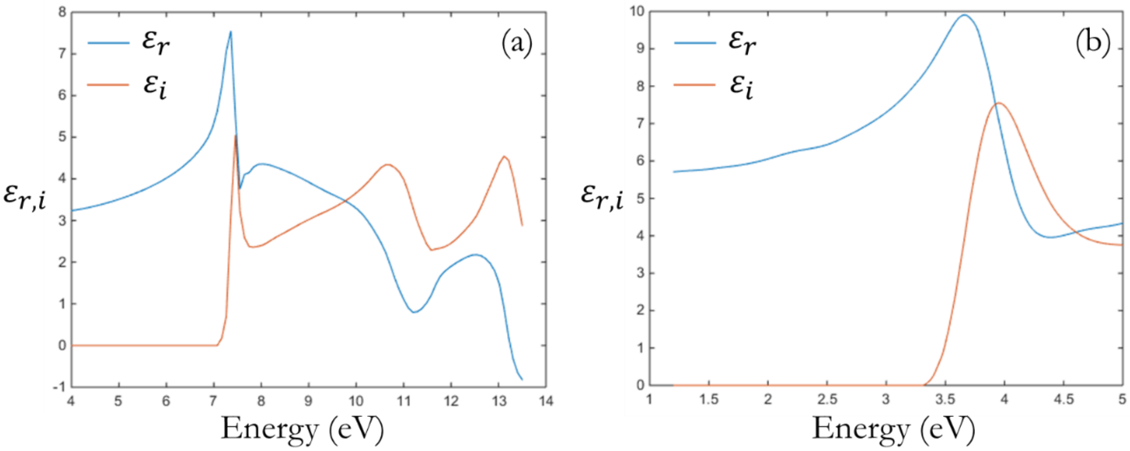

Figure 8.3: Real (ε_r) and imaginary (ε_i) parts of the complex dielectric function for (a) MgO and (b) CeO_2. Data were taken from (Roessler and Walker 1967; Järrendahl and Arwin 1998).

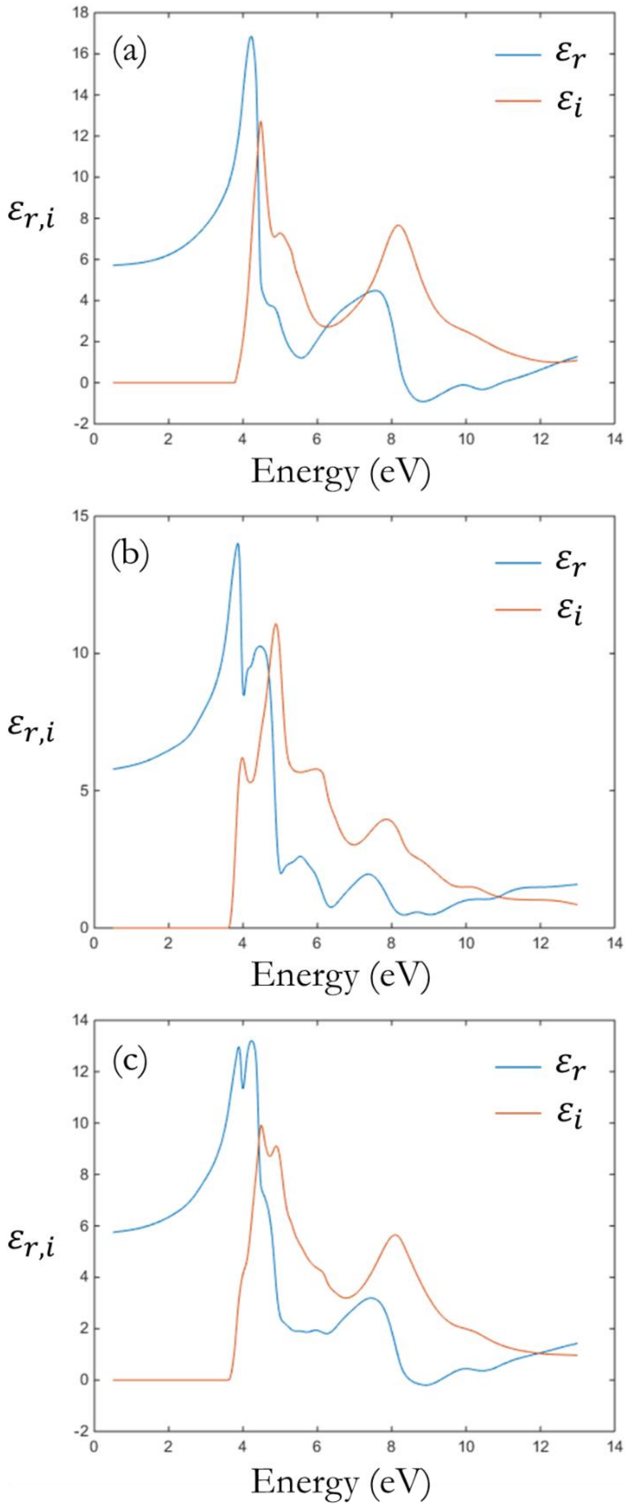

Figure 8.4: Polarization-dependent real (ε_r) and imaginary (ε_i) parts of the complex dielectric function for TiO_2 anatase: (a) is for E∥c (extraordinary polarization); (b) is for E⊥c (ordinary polarization); and (c) is the average of (a) and (b). Data were taken from (Landmann, Rauls, and Schmidt 2012).

8.4 Cavity Modes Induced Spectral Features from Ta_2O_5

As shown in **Figure 8.5**, when conducting an EELS line scan from vacuum onto a Ta_2O_5 particle with particle size in the range of hundreds of nanometers, a series of complicated peaks were observed before the bandgap onset of Ta_2O_5 (~4.1 eV), which is similar to the results obtained from TiO_2 shown in Chapter 5.

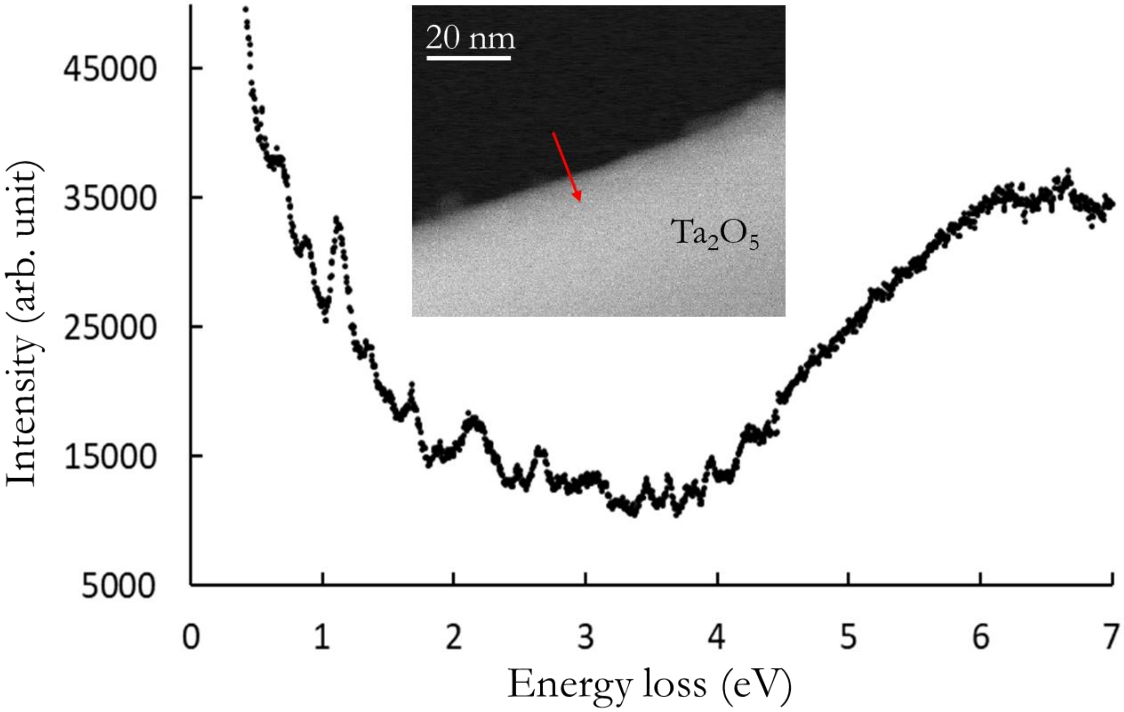

Figure 8.5: An EELS line scan was conducted at 60 kV from vacuum onto a Ta_2O_5 particle as shown in the inset. The summed spectrum from this line scan is plotted.

8.5 Design Details of the *In Situ* Light Illumination System

The table below summarizes the materials and parameters used for the major items involved in the *in situ* light illumination system. The original design of the fiber holder and fiber adapter is also displayed in the AutoCAD drawings below, with the important dimensions labeled. It should be noted that the drawing for the fiber holder only includes the main body without the copper tubing. The technicians at the mechanical instrument shop at ASU built these devices based on the original drawings with minor modifications.

Table 8.1: Item list for the *in situ* light illumination system.

Item	Materials	Description
Fiber 1	Silica, polymer, stainless steel ferrule	Ordered from Ocean Optics 600 μm, solarization-resistant (SR) 2 m, SMA-905
Fiber 2	Silica, aluminum, epoxy, stainless steel ferrule	Specially ordered from Ocean Optics 600 μm, Al buffered, UV/SR 268.55 mm SMA-905 to 30° cut
Fiber holder	Phosphor bronze, Ag soldering, Cu tubing	Fabricated at the mechanical instrument shop at ASU
Fiber adapter	Stainless steel	
Screw cap		
Rotatable flange		Ordered from mechanical instrument shop at ASU 1.33 CF
Vacuum feedthrough	Stainless steel, silica	Ordered from Ocean Optics 600 μm 1.33 CF flange, XSR
O-rings	Viton	One at vacuum seal A (i.e. the groove with Ø5.3 on the fiber holder); One at the step near M4 on the fiber adapter
Cu gasket	Cu	To make a vacuum seal between the 1.33 CF rotatable flange and the vacuum feedthrough

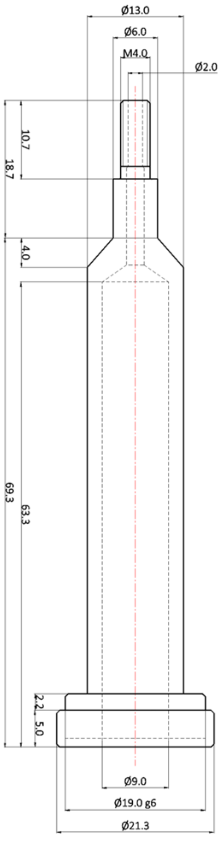

Fiber adapter

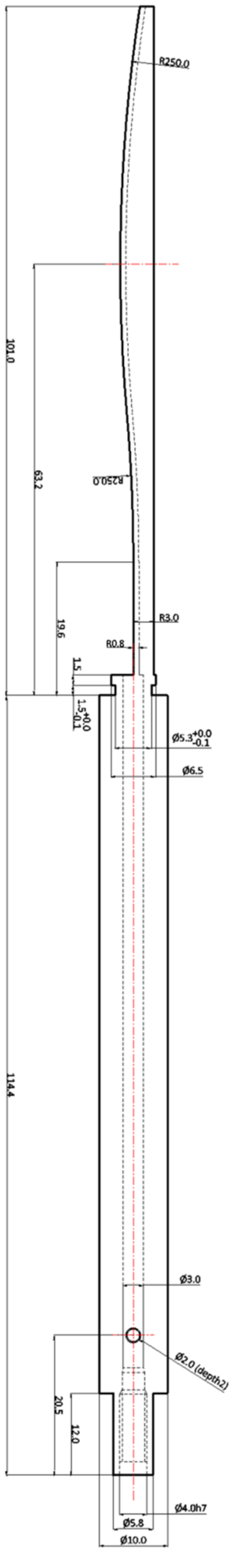

Fiber holder

References

Abe, Hiroyuki, Hiroki Kurata, and Kiichi Hojou. 2000. "Spatially Resolved Electron Energy-Loss Spectroscopy of the Surface Excitations on the Insulating Fine Particle of Aluminum Oxide." *Journal of the Physical Society of Japan* 69 (5):1553–1557.

Alexander, Duncan T. L., Peter A. Crozier, and James R. Anderson. 2008. "Brown Carbon Spheres in East Asian Outflow and Their Optical Properties." *Science* 321 (5890):833–36. https://doi.org/10.1126/science.1155296.

Al-Gaashani, R., S. Radiman, Y. Al-Douri, N. Tabet, and A. R. Daud. 2012. "Investigation of the Optical Properties of Mg(OH)2 and MgO Nanostructures Obtained by Microwave-Assisted Methods." *Journal of Alloys and Compounds* 521 (April):71–76. https://doi.org/10.1016/j.jallcom.2012.01.045.

A. Pinaud, Blaise, Jesse D. Benck, Linsey C. Seitz, Arnold J. Forman, Zhebo Chen, Todd G. Deutsch, Brian D. James, et al. 2013. "Technical and Economic Feasibility of Centralized Facilities for Solar Hydrogen Production via Photocatalysis and Photoelectrochemistry." *Energy & Environmental Science* 6 (7):1983–2002. https://doi.org/10.1039/C3EE40831K.

Archer, Mary D., and James R. Bolton. 1990. "Requirements for Ideal Performance of Photochemical and Photovoltaic Solar Energy Converters." *Journal of Physical Chemistry* 94 (21):8028–8036.

Arrouvel, C., M. Digne, M. Breysse, H. Toulhoat, and P. Raybaud. 2004. "Effects of Morphology on Surface Hydroxyl Concentration: A DFT Comparison of Anatase–TiO2 and γ-Alumina Catalytic Supports." *Journal of Catalysis* 222 (1):152–66. https://doi.org/10.1016/j.jcat.2003.10.016.

Arslan, Ilke, Jerome K. Hyun, Rolf Erni, Michael N. Fairchild, Stephen D. Hersee, and David A. Muller. 2009. "Using Electrons As a High-Resolution Probe of Optical Modes in Individual Nanowires." *Nano Letters* 9 (12):4073–77. https://doi.org/10.1021/nl902266n.

Atkinson, A., D. P. Moon, D. W. Smart, and R. I. Taylor. 1986. "Tracer Diffusion Studies in NiO Bicrystals and Polycrystals." *Journal of Materials Science* 21 (5):1747–57. https://doi.org/10.1007/BF01114735.

Atkinson, A., and R. I. Taylor. 1978. "The Self-Diffusion of Ni in NiO and Its Relevance to the Oxidation of Ni." *Journal of Materials Science* 13 (2):427–32. https://doi.org/10.1007/BF00647789.

Bahnemann, Detlef W., Marcus Hilgendorff, and Ruediger Memming. 1997. "Charge Carrier Dynamics at TiO2 Particles: Reactivity of Free and Trapped Holes." *The Journal of Physical Chemistry B* 101 (21):4265–4275.

Bard, Allen J. 1979. "Photoelectrochemistry and Heterogeneous Photo-Catalysis at Semiconductors." *Journal of Photochemistry* 10 (1):59–75. https://doi.org/10.1016/0047-2670(79)80037-4.

Bard, Allen J., and Marye Anne Fox. 1995. "Artificial Photosynthesis: Solar Splitting of Water to Hydrogen and Oxygen." *Accounts of Chemical Research* 28 (3):141–145.

Batson, P. E. 1983. "Surface Plasmon Scattering on Flat Surfaces at Grazing Incidence." *Ultramicroscopy* 11 (4):299–302.

Batson, P. E., N. Dellby, and O. L. Krivanek. 2002. "Sub-Angstrom Resolution Using Aberration Corrected Electron Optics." *Nature; London* 418 (6898):617–20. https://doi.org/http://dx.doi.org.ezproxy1.lib.asu.edu/10.1038/nature00972.

Batson, P.E. 1982. "New Surface Plasmon Resonance in Clusters of Small Aluminum Spheres." *Ultramicroscopy* 9 (3):277–82. https://doi.org/10.1016/0304-3991(82)90212-1.

Beiter, Philipp. 2015. "2014 Renewable Energy Data Book." NREL (National Renewable Energy Laboratory (NREL). http://www.osti.gov/scitech/biblio/1226242.

Benthem, K. van, C. Elsässer, and R. H. French. 2001. "Bulk Electronic Structure of SrTiO3: Experiment and Theory." *Journal of Applied Physics* 90 (12):6156–64. https://doi.org/10.1063/1.1415766.

Bigelow, Nicholas W., Alex Vaschillo, Vighter Iberi, Jon P. Camden, and David J. Masiello. 2012. "Characterization of the Electron- and Photon-Driven Plasmonic Excitations of Metal Nanorods." *ACS Nano* 6 (8):7497–7504. https://doi.org/10.1021/nn302980u.

Blankenship, Robert E., David M. Tiede, James Barber, Gary W. Brudvig, Graham Fleming, Maria Ghirardi, M. R. Gunner, et al. 2011. "Comparing Photosynthetic and Photovoltaic Efficiencies and Recognizing the Potential for Improvement." *Science* 332 (6031):805–9. https://doi.org/10.1126/science.1200165.

Bohren, Craig F., and Donald R. Huffman. 2008. *Absorption and Scattering of Light by Small Particles*. John Wiley & Sons.

Bolton, James R., Stewart J. Strickler, and John S. Connolly. 1985. "Limiting and Realizable Efficiencies of Solar Photolysis of Water." *Nature* 316 (6028):495–500. https://doi.org/10.1038/316495a0.

Bourikas, Kyriakos, Christos Kordulis, and Alexis Lycourghiotis. 2014. "Titanium Dioxide (Anatase and Rutile): Surface Chemistry, Liquid–Solid Interface Chemistry, and Scientific Synthesis of Supported Catalysts." *Chemical Reviews* 114 (19):9754–9823. https://doi.org/10.1021/cr300230q.

Bowman, W.J., K. March, C.A. Hernandez, and P.A. Crozier. 2016. “Measuring Bandgap States in Individual Non-Stoichiometric Oxide Nanoparticles Using Monochromated STEM EELS: The Praseodymium–ceria Case.” *Ultramicroscopy* 167 (August):5–10. https://doi.org/10.1016/j.ultramic.2016.04.009.

Brause, M., S. Skordas, and V. Kempter. 2000. “Study of the Electronic Structure of TiO2(110) and Cs/TiO2(110) with Metastable Impact Electron Spectroscopy and Ultraviolet Photoemission Spectroscopy (HeI).” *Surface Science* 445 (2–3):224–34. https://doi.org/10.1016/S0039-6028(99)01052-3.

Bredow, Thomas, and Andrea R. Gerson. 2000. “Effect of Exchange and Correlation on Bulk Properties of MgO, NiO, and CoO.” *Physical Review B* 61 (8):5194.

Butler, E. P., and K. F. Hale. 1981. “Dynamic Experiments in the Electron Microscope.” http://inis.iaea.org/Search/search.aspx?orig_q=RN:13651885.

Caspary Toroker, Maytal, Dalal K. Kanan, Nima Alidoust, Leah Y. Isseroff, Peilin Liao, and Emily A. Carter. 2011. “First Principles Scheme to Evaluate Band Edge Positions in Potential Transition Metal Oxide Photocatalysts and Photoelectrodes.” *Physical Chemistry Chemical Physics* 13 (37):16644–54. https://doi.org/10.1039/C1CP22128K.

Cavalca, F., A. B. Laursen, B. E. Kardynal, R. E. Dunin-Borkowski, S. Dahl, J. B. Wagner, and T. W. Hansen. 2012. “In Situ Transmission Electron Microscopy of Light-Induced Photocatalytic Reactions.” *Nanotechnology* 23 (7):075705. https://doi.org/10.1088/0957-4484/23/7/075705.

Chen, Shiyou, and Lin-Wang Wang. 2012. “Thermodynamic Oxidation and Reduction Potentials of Photocatalytic Semiconductors in Aqueous Solution.” *Chemistry of Materials* 24 (18):3659–66. https://doi.org/10.1021/cm302533s.

Chen, Xiaobo, Shaohua Shen, Liejin Guo, and Samuel S. Mao. 2010. “Semiconductor-Based Photocatalytic Hydrogen Generation.” *Chemical Reviews* 110 (11):6503–70. https://doi.org/10.1021/cr1001645.

Chenna, Santhosh, and Peter A. Crozier. 2012. “In Situ Environmental Transmission Electron Microscopy to Determine Transformation Pathways in Supported Ni Nanoparticles.” *Micron*, In situ TEM, 43 (11):1188–94. https://doi.org/10.1016/j.micron.2012.04.007.

Chun, Wang-Jae, Akio Ishikawa, Hideki Fujisawa, Tsuyoshi Takata, Junko N. Kondo, Michikazu Hara, Maki Kawai, Yasumichi Matsumoto, and Kazunari Domen. 2003. “Conduction and Valence Band Positions of Ta2O5, TaON, and Ta3N5 by UPS and Electrochemical Methods.” *The Journal of Physical Chemistry B* 107 (8):1798–1803. https://doi.org/10.1021/jp027593f.

Compton, Owen C., Cory H. Mullet, Shirley Chiang, and Frank E. Osterloh. 2008. “A Building Block Approach to Photochemical Water-Splitting Catalysts Based on Layered

Niobate Nanosheets." *The Journal of Physical Chemistry C* 112 (15):6202–8. https://doi.org/10.1021/jp711589z.

Cook, John, Dana Nuccitelli, Sarah A. Green, Mark Richardson, Bärbel Winkler, Rob Painting, Robert Way, Peter Jacobs, and Andrew Skuce. 2013. "Quantifying the Consensus on Anthropogenic Global Warming in the Scientific Literature." *Environmental Research Letters* 8 (2):024024. https://doi.org/10.1088/1748-9326/8/2/024024.

Cowley, J. M. 1982a. "Energy Losses of Fast Electrons at Crystal Surfaces." *Physical Review B* 25 (2):1401.

———. 1982b. "Surface Energies and Surface Structure of Small Crystals Studied by Use of a Stem Instrument." *Surface Science* 114 (2):587–606. https://doi.org/10.1016/0039-6028(82)90707-5.

Crabtree, George W., Mildred S. Dresselhaus, and Michelle V. Buchanan. 2004. "The Hydrogen Economy." *Physics Today* 57 (12):39–44.

Creemer, J.F., S. Helveg, G.H. Hoveling, S. Ullmann, A.M. Molenbroek, P.M. Sarro, and H.W. Zandbergen. 2008. "Atomic-Scale Electron Microscopy at Ambient Pressure." *Ultramicroscopy* 108 (9):993–98. https://doi.org/10.1016/j.ultramic.2008.04.014.

Crozier, Peter A. 2017. "Vibrational and Valence Aloof Beam EELS: A Potential Tool for Nondestructive Characterization of Nanoparticle Surfaces." *Ultramicroscopy* 180 (September):104–14. https://doi.org/10.1016/j.ultramic.2017.03.011.

Crozier, Peter A., Toshihiro Aoki, and Qianlang Liu. 2016. "Detection of Water and Its Derivatives on Individual Nanoparticles Using Vibrational Electron Energy-Loss Spectroscopy." *Ultramicroscopy* 169 (October):30–36. https://doi.org/10.1016/j.ultramic.2016.06.008.

Crozier, Peter A., and Santhosh Chenna. 2011. "In Situ Analysis of Gas Composition by Electron Energy-Loss Spectroscopy for Environmental Transmission Electron Microscopy." *Ultramicroscopy* 111 (3):177–85. https://doi.org/10.1016/j.ultramic.2010.11.005.

Crozier, Peter A., and Benjamin K. Miller. 2016. "Spectroscopy of Solids, Gases, and Liquids in the ETEM." In *Controlled Atmosphere Transmission Electron Microscopy*, 95–141. Springer, Cham. https://doi.org/10.1007/978-3-319-22988-1_4.

Czekalla, Christian, Thomas Nobis, Andreas Rahm, Bingqiang Cao, Jesús Zúñiga-Pérez, Chris Sturm, Rüdiger Schmidt-Grund, Michael Lorenz, and Marius Grundmann. 2010. "Whispering Gallery Modes in Zinc Oxide Micro- and Nanowires." *Physica Status Solidi (B)* 247 (6):1282–93. https://doi.org/10.1002/pssb.200945527.

Davison, S. G., and J. D. Levine. 1970. "Surface States." *Solid State Physics - Advances in Research and Applications* 25 (C):1–149. https://doi.org/10.1016/S0081-1947(08)60008-9.

Deng, Qixin, Mingdeng Wei, Zhensheng Hong, Xiaokun Ding, Lilong Jiang, and Kemei Wei. 2010. "Selective Synthesis of Rutile, Anatase, and Brookite Nanorods by a Hydrothermal Route." *Current Nanoscience* 6 (5):479–82. https://doi.org/10.2174/157341310797574970.

Diebold, Ulrike. 2003. "The Surface Science of Titanium Dioxide." *Surface Science Reports* 48 (5–8):53–229. https://doi.org/10.1016/S0167-5729(02)00100-0.

Domen, Kazunari, Akihiko Kudo, and Takaharu Onishi. 1986. "Mechanism of Photocatalytic Decomposition of Water into H2 and O2 over NiO SrTiO3." *Journal of Catalysis* 102 (1):92–98. https://doi.org/10.1016/0021-9517(86)90143-0.

Domen, Kazunari, Akihiko Kudo, Takaharu Onishi, Nobuhiro Kosugi, and Haruo Kuroda. 1986. "Photocatalytic Decomposition of Water into Hydrogen and Oxygen over Nickel(II) Oxide-Strontium Titanate (SrTiO3) Powder. 1. Structure of the Catalysts." *The Journal of Physical Chemistry* 90 (2):292–95. https://doi.org/10.1021/j100274a018.

Domen, Kazunari, Shuichi Naito, Takaharu Onishi, Kenzi Tamaru, and Mitsuyuki Soma. 1982. "Study of the Photocatalytic Decomposition of Water Vapor over a Nickel(II) Oxide-Strontium Titanate (SrTiO3) Catalyst." *The Journal of Physical Chemistry* 86 (18):3657–61. https://doi.org/10.1021/j100215a032.

Domen, Kazunari, Shuichi Naito, Mitsuyuki Soma, Takaharu Onishi, and Kenzi Tamaru. 1980. "Photocatalytic Decomposition of Water Vapour on an NiO–SrTiO 3 Catalyst." *Journal of the Chemical Society, Chemical Communications*, no. 12:543–544.

Doole, R. C., G. M. Parkinson, and J. M. Stead. 1991. "High Resolution Gas Reaction Cell for the JEM 4000." In *Institute of Physics Conference Series*, 119:157–160.

Draine, Bruce T., and Piotr J. Flatau. 1994. "Discrete-Dipole Approximation For Scattering Calculations." *JOSA A* 11 (4):1491–99. https://doi.org/10.1364/JOSAA.11.001491.

Dresselhaus, M. S., and I. L. Thomas. 2001. "Alternative Energy Technologies." *Nature* 414 (6861):332–37. https://doi.org/10.1038/35104599.

Duonghong, Dung, and Michael Grätzel. 1984. "Colloidal TiO 2 Particles as Oxygen Carriers in Photochemical Water Cleavage Systems." *Journal of the Chemical Society, Chemical Communications* 0 (23):1597–99. https://doi.org/10.1039/C39840001597.

Egashira, Makoto, Shohachi Kawasumi, Shuichi Kagawa, and Tetsuro Seiyama. 1978. "Temperature Programmed Desorption Study of Water Adsorbed on Metal Oxides. I. Anatase and Rutile." *Bulletin of the Chemical Society of Japan* 51 (11):3144–49. https://doi.org/10.1246/bcsj.51.3144.

Egerton, Ray. 2011. *Electron Energy-Loss Spectroscopy in the Electron Microscope*. 3rd ed. Springer Science & Business Media.

Egerton, Raymond F., Feng Wang, and Peter A. Crozier. 2006. “Beam-Induced Damage to Thin Specimens in an Intense Electron Probe.” *Microscopy and Microanalysis* 12 (01):65–71. https://doi.org/10.1017/S1431927606060065.

Egerton, R.F. 2011. *Electron Energy-Loss Spectroscopy in the Electron Microscope*. Boston, MA: Springer US. http://link.springer.com/10.1007/978-1-4419-9583-4.

———. 2012. “Mechanisms of Radiation Damage in Beam-Sensitive Specimens, for TEM Accelerating Voltages between 10 and 300 KV.” *Microscopy Research and Technique* 75 (11):1550–56. https://doi.org/10.1002/jemt.22099.

———. 2013. “Control of Radiation Damage in the TEM.” *Ultramicroscopy* 127 (April):100–108. https://doi.org/10.1016/j.ultramic.2012.07.006.

“EIA - Annual Energy Outlook 2017.” Accessed March 24, 2017. https://www.eia.gov/outlooks/aeo/.

E. Osterloh, Frank. 2013. “Inorganic Nanostructures for Photoelectrochemical and Photocatalytic Water Splitting.” *Chemical Society Reviews* 42 (6):2294–2320. https://doi.org/10.1039/C2CS35266D.

Erni, Rolf, and Browning, Nigel 2008. "The impact of surface and retardation losses on valence electron energy-loss spectroscopy." *Ultramicroscopy* 108 (2) 84 10.1016/j.ultramic.2007.03.005.

Erni, Rolf. 2015. *Aberration-Corrected Imaging in Transmission Electron Microscopy: An Introduction Second Edition*. World Scientific Publishing Company.

Finazzi, Emanuele, Cristiana Di Valentin, Gianfranco Pacchioni, and Annabella Selloni. 2008. “Excess Electron States in Reduced Bulk Anatase TiO2: Comparison of Standard GGA, GGA+U, and Hybrid DFT Calculations.” *The Journal of Chemical Physics* 129 (15):154113. https://doi.org/10.1063/1.2996362.

Findlay, S. D., N. Shibata, H. Sawada, E. Okunishi, Y. Kondo, T. Yamamoto, and Y. Ikuhara. 2009. “Robust Atomic Resolution Imaging of Light Elements Using Scanning Transmission Electron Microscopy.” *Applied Physics Letters* 95 (19):191913. https://doi.org/10.1063/1.3265946.

Fox, Marye Anne., and Maria T. Dulay. 1993. “Heterogeneous Photocatalysis.” *Chemical Reviews* 93 (1):341–57. https://doi.org/10.1021/cr00017a016.

Fujishima, Akira, and Kenichi Honda. 1971. “Electrochemical Evidence for the Mechanism of the Primary Stage of Photosynthesis.” *Bulletin of the Chemical Society of Japan* 44 (4):1148–50. https://doi.org/10.1246/bcsj.44.1148.

———. 1972. “Electrochemical Photolysis of Water at a Semiconductor Electrode.” *Nature* 238 (5358):37–38. https://doi.org/10.1038/238037a0.

Fujishima, Akira, Xintong Zhang, and Donald A. Tryk. 2008. "TiO2 Photocatalysis and Related Surface Phenomena." *Surface Science Reports* 63 (12):515–82. https://doi.org/10.1016/j.surfrep.2008.10.001.

García de Abajo, F. J. 1999. "Relativistic Energy Loss and Induced Photon Emission in the Interaction of a Dielectric Sphere with an External Electron Beam." *Physical Review B* 59 (4):3095–3107. https://doi.org/10.1103/PhysRevB.59.3095.

———. 2010. "Optical Excitations in Electron Microscopy." *Reviews of Modern Physics* 82 (1):209–75. https://doi.org/10.1103/RevModPhys.82.209.

Gaye, Amie, and others. 2007. "Access to Energy and Human Development." *Human Development Report* 2008. https://pdfs.semanticscholar.org/97f6/9c15a5b4188a9f687492851fa556bee2cb30.pdf.

Gerischer, H. 1990. "The Impact of Semiconductors on the Concepts of Electrochemistry." *Electrochimica Acta* 35 (11–12):1677–99. https://doi.org/10.1016/0013-4686(90)87067-C.

Geuquet, Nicolas, and Luc Henrard. 2010. "EELS and Optical Response of a Noble Metal Nanoparticle in the Frame of a Discrete Dipole Approximation." *Ultramicroscopy*, PROCEEDINGS OF THE INTERNATIONAL WORKSHOP ON ENHANCED DATA GENERATED BY ELECTRONS, 110 (8):1075–80. https://doi.org/10.1016/j.ultramic.2010.01.013.

Gibson, Andrew, Roger Haydock, and John P. LaFemina. 1992. "Electronic Structure and Relative Stability of the MgO (001) and (111) Surfaces." *Journal of Vacuum Science & Technology A* 10 (4):2361–66. https://doi.org/10.1116/1.577965.

Ginzburg, V. L. 2005. "Radiation from Uniformly Moving Sources (Vavilov-Cherenkov Effect, Transition Radiation, and Some Other Phenomena)." *Acoustical Physics* 51 (1):11–23. https://doi.org/10.1134/1.1851624.

Gong, Xue-Qing, and Annabella Selloni. 2005. "Reactivity of Anatase TiO2 Nanoparticles: The Role of the Minority (001) Surface." *The Journal of Physical Chemistry B* 109 (42):19560–62. https://doi.org/10.1021/jp055311g.

Gong, Xue-Qing, Annabella Selloni, Matthias Batzill, and Ulrike Diebold. 2006. "Steps on Anatase TiO2(101)." *Nature Materials* 5 (8):665–70. https://doi.org/10.1038/nmat1695.

Graetzel, Michael. 1981. "Artificial Photosynthesis: Water Cleavage into Hydrogen and Oxygen by Visible Light." *Accounts of Chemical Research* 14 (12):376–384.

Grob, Robert L., and Eugene F. Barry. 2004. *Modern Practice of Gas Chromatography*. John Wiley & Sons.

Hagfeldt, Anders, and Michael Graetzel. 1995. "Light-Induced Redox Reactions in Nanocrystalline Systems." *Chemical Reviews* 95 (1):49–68.

Haider, M., G. Braunshausen, and E. Schwan. 1995. "Correction of the Spherical Aberration of a 200 KV TEM by Means of a Hexapole-Corrector." *Optik* 99 (4):167–79.

Haider, Max, Harald Rose, Stephan Uhlemann, Eugen Schwan, Bernd Kabius, and Knut Urban. 1998. "A Spherical-Aberration-Corrected 200 KV Transmission Electron Microscope." *Ultramicroscopy* 75 (1):53–60. https://doi.org/10.1016/S0304-3991(98)00048-5.

Han, Kai, Tomas Kreuger, Bastian Mei, and Guido Mul. 2017. "Transient Behavior of Ni@NiOx Functionalized SrTiO3 in Overall Water Splitting." *ACS Catalysis* 7 (3):1610–14. https://doi.org/10.1021/acscatal.6b03662.

Hanaor, Dorian A. H., and Charles C. Sorrell. 2011. "Review of the Anatase to Rutile Phase Transformation." *Journal of Materials Science* 46 (4):855–74. https://doi.org/10.1007/s10853-010-5113-0.

Hansen, K. K. 2008. "Electrochemical Reduction of O2 and NO on Ni, Pt and Au." *Journal of Applied Electrochemistry* 38 (5):591–95. https://doi.org/10.1007/s10800-007-9476-0.

Hansen, T. W., J. B. Wagner, and R. E. Dunin-Borkowski. 2010. "Aberration Corrected and Monochromated Environmental Transmission Electron Microscopy: Challenges and Prospects for Materials Science." *Materials Science and Technology* 26 (11):1338–44. https://doi.org/10.1179/026708310X12756557336355.

Hansen, Thomas W., and Jakob B. Wagner. 2012. "Environmental Transmission Electron Microscopy in an Aberration-Corrected Environment." *Microscopy and Microanalysis* 18 (04):684–90. https://doi.org/10.1017/S1431927612000293.

Harada, Yoshiya, Shigeru Masuda, and Hiroyuki Ozaki. 1997. "Electron Spectroscopy Using Metastable Atoms as Probes for Solid Surfaces." *Chemical Reviews* 97 (6):1897–1952. https://doi.org/10.1021/cr940315v.

Hardman, P. J., R. Casanova, K. Prabhakaran, C. A. Muryn, P. L. Wincott, and G. Thornton. 1992. "Electronic Structure Effects of Potassium Adsorption on TiO2(100)." *Surface Science* 269 (May):677–81. https://doi.org/10.1016/0039-6028(92)91331-5.

Harris, Clifton, and Prashant V. Kamat. 2010. "Photocatalytic Events of CdSe Quantum Dots in Confined Media. Electrodic Behavior of Coupled Platinum Nanoparticles." *ACS Nano* 4 (12):7321–30. https://doi.org/10.1021/nn102564x.

He, Yunbin, Antonio Tilocca, Olga Dulub, Annabella Selloni, and Ulrike Diebold. 2009. "Local Ordering and Electronic Signatures of Submonolayer Water on Anatase TiO2(101)." *Nature Materials* 8 (7):585–89. https://doi.org/10.1038/nmat2466.

Henrich, Victor E., G. Dresselhaus, and H. J. Zeiger. 1980. "Energy-Dependent Electron-Energy-Loss Spectroscopy: Application to the Surface and Bulk Electronic Structure of MgO." *Physical Review B* 22 (10):4764–75. https://doi.org/10.1103/PhysRevB.22.4764.

Henzler, M. 1971. "The Origin of Surface States." *Surface Science* 25 (3):650–80. https://doi.org/10.1016/0039-6028(71)90153-1.

Herman, G. S., Z. Dohnálek, N. Ruzycki, and U. Diebold. 2003. "Experimental Investigation of the Interaction of Water and Methanol with Anatase−TiO2(101)." *The Journal of Physical Chemistry B* 107 (12):2788–95. https://doi.org/10.1021/jp0275544.

Hoffmann, Michael R., Scot T. Martin, Wonyong. Choi, and Detlef W. Bahnemann. 1995. "Environmental Applications of Semiconductor Photocatalysis." *Chemical Reviews* 95 (1):69–96. https://doi.org/10.1021/cr00033a004.

Hosokawa, Fumio, Hidetaka Sawada, Yukihito Kondo, Kunio Takayanagi, and Kazutomo Suenaga. 2013. "Development of Cs and Cc Correctors for Transmission Electron Microscopy." *Microscopy* 62 (1):23–41. https://doi.org/10.1093/jmicro/dfs134.

Houghton, John Theodore, and Intergovernmental Panel on Climate Change, eds. 2001. *Climate Change 2001: The Scientific Basis: Contribution of Working Group I to the Third Assessment Report of the Intergovernmental Panel on Climate Change*. Cambridge ; New York: Cambridge University Press.

Howe, Russell F., and Michael Gratzel. 1987. "EPR Study of Hydrated Anatase under UV Irradiation." *Journal of Physical Chemistry* 91 (14):3906–3909.

Howie, A., and R.H. Milne. 1985. "Excitations at Interfaces and Small Particles." *Ultramicroscopy* 18:427–34.

Hubbard, J. 1955. "The Dielectric Theory of Electronic Interactions in Solids." *Proceedings of the Physical Society. Section A* 68 (11):976. https://doi.org/10.1088/0370-1298/68/11/304.

Hyun, J. K., M. Couillard, P. Rajendran, C. M. Liddell, and D. A. Muller. 2008. "Measuring Far-Ultraviolet Whispering Gallery Modes with High Energy Electrons." *Applied Physics Letters* 93 (24):243106. https://doi.org/10.1063/1.3046731.

Hyun, J. K., M. P. Levendorf, M. Blood-Forsythe, J. Park, and D. A. Muller. 2010. "Relativistic Electron Energy Loss Spectroscopy of Solid and Core-Shell Nanowires." *Physical Review B* 81 (16). https://doi.org/10.1103/PhysRevB.81.165403.

Ibach, H., and D. L. Mills. 2013. *Electron Energy Loss Spectroscopy and Surface Vibrations*. Academic Press.

Inoue, Yasunobu. 2009. "Photocatalytic Water Splitting by RuO 2 -Loaded Metal Oxides and Nitrides with d 0 - and d 10 -Related Electronic Configurations." *Energy & Environmental Science* 2 (4):364–86. https://doi.org/10.1039/B816677N.

Jackson, John David. 1999. *Classical Electrodynamics*. Wiley. http://cds.cern.ch/record/490457/files/9780471309321_TOC.pdf.

James, Brian D., George N. Baum, Julie Perez, and Kevin N. Baum. 2009. "Technoeconomic Analysis of Photoelectrochemical (PEC) Hydrogen Production." 1218403. https://doi.org/10.2172/1218403.

Järrendahl, K., and H. Arwin. 1998. "Multiple Sample Analysis of Spectroscopic Ellipsometry Data of Semi-Transparent Films." *Thin Solid Films* 313–314 (February):114–18. https://doi.org/10.1016/S0040-6090(97)00781-5.

Jellison, G. E., L. A. Boatner, J. D. Budai, B.-S. Jeong, and D. P. Norton. 2003. "Spectroscopic Ellipsometry of Thin Film and Bulk Anatase (TiO[Sub 2])." *Journal of Applied Physics* 93 (12):9537. https://doi.org/10.1063/1.1573737.

Jia, Chun-Lin, Markus Lentzen, and Knut Urban. 2004. "High-Resolution Transmission Electron Microscopy Using Negative Spherical Aberration." *Microscopy and Microanalysis* 10 (02):174–84. https://doi.org/10.1017/S1431927604040425.

Johnson, Richard W., Adam Hultqvist, and Stacey F. Bent. 2014. "A Brief Review of Atomic Layer Deposition: From Fundamentals to Applications." *Materials Today* 17 (5):236–46. https://doi.org/10.1016/j.mattod.2014.04.026.

Kanan, Matthew W., and Daniel G. Nocera. 2008. "In Situ Formation of an Oxygen-Evolving Catalyst in Neutral Water Containing Phosphate and Co2+." *Science* 321 (5892):1072–75. https://doi.org/10.1126/science.1162018.

Kannan, Nadarajah, and Divagar Vakeesan. 2016. "Solar Energy for Future World: - A Review." *Renewable and Sustainable Energy Reviews* 62 (September):1092–1105. https://doi.org/10.1016/j.rser.2016.05.022.

Kanury, A. Murty. 1975. *Introduction to Combustion Phenomena: For Fire, Incineration, Pollution, and Energy Applications*. Combustion Science and Technology Book Series, v. 2. New York: Gordon and Breach.

Kato, Hideki, Kiyotaka Asakura, and Akihiko Kudo. 2003. "Highly Efficient Water Splitting into H2 and O2 over Lanthanum-Doped NaTaO3 Photocatalysts with High Crystallinity and Surface Nanostructure." *Journal of the American Chemical Society* 125 (10):3082–89. https://doi.org/10.1021/ja027751g.

Kato, Hideki, and Akihiko Kudo. 1998. "New Tantalate Photocatalysts for Water Decomposition into H2 and O2." *Chemical Physics Letters* 295 (5–6):487–92. https://doi.org/10.1016/S0009-2614(98)01001-X.

Katoh, Ryuzi, Akihiro Furube, Ken-ichi Yamanaka, and Takeshi Morikawa. 2010. "Charge Separation and Trapping in N-Doped TiO $_2$ Photocatalysts: A Time-Resolved Microwave Conductivity Study." *The Journal of Physical Chemistry Letters* 1 (22):3261–65. https://doi.org/10.1021/jz1011548.

King, P. D. C., T. D. Veal, A. Schleife, J. Zúñiga-Pérez, B. Martel, P. H. Jefferson, F. Fuchs, V. Muñoz-Sanjosé, F. Bechstedt, and C. F. McConville. 2009. "Valence-Band Electronic Structure of CdO, ZnO, and MgO from x-Ray Photoemission Spectroscopy and Quasi-Particle-Corrected Density-Functional Theory Calculations." *Physical Review B* 79 (20). https://doi.org/10.1103/PhysRevB.79.205205.

Kisumi, Tetsuya, Akira Tsujiko, Kei Murakoshi, and Yoshihiro Nakato. 2003. "Crystal-Face and Illumination Intensity Dependences of the Quantum Efficiency of Photoelectrochemical Etching, in Relation to Those of Water Photooxidation, at n-TiO2 (Rutile) Semiconductor Electrodes." *Journal of Electroanalytical Chemistry* 545 (March):99–107. https://doi.org/10.1016/S0022-0728(03)00114-1.

Krivanek, O. L., N. Dellby, and A. R. Lupini. 1999. "Towards Sub-Å Electron Beams." *Ultramicroscopy* 78 (1):1–11. https://doi.org/10.1016/S0304-3991(99)00013-3.

Krivanek, Ondrej L., Tracy C. Lovejoy, Niklas Dellby, Toshihiro Aoki, R. W. Carpenter, Peter Rez, Emmanuel Soignard, et al. 2014. "Vibrational Spectroscopy in the Electron Microscope." *Nature* 514 (7521):209–12. https://doi.org/10.1038/nature13870.

Krivanek, Ondrej L., Tracy C. Lovejoy, Niklas Dellby, and R.W. Carpenter. 2013. "Monochromated STEM with a 30 MeV-Wide, Atom-Sized Electron Probe." *Microscopy* 62 (1):3–21. https://doi.org/10.1093/jmicro/dfs089.

Krivanek, Ondrej L., Jonathan P. Ursin, Neil J. Bacon, George J. Corbin, Niklas Dellby, Petr Hrncirik, Matthew F. Murfitt, Christopher S. Own, and Zoltan S. Szilagyi. 2009. "High-Energy-Resolution Monochromator for Aberration-Corrected Scanning Transmission Electron Microscopy/Electron Energy-Loss Spectroscopy." *Philosophical Transactions of the Royal Society of London A: Mathematical, Physical and Engineering Sciences* 367 (1903):3683–97. https://doi.org/10.1098/rsta.2009.0087.

Kronik, Leeor, and Yoram Shapira. 2001. "Surface Photovoltage Spectroscopy of Semiconductor Structures: At the Crossroads of Physics, Chemistry and Electrical Engineering." *Surface and Interface Analysis* 31 (10):954–65. https://doi.org/10.1002/sia.1132.

K. Townsend, Troy, Nigel D. Browning, and Frank E. Osterloh. 2012. "Overall Photocatalytic Water Splitting with NiO $_x$ –SrTiO $_3$ – a Revised Mechanism." *Energy & Environmental Science* 5 (11):9543–50. https://doi.org/10.1039/C2EE22665K.

Kudo, Akihiko, and Yugo Miseki. 2009. "Heterogeneous Photocatalyst Materials for Water Splitting." *Chem. Soc. Rev.* 38 (1):253–78. https://doi.org/10.1039/B800489G.

Kudo, Akihiko, Akira Tanaka, Kazunari Domen, Ken-ichi Maruya, Ken-ichi Aika, and Takaharu Onishi. 1988. "Photocatalytic Decomposition of Water over NiO K4Nb6O17 Catalyst." *Journal of Catalysis* 111 (1):67–76. https://doi.org/10.1016/0021-9517(88)90066-8.

Kudo, Akihiko, Akira Tanaka, Kazunari Domen, and Takaharu Onishi. 1988. "The Effects of the Calcination Temperature of SrTiO3 Powder on Photocatalytic Activities." *Journal of Catalysis* 111 (2):296–301. https://doi.org/10.1016/0021-9517(88)90088-7.

Landmann, M, E Rauls, and W G Schmidt. 2012. "The Electronic Structure and Optical Response of Rutile, Anatase and Brookite TiO_2." *Journal of Physics: Condensed Matter* 24 (19):195503. https://doi.org/10.1088/0953-8984/24/19/195503.

Langel, Walter, and Michele Parrinello. 1994. "Hydrolysis at Stepped MgO Surfaces." *Physical Review Letters* 73 (3):504.

Lewis, Nathan S., and George Crabtree. 2005. "Basic Research Needs for Solar Energy Utilization: Report of the Basic Energy Sciences Workshop on Solar Energy Utilization, April 18-21, 2005." http://authors.library.caltech.edu/8599/.

Leytner, Svetlana, and Joseph T. Hupp. 2000. "Evaluation of the Energetics of Electron Trap States at the Nanocrystalline Titanium Dioxide/Aqueous Solution Interface via Time-Resolved Photoacoustic Spectroscopy." *Chemical Physics Letters* 330 (3–4):231–36. https://doi.org/10.1016/S0009-2614(00)01112-X.

Li, Xin, Jiaguo Yu, Jingxiang Low, Yueping Fang, Jing Xiao, and Xiaobo Chen. 2015. "Engineering Heterogeneous Semiconductors for Solar Water Splitting." *Journal of Materials Chemistry A* 3 (6):2485–2534. https://doi.org/10.1039/C4TA04461D.

Li, Ye-Fei, Zhi-Pan Liu, LuLu Liu, and Weiguo Gao. 2010. "Mechanism and Activity of Photocatalytic Oxygen Evolution on Titania Anatase in Aqueous Surroundings." *Journal of the American Chemical Society* 132 (37):13008–15. https://doi.org/10.1021/ja105340b.

Li, Ye-Fei, and Annabella Selloni. 2016. "Pathway of Photocatalytic Oxygen Evolution on Aqueous TiO2 Anatase and Insights into the Different Activities of Anatase and Rutile." *ACS Catalysis* 6 (7):4769–74. https://doi.org/10.1021/acscatal.6b01138.

Linsebigler, Amy L., Guangquan. Lu, and John T. Yates. 1995. "Photocatalysis on TiO2 Surfaces: Principles, Mechanisms, and Selected Results." *Chemical Reviews* 95 (3):735–58. https://doi.org/10.1021/cr00035a013.

Liu, J., Y. Liu, N. Liu, Y. Han, X. Zhang, H. Huang, Y. Lifshitz, S.-T. Lee, J. Zhong, and Z. Kang. 2015. "Metal-Free Efficient Photocatalyst for Stable Visible Water Splitting via a Two-Electron Pathway." *Science* 347 (6225):970–74. https://doi.org/10.1126/science.aaa3145.

Liu, Qianlang, Katia March, and Peter A. Crozier. 2017. "Nanoscale Probing of Bandgap States on Oxide Particles Using Electron Energy-Loss Spectroscopy." *Ultramicroscopy*, FEMMS 2015FEMMS 2015, 178 (July): 2–11. https://doi.org/10.1016/j.ultramic.2016.06.010.

Loane, R. F., E. J. Kirkland, and J. Silcox. 1988. "Visibility of Single Heavy Atoms on Thin Crystalline Silicon in Simulated Annular Dark-Field STEM Images." *Acta Crystallographica Section A: Foundations of Crystallography* 44 (6):912–927.

Maeda, Kazuhiko. 2011. "Photocatalytic Water Splitting Using Semiconductor Particles: History and Recent Developments." *Journal of Photochemistry and Photobiology C: Photochemistry Reviews* 12 (4):237–68. https://doi.org/10.1016/j.jphotochemrev.2011.07.001.

Maeda, Kazuhiko, and Kazunari Domen. 2010. "Photocatalytic Water Splitting: Recent Progress and Future Challenges." *The Journal of Physical Chemistry Letters* 1 (18):2655–61. https://doi.org/10.1021/jz1007966.

Maeda, Kazuhiko, Tsuyoshi Takata, Michikazu Hara, Nobuo Saito, Yasunobu Inoue, Hisayoshi Kobayashi, and Kazunari Domen. 2005. "GaN:ZnO Solid Solution as a Photocatalyst for Visible-Light-Driven Overall Water Splitting." *Journal of the American Chemical Society* 127 (23):8286–87. https://doi.org/10.1021/ja0518777.

Maeda, Kazuhiko, Kentaro Teramura, Daling Lu, Nobuo Saito, Yasunobu Inoue, and Kazunari Domen. 2006. "Noble-Metal/Cr2O3 Core/Shell Nanoparticles as a Cocatalyst for Photocatalytic Overall Water Splitting." *Angewandte Chemie International Edition* 45 (46):7806–9. https://doi.org/10.1002/anie.200602473.

Maeda, Kazuhiko, Kentaro Teramura, Daling Lu, Tsuyoshi Takata, Nobuo Saito, Yasunobu Inoue, and Kazunari Domen. 2006. "Photocatalyst Releasing Hydrogen from Water." *Nature* 440 (7082):295–295. https://doi.org/10.1038/440295a.

Maeda, Kazuhiko, Xinchen Wang, Yasushi Nishihara, Daling Lu, Markus Antonietti, and Kazunari Domen. 2009. "Photocatalytic Activities of Graphitic Carbon Nitride Powder for Water Reduction and Oxidation under Visible Light." *The Journal of Physical Chemistry C* 113 (12):4940–47. https://doi.org/10.1021/jp809119m.

Malashevich, Andrei, Eric I. Altman, and Sohrab Ismail-Beigi. 2014. "Imaging the Buried MgO/Ag Interface: Formation Mechanism of the STM Contrast." *Physical Review B* 90 (16). https://doi.org/10.1103/PhysRevB.90.165426.

Marcus, Rudolph A. 1964. "Chemical and Electrochemical Electron-Transfer Theory." *Annual Review of Physical Chemistry* 15 (1):155–196.

Matsumoto, Yasumichi, Ugur Unal, Noriyuki Tanaka, Akihiko Kudo, and Hideki Kato. 2004. "Electrochemical Approach to Evaluate the Mechanism of Photocatalytic Water

Splitting on Oxide Photocatalysts." *Journal of Solid State Chemistry* 177 (11):4205–12. https://doi.org/10.1016/j.jssc.2004.08.001.

McCrory, Charles C. L., Suho Jung, Ivonne M. Ferrer, Shawn M. Chatman, Jonas C. Peters, and Thomas F. Jaramillo. 2015. "Benchmarking Hydrogen Evolving Reaction and Oxygen Evolving Reaction Electrocatalysts for Solar Water Splitting Devices." *Journal of the American Chemical Society* 137 (13):4347–57. https://doi.org/10.1021/ja510442p.

Meekins, Benjamin H., and Prashant V. Kamat. 2011. "Role of Water Oxidation Catalyst IrO2 in Shuttling Photogenerated Holes Across TiO2 Interface." *The Journal of Physical Chemistry Letters* 2 (18):2304–10. https://doi.org/10.1021/jz200852m.

M. Fabian, David, Shu Hu, Nirala Singh, Frances A. Houle, Takashi Hisatomi, Kazunari Domen, Frank E. Osterloh, and Shane Ardo. 2015. "Particle Suspension Reactors and Materials for Solar-Driven Water Splitting." *Energy & Environmental Science* 8 (10):2825–50. https://doi.org/10.1039/C5EE01434D.

Miller, Benjamin, Peter A Crozier, Martha Mccartney, Peter Rez, and Arizona State University. 2012. "A System for In Situ UV-Visible Illumination of Transmission Electron Microscope Samples." In *ASU Electronic Theses and Dissertations*. Arizona State University. http://hdl.handle.net/2286/R.I.15192.

Miller, Benjamin K., and Peter A. Crozier. 2013. "System for In Situ UV-Visible Illumination of Environmental Transmission Electron Microscopy Samples." *Microscopy and Microanalysis* 19 (02):461–469. https://doi.org/10.1017/S1431927612014122.

Mönch, Winfried. 2013. *Semiconductor Surfaces and Interfaces*. Springer Science & Business Media.

Moreau, P., N. Brun, C. A. Walsh, C. Colliex, and A. Howie. 1997. "Relativistic Effects in Electron-Energy-Loss-Spectroscopy Observations of the S i/S i O 2 Interface Plasmon Peak." *Physical Review B* 56 (11):6774.

Moser, S., L. Moreschini, J. Jaćimović, O. S. Barišić, H. Berger, A. Magrez, Y. J. Chang, et al. 2013. "Tunable Polaronic Conduction in Anatase TiO 2." *Physical Review Letters* 110 (19). https://doi.org/10.1103/PhysRevLett.110.196403.

Muller, D. A., L. Fitting Kourkoutis, M. Murfitt, J. H. Song, H. Y. Hwang, J. Silcox, N. Dellby, and O. L. Krivanek. 2008. "Atomic-Scale Chemical Imaging of Composition and Bonding by Aberration-Corrected Microscopy." *Science* 319 (5866):1073–76. https://doi.org/10.1126/science.1148820.

Nakamura, Ryuhei, and Yoshihiro Nakato. 2004. "Primary Intermediates of Oxygen Photoevolution Reaction on TiO2 (Rutile) Particles, Revealed by in Situ FTIR Absorption and Photoluminescence Measurements." *Journal of the American Chemical Society* 126 (4):1290–98. https://doi.org/10.1021/ja0388764.

Nakamura, Ryuhei, Tomoaki Okamura, Naomichi Ohashi, Akihito Imanishi, and Yoshihiro Nakato. 2005. "Molecular Mechanisms of Photoinduced Oxygen Evolution, PL Emission, and Surface Roughening at Atomically Smooth (110) and (100) *n* -TiO $_2$ (Rutile) Surfaces in Aqueous Acidic Solutions." *Journal of the American Chemical Society* 127 (37):12975–83. https://doi.org/10.1021/ja053252e.

Nellist, P. D., M. F. Chisholm, N. Dellby, O. L. Krivanek, M. F. Murfitt, Z. S. Szilagyi, A. R. Lupini, A. Borisevich, W. H. Sides, and S. J. Pennycook. 2004. "Direct Sub-Angstrom Imaging of a Crystal Lattice." *Science* 305 (5691):1741–1741. https://doi.org/10.1126/science.1100965.

Nelson, Jenny. 2003. *The Physics of Solar Cells*. World Scientific Publishing Co Inc.

Nobis, Thomas, Evgeni M. Kaidashev, Andreas Rahm, Michael Lorenz, and Marius Grundmann. 2004. "Whispering Gallery Modes in Nanosized Dielectric Resonators with Hexagonal Cross Section." *Physical Review Letters* 93 (10). https://doi.org/10.1103/PhysRevLett.93.103903.

Nozik, A. J. 1977. "Photochemical Diodes." *Applied Physics Letters* 30 (11):567–69. https://doi.org/10.1063/1.89262.

Ogura, Shuji, Mitsuru Kohno, Kazunori Sato, and Yasunobu Inoue. 1997. "Photocatalytic Activity for Water Decomposition of RuO2-Combined M2Ti6O13 (M = Na, K, Rb, Cs)." *Applied Surface Science*, Iketani-6, 121 (November):521–24. https://doi.org/10.1016/S0169-4332(97)00358-9.

Ohno, Teruhisa, Koji Sarukawa, and Michio Matsumura. 2002. "Crystal Faces of Rutile and Anatase TiO2 Particles and Their Roles in Photocatalytic Reactions." *New Journal of Chemistry* 26 (9):1167–70. https://doi.org/10.1039/b202140d.

Ohtani, Bunsho. 2008. "Preparing Articles on Photocatalysis—beyond the Illusions, Misconceptions, and Speculation." *Chemistry Letters* 37 (3):216–229.

O'Keefe, Michael A. 2008. "Seeing Atoms with Aberration-Corrected Sub-Ångström Electron Microscopy." *Ultramicroscopy* 108 (3):196–209. https://doi.org/10.1016/j.ultramic.2007.07.009.

Okunishi, E., I. Ishikawa, H. Sawada, F. Hosokawa, M. Hori, and Y. Kondo. 2009. "Visualization of Light Elements at Ultrahigh Resolution by STEM Annular Bright Field Microscopy." *Microscopy and Microanalysis* 15 (S2):164–65. https://doi.org/10.1017/S1431927609093891.

Oreskes, N. 2004. "BEYOND THE IVORY TOWER: The Scientific Consensus on Climate Change." *Science* 306 (5702):1686–1686. https://doi.org/10.1126/science.1103618.

Osterloh, Frank E. 2014a. "Boosting the Efficiency of Suspended Photocatalysts for Overall Water Splitting." *The Journal of Physical Chemistry Letters* 5 (15):2510–11. https://doi.org/10.1021/jz501342j.

———. 2014b. "Maximum Theoretical Efficiency Limit of Photovoltaic Devices: Effect of Band Structure on Excited State Entropy." *The Journal of Physical Chemistry Letters* 5 (19):3354–59. https://doi.org/10.1021/jz501740n.

———. 2015. "Nanoscale Effects in Water Splitting Photocatalysis," 105–42. https://doi.org/10.1007/128_2015_633.

Osterloh, Frank E., and Bruce A. Parkinson. 2011. "Recent Developments in Solar Water-Splitting Photocatalysis." *MRS Bulletin* 36 (01):17–22. https://doi.org/10.1557/mrs.2010.5.

Pachauri, R. K., Leo Mayer, and Intergovernmental Panel on Climate Change, eds. 2015. *Climate Change 2014: Synthesis Report*. Geneva, Switzerland: Intergovernmental Panel on Climate Change.

Pachauri, Rajendra K., and IPCC, eds. 2008. *Climate Change 2007:: Contribution of ... to the Fourth Assessment Report of the Intergovernmental Panel on Climate Change. 4: Synthesis Report: [A Report of the Intergovernmental Panel on Climate Change]*. Geneva: IPCC.

Parsons, Roger. 1958. "The Rate of Electrolytic Hydrogen Evolution and the Heat of Adsorption of Hydrogen." *Transactions of the Faraday Society* 54 (0):1053–63. https://doi.org/10.1039/TF9585401053.

Pennycook, Stephen J., and Peter D. Nellist, eds. 2011. *Scanning Transmission Electron Microscopy: Imaging and Analysis*. New York, NY: Springer.

Peraldi, R., D. Monceau, and B. Pieraggi. 2002. "Correlations Between Growth Kinetics and Microstructure for Scales Formed by High-Temperature Oxidation of Pure Nickel. II. Growth Kinetics." *Oxidation of Metals* 58 (3–4):275–95. https://doi.org/10.1023/A:1020102604090.

Pogorzelski, R., and C. Yeh. 1973. "Diffraction Radiation from a Charged Particle Moving through a Penetrable Sphere." *Physical Review A* 8 (1):137.

Poole, Colin. 2012. *Gas Chromatography*. Elsevier Science & Technology. http://www.myilibrary.com?id=368078.

Potylitsyn, A. P. 1998. "Transition Radiation and Diffraction Radiation. Similarities and Differences." *Nuclear Instruments and Methods in Physics Research Section B: Beam Interactions with Materials and Atoms* 145 (1):169–79. https://doi.org/10.1016/S0168-583X(98)00384-X.

Purcell, Edward M., and Carlton R. Pennypacker. 1973. "Scattering and Absorption of Light by Nonspherical Dielectric Grains." *The Astrophysical Journal* 186 (December):705–14. https://doi.org/10.1086/152538.

Raether, H. 1965. "Solid State Excitations by Electrons." In *Springer Tracts in Modern Physics, Volume 38*, 38:84–157. Berlin/Heidelberg: Springer-Verlag. http://www.springerlink.com/index/10.1007/BFb0045738.

Ramasse, Quentin M., Che R. Seabourne, Despoina-Maria Kepaptsoglou, Recep Zan, Ursel Bangert, and Andrew J. Scott. 2013. "Probing the Bonding and Electronic Structure of Single Atom Dopants in Graphene with Electron Energy Loss Spectroscopy." *Nano Letters* 13 (10):4989–95. https://doi.org/10.1021/nl304187e.

Ran, Jingrun, Jun Zhang, Jiaguo Yu, Mietek Jaroniec, and Shi Zhang Qiao. 2014. "Earth-Abundant Cocatalysts for Semiconductor-Based Photocatalytic Water Splitting." *Chemical Society Reviews* 43 (22):7787–7812. https://doi.org/10.1039/C3CS60425J.

Reimer, Ludwig. 2013. *Transmission Electron Microscopy: Physics of Image Formation and Microanalysis*. Springer.

Ritchie, R. H. 1957. "Plasma Losses by Fast Electrons in Thin Films." *Physical Review* 106 (5):874–81. https://doi.org/10.1103/PhysRev.106.874.

Robertson, Ian M., and D. Teter. 1998. "Controlled Environment Transmission Electron Microscopy." *Microscopy Research and Technique* 42 (4):260–69. https://doi.org/10.1002/(SICI)1097-0029(19980915)42:4<260::AID-JEMT5>3.0.CO;2-U.

Roessler, D. M., and W. C. Walker. 1967. "Electronic Spectrum and Ultraviolet Optical Properties of Crystalline MgO." *Physical Review* 159 (3):733–38. https://doi.org/10.1103/PhysRev.159.733.

Sabio, Erwin M., Rachel L. Chamousis, Nigel D. Browning, and Frank E. Osterloh. 2012. "Photocatalytic Water Splitting with Suspended Calcium Niobium Oxides: Why Nanoscale Is Better than Bulk – A Kinetic Analysis." *The Journal of Physical Chemistry C* 116 (4):3161–70. https://doi.org/10.1021/jp209006n.

Sakata, T., T. Kawai, and K. Hashimoto. 1982. "Photochemical Diode Model of Pt/TiO2 Particle and Its Photocatalytic Activity." *Chemical Physics Letters* 88 (1):50–54. https://doi.org/10.1016/0009-2614(82)80068-7.

Salvador, Pedro. 2011. "Mechanisms of Water Photooxidation at N-TiO2 Rutile Single Crystal Oriented Electrodes under UV Illumination in Competition with Photocorrosion." *Progress in Surface Science* 86 (1):41–58. https://doi.org/10.1016/j.progsurf.2010.10.002.

Sato, J., H. Kobayashi, and Y. Inoue. 2003. "Photocatalytic Activity for Water Decomposition of Indates with Octahedrally Coordinated D10 Configuration. II. Roles of Geometric and Electronic Structures." *The Journal of Physical Chemistry B* 107 (31):7970–75. https://doi.org/10.1021/jp030021q.

Sato, S., and J. M. White. 1980. "Photodecomposition of Water over Pt/TiO2 Catalysts." *Chemical Physics Letters* 72 (1):83–86. https://doi.org/10.1016/0009-2614(80)80246-6.

Scherzer, O. 1949. "The Theoretical Resolution Limit of the Electron Microscope." *Journal of Applied Physics* 20 (1):20–29. https://doi.org/10.1063/1.1698233.

Selcuk, Sencer, and Annabella Selloni. 2016. "Facet-Dependent Trapping and Dynamics of Excess Electrons at Anatase TiO2 Surfaces and Aqueous Interfaces." *Nature Materials* 15 (10):1107–12. https://doi.org/10.1038/nmat4672.

Serpone, N., D. Lawless, R. Khairutdinov, and Ezio Pelizzetti. 1995. "Subnanosecond Relaxation Dynamics in TiO2 Colloidal Sols (Particle Sizes Rp= 1.0-13.4 Nm). Relevance to Heterogeneous Photocatalysis." *The Journal of Physical Chemistry* 99 (45):16655–16661.

Setvin, Martin, Xianfeng Hao, Benjamin Daniel, Jiri Pavelec, Zbynek Novotny, Gareth S. Parkinson, Michael Schmid, Georg Kresse, Cesare Franchini, and Ulrike Diebold. 2014. "Charge Trapping at the Step Edges of TiO2 Anatase (101)." *Angewandte Chemie International Edition* 53 (18):4714–16. https://doi.org/10.1002/anie.201309796.

Smith, David J. 2008. "Development of Aberration-Corrected Electron Microscopy." *Microscopy and Microanalysis* 14 (1):2–15. https://doi.org/10.1017/S1431927608080124.

Sobolev, V. Val. 2004. "Exciton Spectra of MgO." *Inorganic Materials* 40 (11):1169–1172.

Spiecker, E., M. Garbrecht, W. JäGer, and K. Tillmann. 2010. "Advantages of Aberration Correction for HRTEM Investigation of Complex Layer Compounds." *Journal of Microscopy* 237 (3):341–46. https://doi.org/10.1111/j.1365-2818.2009.03257.x.

Stocker, T. F., D. Qin, G. K. Plattner, M. Tignor, S. K. Allen, J. Boschung, A. Nauels, Y. Xia, B. Bex, and B. M. Midgley. 2013. "IPCC, 2013: Climate Change 2013: The Physical Science Basis. Contribution of Working Group I to the Fifth Assessment Report of the Intergovernmental Panel on Climate Change."

Stöger-Pollach, M. 2008. "Optical Properties and Bandgaps from Low Loss EELS: Pitfalls and Solutions." *Micron* 39 (8):1092–1110. https://doi.org/10.1016/j.micron.2008.01.023.

Stroscio, Joseph A., R. M. Feenstra, and A. P. Fein. 1986. "Electronic Structure of the Si (111) 2×1 Surface by Scanning-Tunneling Microscopy." *Physical Review Letters* 57 (20):2579.

Subramanian, Vaidyanathan, Eduardo E. Wolf, and Prashant V. Kamat. 2004. "Catalysis with TiO2/Gold Nanocomposites. Effect of Metal Particle Size on the Fermi Level

Equilibration." *Journal of the American Chemical Society* 126 (15):4943–50. https://doi.org/10.1021/ja0315199.

Sumita, Masato, Chunping Hu, and Yoshitaka Tateyama. 2010. "Interface Water on TiO2 Anatase (101) and (001) Surfaces: First-Principles Study with TiO2 Slabs Dipped in Bulk Water." *The Journal of Physical Chemistry C* 114 (43):18529–37. https://doi.org/10.1021/jp105364z.

Sun, Chenghua, Li-Min Liu, Annabella Selloni, Gao Qing (Max) Lu, and Sean C. Smith. 2010. "Titania-Water Interactions: A Review of Theoretical Studies." *Journal of Materials Chemistry* 20 (46):10319–34. https://doi.org/10.1039/C0JM01491E.

Sun, Jingxue, Gang Chen, Yingxuan Li, Rencheng Jin, Qun Wang, and Jian Pei. 2011. "Novel (Na, K)TaO 3 Single Crystal Nanocubes: Molten Salt Synthesis, Invariable Energy Level Doping and Excellent Photocatalytic Performance." *Energy & Environmental Science* 4 (10):4052–60. https://doi.org/10.1039/C1EE01259B.

Surendranath, Yogesh, Mircea Dincă, and Daniel G. Nocera. 2009. "Electrolyte-Dependent Electrosynthesis and Activity of Cobalt-Based Water Oxidation Catalysts." *Journal of the American Chemical Society* 131 (7):2615–20. https://doi.org/10.1021/ja807769r.

Tachikawa, Takashi, Soichiro Yamashita, and Tetsuro Majima. 2011. "Evidence for Crystal-Face-Dependent TiO2 Photocatalysis from Single-Molecule Imaging and Kinetic Analysis." *Journal of the American Chemical Society* 133 (18):7197–7204. https://doi.org/10.1021/ja201415j.

Taheri, Mitra L., Eric A. Stach, Ilke Arslan, P. A. Crozier, Bernd C. Kabius, Thomas LaGrange, Andrew M. Minor, et al. 2016. "Current Status and Future Directions for in Situ Transmission Electron Microscopy." *Ultramicroscopy* 170 (November):86–95. https://doi.org/10.1016/j.ultramic.2016.08.007.

Takai, Azusa, and Prashant V. Kamat. 2011. "Capture, Store, and Discharge. Shuttling Photogenerated Electrons across TiO2–Silver Interface." *ACS Nano* 5 (9):7369–76. https://doi.org/10.1021/nn202294b.

Takata, Tsuyoshi, Yoko Furumi, Kiyoaki Shinohara, Akira Tanaka, Michikazu Hara, Junko N. Kondo, and Kazunari Domen. 1997. "Photocatalytic Decomposition of Water on Spontaneously Hydrated Layered Perovskites." *Chemistry of Materials* 9 (5):1063–64. https://doi.org/10.1021/cm960612b.

Tamm, Ig. 1932. "About a possible type of electron binding on crystal surfaces." *Zeitschrift Fur Physik* 76 (11–12):849–50. https://doi.org/10.1007/BF01341581.

Tang, Junwang, James R. Durrant, and David R. Klug. 2008. "Mechanism of Photocatalytic Water Splitting in TiO2. Reaction of Water with Photoholes, Importance of Charge

Carrier Dynamics, and Evidence for Four-Hole Chemistry." *Journal of the American Chemical Society* 130 (42):13885–91. https://doi.org/10.1021/ja8034637.

Thomas, A. G., W. R. Flavell, A. K. Mallick, A. R. Kumarasinghe, D. Tsoutsou, N. Khan, C. Chatwin, et al. 2007. "Comparison of the Electronic Structure of Anatase and Rutile TiO 2 Single-Crystal Surfaces Using Resonant Photoemission and x-Ray Absorption Spectroscopy." *Physical Review B* 75 (3). https://doi.org/10.1103/PhysRevB.75.035105.

Thompson, Tracy L., and John T. Yates. 2006. "Surface Science Studies of the Photoactivation of TiO2New Photochemical Processes." *Chemical Reviews* 106 (10):4428–53. https://doi.org/10.1021/cr050172k.

Tilocca, Antonio, and Annabella Selloni. 2003. "Reaction Pathway and Free Energy Barrier for Defect-Induced Water Dissociation on the (101) Surface of TiO2-Anatase." *The Journal of Chemical Physics* 119 (14):7445–50. https://doi.org/10.1063/1.1607306.

———. 2004. "Structure and Reactivity of Water Layers on Defect-Free and Defective Anatase TiO2(101) Surfaces." *The Journal of Physical Chemistry B* 108 (15):4743–51. https://doi.org/10.1021/jp037685k.

Tong, Hua, Shuxin Ouyang, Yingpu Bi, Naoto Umezawa, Mitsutake Oshikiri, and Jinhua Ye. 2012. "Nano-Photocatalytic Materials: Possibilities and Challenges." *Advanced Materials* 24 (2):229–51. https://doi.org/10.1002/adma.201102752.

Trasatti, Sergio. 1972. "Work Function, Electronegativity, and Electrochemical Behaviour of Metals." *Journal of Electroanalytical Chemistry and Interfacial Electrochemistry* 39 (1):163–84. https://doi.org/10.1016/S0022-0728(72)80485-6.

———. 1980. "Electrocatalysis by Oxides — Attempt at a Unifying Approach." *Journal of Electroanalytical Chemistry and Interfacial Electrochemistry* 111 (1):125–31. https://doi.org/10.1016/S0022-0728(80)80084-2.

Turner, John A. 1999. "A Realizable Renewable Energy Future." *Science* 285 (5428):687–89. https://doi.org/10.1126/science.285.5428.687.

Urban, Knut W. 2008. "Studying Atomic Structures by Aberration-Corrected Transmission Electron Microscopy." *Science* 321 (5888):506–10. https://doi.org/10.1126/science.1152800.

Valdés, Álvaro, Jeremie Brillet, Michael Grätzel, Hildur Gudmundsdóttir, Heine A. Hansen, Hannes Jónsson, Peter Klüpfel, et al. 2012. "Solar Hydrogen Production with Semiconductor Metal Oxides : New Directions in Experiment and Theory." *Physical Chemistry Chemical Physics* 14 (1):49–70. https://doi.org/10.1039/C1CP23212F.

Van Dyck, D., and A. F. de Jong. 1992. "Ultimate Resolution and Information in Electron Microscopy: General Principles." *Ultramicroscopy* 47 (1):266–81. https://doi.org/10.1016/0304-3991(92)90202-U.

Vittadini, A., A. Selloni, F. P. Rotzinger, and M. Grätzel. 1998. "Structure and Energetics of Water Adsorbed at TiO2 Anatase (101) and (001) Surfaces." *Physical Review Letters* 81 (14):2954.

Vittadini, Andrea, Maurizio Casarin, and Annabella Selloni. 2007. "Chemistry of and on TiO2-Anatase Surfaces by DFT Calculations: A Partial Review." *Theoretical Chemistry Accounts* 117 (5–6):663–71. https://doi.org/10.1007/s00214-006-0191-4.

Wagner, Jakob B., Filippo Cavalca, Christian D. Damsgaard, Linus D. L. Duchstein, and Thomas W. Hansen. 2012. "Exploring the Environmental Transmission Electron Microscope." *Micron*, In situ TEM, 43 (11):1169–75. https://doi.org/10.1016/j.micron.2012.02.008.

Walter, Michael G., Emily L. Warren, James R. McKone, Shannon W. Boettcher, Qixi Mi, Elizabeth A. Santori, and Nathan S. Lewis. 2010. "Solar Water Splitting Cells." *Chemical Reviews* 110 (11):6446–73. https://doi.org/10.1021/cr1002326.

Wang, Li-Qiong, D. R. Baer, and M. H. Engelhard. 1994. "Creation of Variable Concentrations of Defects on TiO2(110) Using Low-Density Electron Beams." *Surface Science* 320 (3):295–306. https://doi.org/10.1016/0039-6028(94)90317-4.

Wang, Xinchen, Kazuhiko Maeda, Arne Thomas, Kazuhiro Takanabe, Gang Xin, Johan M. Carlsson, Kazunari Domen, and Markus Antonietti. 2009. "A Metal-Free Polymeric Photocatalyst for Hydrogen Production from Water under Visible Light." *Nature Materials* 8 (1):76–80. https://doi.org/10.1038/nmat2317.

Wang, Yang, Huijuan Sun, Shijing Tan, Hao Feng, Zhengwang Cheng, Jin Zhao, Aidi Zhao, et al. 2013. "Role of Point Defects on the Reactivity of Reconstructed Anatase Titanium Dioxide (001) Surface." *Nature Communications* 4 (July). https://doi.org/10.1038/ncomms3214.

Wang, Z. L. 1996. "Valence Electron Excitations and Plasmon Oscillations in Thin Films, Surfaces, Interfaces and Small Particles." *Micron* 27 (3–4):265–99. https://doi.org/10.1016/0968-4328(96)00011-X.

Wang, Z. L., and J. M. Cowley. 1988. "Reflection Electron Energy Loss Spectroscopy (REELS): A Technique for the Study of Surfaces." *Surface Science* 193 (3):501–12. https://doi.org/10.1016/0039-6028(88)90449-9.

Weber, Michael F., and Michael J. Dignam. 1984. "Efficiency of Splitting Water with Semiconducting Photoelectrodes." *Journal of The Electrochemical Society* 131 (6):1258–65. https://doi.org/10.1149/1.2115797.

Wiegel, M., M. H. J. Emond, E. R. Stobbe, and G. Blasse. 1994. "Luminescence of Alkali Tantalates and Niobates." *Journal of Physics and Chemistry of Solids* 55 (8):773–78. https://doi.org/10.1016/0022-3697(94)90030-2.

Williams, David B., and C. Barry Carter. 2008. *Transmission Electron Microscopy: A Textbook for Materials Science*. 2nd ed. New York: Springer.

Xu, Yong, and Martin A. A. Schoonen. 2000. "The Absolute Energy Positions of Conduction and Valence Bands of Selected Semiconducting Minerals." *American Mineralogist* 85 (3–4):543–56. https://doi.org/10.2138/am-2000-0416.

Xu, Yong-Nian, and W. Y. Ching. 1991. "Self-Consistent Band Structures, Charge Distributions, and Optical-Absorption Spectra in MgO, α-Al2O3, and MgAl2O4." *Physical Review B* 43 (5):4461–72. https://doi.org/10.1103/PhysRevB.43.4461.

Yamamoto, N., K. Araya, and F. J. García de Abajo. 2001. "Photon Emission from Silver Particles Induced by a High-Energy Electron Beam." *Physical Review B* 64 (20). https://doi.org/10.1103/PhysRevB.64.205419.

Yang, Zhijie, Yanzhao Yang, Hui Liang, and Ling Liu. 2009. "Hydrothermal Synthesis of Monodisperse CeO2 Nanocubes." *Materials Letters* 63 (21):1774–77. https://doi.org/10.1016/j.matlet.2009.05.034.

Yang, Zhiqiang, Kebin Zhou, Xiangwen Liu, Qun Tian, Deyi Lu, and Sen Yang. 2007. "Single-Crystalline Ceria Nanocubes: Size-Controlled Synthesis, Characterization and Redox Property." *Nanotechnology* 18 (18):185606. https://doi.org/10.1088/0957-4484/18/18/185606.

Yeh, Te-Fu, Chiao-Yi Teng, Shean-Jen Chen, and Hsisheng Teng. 2014. "Nitrogen-Doped Graphene Oxide Quantum Dots as Photocatalysts for Overall Water-Splitting under Visible Light Illumination." *Advanced Materials* 26 (20):3297–3303. https://doi.org/10.1002/adma.201305299.

Yoshida, Kenta, Jun Yamasaki, and Nobuo Tanaka. 2004. "In Situ High-Resolution Transmission Electron Microscopy Observation of Photodecomposition Process of Poly-Hydrocarbons on Catalytic TiO[Sub 2] Films." *Applied Physics Letters* 84 (14):2542. https://doi.org/10.1063/1.1689747.

Yoshida, Masaaki, Kazuhiro Takanabe, Kazuhiko Maeda, Akio Ishikawa, Jun Kubota, Yoshihisa Sakata, Yasunari Ikezawa, and Kazunari Domen. 2009. "Role and Function of Noble-Metal/Cr-Layer Core/Shell Structure Cocatalysts for Photocatalytic Overall Water Splitting Studied by Model Electrodes." *The Journal of Physical Chemistry C* 113 (23):10151–57. https://doi.org/10.1021/jp901418u.

Yurtsever, Aycan, Martin Couillard, and David A. Muller. 2008. "Formation of Guided Cherenkov Radiation in Silicon-Based Nanocomposites." *Physical Review Letters* 100 (21). https://doi.org/10.1103/PhysRevLett.100.217402.

Zhang, Chao, Wei Tian, Zhi Xu, Xi Wang, Jiangwei Liu, Song-Lin Li, Dai-Ming Tang, et al. 2014. "Photosensing Performance of Branched CdS/ZnO Heterostructures as

Revealed by in Situ TEM and Photodetector Tests." *Nanoscale* 6 (14):8084–90. https://doi.org/10.1039/C4NR00963K.

Zhang, Liuxian. 2015. "Atomic Level Study of Structural Changes of TiO2 Based Photocatalysts During Solar Water Splitting Reactions Using TEM." Ph.D., United States -- Arizona: Arizona State University. http://search.proquest.com.ezproxy1.lib.asu.edu/docview/1749738831/abstract/8DF28B350EA64207PQ/1.

Zhang, Liuxian, Qianlang Liu, Toshihiro Aoki, and Peter A. Crozier. 2015. "Structural Evolution during Photocorrosion of Ni/NiO Core/Shell Cocatalyst on TiO2." *The Journal of Physical Chemistry C* 119 (13):7207–14. https://doi.org/10.1021/jp512907g.

Zhang, Liuxian, Benjamin K. Miller, and Peter A. Crozier. 2013. "Atomic Level In Situ Observation of Surface Amorphization in Anatase Nanocrystals During Light Irradiation in Water Vapor." *Nano Letters* 13 (2):679–84. https://doi.org/10.1021/nl304333h.

Zhang, Peng, Jijie Zhang, and Jinlong Gong. 2014. "Tantalum-Based Semiconductors for Solar Water Splitting." *Chemical Society Reviews* 43 (13):4395. https://doi.org/10.1039/c3cs60438a.

Zhang, Zhen, and John T. Yates. 2012. "Band Bending in Semiconductors: Chemical and Physical Consequences at Surfaces and Interfaces." *Chemical Reviews* 112 (10):5520–51. https://doi.org/10.1021/cr3000626.

Zhu, H. Y., Y. Lan, X. P. Gao, S. P. Ringer, Z. F. Zheng, D. Y. Song, and J. C. Zhao. 2005. "Phase Transition between Nanostructures of Titanate and Titanium Dioxides via Simple Wet-Chemical Reactions." *Journal of the American Chemical Society* 127 (18):6730–36. https://doi.org/10.1021/ja044689+.

Zhu, Jiangtao, Peter A. Crozier, Peter Ercius, and James R. Anderson. 2014. "Derivation of Optical Properties of Carbonaceous Aerosols by Monochromated Electron Energy-Loss Spectroscopy." *Microscopy and Microanalysis* 20 (03):748–59. https://doi.org/10.1017/S143192761400049X.

Zolotorev, Max S., and Kirk T. McDonald. 2000. "Classical Radiation Processes in the Weizsacker-Williams Approximation." *ArXiv Preprint Physics/0003096*. https://arxiv.org/abs/physics/0003096.

Zubko, Evgenij, Dmitry Petrov, Yevgen Grynko, Yuriy Shkuratov, Hajime Okamoto, Karri Muinonen, Timo Nousiainen, Hiroshi Kimura, Tetsuo Yamamoto, and Gorden Videen. 2010. "Validity Criteria of the Discrete Dipole Approximation." *Applied Optics* 49 (8):1267–79. https://doi.org/10.1364/AO.49.001267.